Electronic transport through correlated nanostructures:

molecular diodes and steady state currents.

Elektronischer Transport durch korrelierte Nanostrukturen:

molekulare Dioden und Ströme in stationären Zuständen.

_____

Zur Erlangung des akademischen Grades eines
DOKTORS DER NATURWISSENSCHAFTEN
an der Fakultät für Physik des
Karlsruher Instituts für Technologie

genehmigte
Dissertation
von
Dipl.-Phys. Tim David Collet
aus Ottweiler

Erstgutachter: Professor Dr. Jörg Schmalian
Zweitgutachter: Professor Dr. Ferdinand Evers

Tag der mündlichen Prüfung: 7. November 2014

Contents

Chapter 1

Introduction

Nothing tends so much to the advancement of knowledge as the application of a new instrument. The native intellectual powers of men in different times are not so much the causes of the different success of their labours, as the peculiar nature of the means and artificial resources in their possession.

Sir Humphry Davy (1778-1829)[1]

This work is on the topic of electronic transport in nanodevices using numerical techniques, targeting advancements in electronic circuitry. Within this research area, the thesis pursues two routes. On the one hand the author uses already existing computational 'instruments' at the frontier of research on electronic devices, where the theoretical understanding of an electric current asymmetry in certain types of molecules is improved [2]. This improvement is achieved via simulation of isolated effects which can not be separated experimentally. On the other hand limitations of these 'instruments' are attacked, resulting in new tools with a broadened scope of application [3]. Thus the 'artificial resources' available are improved, enabling new insights to be gained and new discoveries to be made, in the spirit of Sir Humphry Davy.

The story of electronic circuitry started when Frederick Guthrie discovered the first one-directional current flow in 1873. He observed the discharging of a positively charged electroscope when a glowing, electrically grounded metal was brought nearby, while negatively charged electroscopes did not discharge. This effect is nowadays called Edison effect and led to the development of vacuum tube diodes. In the following year, Karl Ferdinand Braun discovered the 'dependence of electric conductance upon the direction of the current' – which will be called in short 'rectification' within the scope of this thesis – in a semiconductor coupled to a metallic wire [4]. This discovery paved the way for semiconductor based diodes.

After the Edison-Richardson-effect was rediscovered by Thomas Edison in 1880, electronic circuits became prominent, e.g. for use in the 'first automatic electronic computer' in 1942 [5]. Since then, there has been huge progress in electronic circuitry due to advances in the construction of semiconducting elements such as diodes and transistors. The first microprocessor was presented in 1971 by Intel. It had 2300 transistors on a 3×4 mm area, with each transistor having a length of $10 \, \mu$m. Nowadays the size of single parts of circuits has been reduced to a remarkeably small scale with the prospect of a further reduction in size. For example the graphics chip 'Hawaii' produced by the enterprise 'Radeon' in 2013 contains

Frederick Guthrie

6.2 million transistors with a length of 28 nm on an area of 438 mm^2, hence the linear size of the transistors has been reduced by roughly a factor of thousand over 40 years. While today's semiconducting electronic elements span over a length of the order of one hundred atom radii, the next big step, which might be the production of electronic devices of a different kind, will lead to sizes of the order of only a few atoms. There is already ongoing research on devices consisting of single molecules [6, 7]. In these devices rectification effects have been predicted and experimentally confirmed. However, the mechanisms causing this rectification are yet to be fully understood. It is unclear whether the originally proposed mechanism is the cause and even whether it contributes at all. The controversy is challenging to solve experimentally, because elements of the mechanisms are difficult to separate physically, so one cannot rule out contributions from any of them. The author contributes to the discussion by artificially separating the elements in his simulations and testing them for their ability to cause the observed effect, as well as proposing a new mechanism [2].

On the mesoscopic scales and nanoscales of devices encountered in industrial production and research quantum mechanical effects influence the electric currents significantly. Thus one needs to check the devices for their electronic properties. This is done in environments where such a device is separately coupled to a source and drain via two leads. There, the electrical current in response to applied voltages between source and drain is studied. Theoretical analysis guides the experiments on the search for suitable devices with the requested properties. However, the systems are still too big to solve the full quantum mechanical problem exactly.

So in order to study the influence of quantum effects on the electric cur-

rents running through nanodevices theoretically, different approaches have been developed. Beyond the Born-Oppenheimer approximation of stationary cores and mobile electrons people reduced the full interaction to sets of interactions relevant for the effects they wanted to study. Within the resulting models Landauer [8, 9] and Büttiker [10] developed a formalism to analytically calculate the direct currents through extended structures of arbitrary shape.

Their work builds upon time-dependent scattering theory introduced by Lippmann and Schwinger [12]. However interactions may only appear implicitly within their approach. This is valid for extended metallic devices where interactions are screened by electrons and charge carriers therefore act like free, interactionless particles. For small devices the effective dimensionality reduces and screening gets weaker, hence interactions play a greater role. Meir and Wingreen formally solved this problem in 1993 [13]. In practice, their solution often has to be applied in perturbation theory. The resulting current is expanded in some small parameter which connects the system under considera-

Scanning transmission electron microscopy image of a Pt/ZnO nanoneedle shottky diode, published in Ref. [11]. The contrast is directly related to the atomic number (Z-contrast).

tion to one of the few exactly solvable systems. This confines the set of models one can investigate suggesting the application of complementary approaches.This work is based on such an approach in the form of numerical methods. With increasing computational power available numerical simulations have become important. They allow to investigate the systems in different parameter regimes and allow for either independent crosschecks with analytical predictions or comparisons between predictions made from assumed models and experiments where the analytical methods fail. An example for the latter case is the author's work on rectifying molecules [2].

The most important methods that were developed in this context are the density functional theory (DFT) [14, 15], quantum monte carlo (QMC) [16, 17, 18, 19, 20, 21, 22] and numerical renormalization group (NRG) [23], which has later been generalized to the density matrix renormalization group

(DMRG) [24]. The latter algorithm is tailor-made for one-dimensional problems and is therefore the method chosen in this thesis regarding current measurement setups on small devices. It started as a means to study ground state properties in 1992, was modified in a first attempt to account for time evolution in 2002 [25] and was used for wave packet dynamics in 2004 [26]. The first conductance calculations using DMRG variants were published in 2006 [27, 28].

Of course, these methods still have their short-comings. For the DMRG, one problem in the context of this work is that of the simulation of sufficiently large baths acting as source and drain due to limitations in storage and computational power. As a result, the steady states one encounters in experiments are only reproduced in very rough approximations. Therefore there is an uncertainty in theoretical predictions on the current measured in steady states. A solution to this is provided by the author [3] by introducing a new
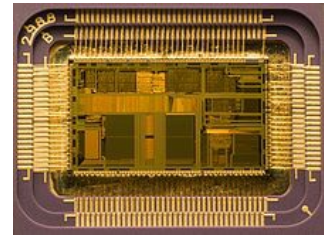
An integrated electronic circuit.

type of drain through energetic damping. It is shown within this thesis that this indeed produces steady states even for very small system sizes. Also, so far the traditional algorithm has only been applicable in static cases. Within this work the algorithm is extended to simulation of dynamic conditions. To achieve this, a time-dependent exponential perturbation theory is used. Amongst other advantages this allows for time-dependent driving of systems, alternating current measurements and studies of the interaction with photons or adiabatic boundary conditions when switching on currents very slowly. The results of this new algorithm are crosschecked using the required independence of the result from the choice of source type, voltage or current source. The reason for the good quality of the approximation is subsequently discussed.

To summarize, the work of the author contributes to the understanding of the basic electronic nanoelements both via numerical studies on properties required for such elements, and via providing tools which help with the study of nanodevices. Hopefully, this will ultimately lead to similar success stories as the discovery and understanding of the macroscopic counterparts of these devices.

This thesis is organized as follows: In chapter 2 the notation used in this thesis is introduced. Experiments on electric current measurements are discussed. The simplifications made by the modeling of the measurement setups are explained. Subsequent to this it is outlined how to simulate the process of the measurement within the modeled setup. In chapter 3 the

numerical techniques used in the framework of this work are presented and explained. The presentation starts with an approach to treat noninteracting systems in a single particle picture in order to diagonalize them exactly. Then the ideas behind the different DMRG variants used in the context of this work and provided by Peter Schmitteckert are restated. The parser of these DMRG tools is also included within the author's implementation of the approach on noninteracting systems in order to allow the handling of common input files. In the chapters 4–6 results on the author's work are presented. In chapter 4 the interest in simple models of molecular rectifiers is motivated. Then models of proposed mechanisms are revisited and they are tested for their ability to cause rectification. The chapter continues with the presentation of a new ingredient for rectification embedded in another simple model and of its potential to be physically relevant. Chapter 4 finishes with a simulation of a bridge rectifier as a first device built on the proposed rectification effect. Chapter 5 reports on the author's implementation of time-dependent exponential perturbation theory which allows for fully time-dependent Hamiltonians. First the reader is reminded of the basics of time-dependent exponential perturbation theory. Then the terms needed for a quality check of the implementation up to second order in the perturbation are calculated. Using the results of the quality check it is shown that terms of second order and beyond can be neglected in the calculation. An application of this in form of different shapes of an adiabatic current switch-on is discussed. Chapter 6 is about the author's work on steady state current simulations in finite one-dimensional systems. After an illustration of the problem, the idea is imparted and results are shown for a toy model which is used to test the proposal. Finally, conclusions are presented in chapter 7.

Chapter 2

Modeling the experiment

The purpose of theoretical studies and simulations is to make predictions for experiments or to explain the outcome and gain understanding of experiments. Therefore, the experimental situation needs to be mapped to a mathematical model which keeps only the key properties determining the experimental result while neglecting the unimportant details. In this work the situation for transport experiments through nanostructures is simulated and studied. To be more precise, the experimental setups under regard consist of a left and a right lead attached to two separate baths. The leads are coupled to a structure whose transport properties are to be investigated. In Sec. 2.2 three examples for this class of experimental setups are discussed. The aim of this chapter is to lead the reader on the route from the mentioned experiments, via the process of mapping the experiments, to the theoretical models and the simulations. The basic assumptions are given in Sec. 2.1 as a starting point. Then the general setting for the mentioned class of experiments is translated into a specific class of models in Sec. 2.2. Also some time is devoted revisiting the most basic model of that class, motivated by the ambition to keep models as simple as possible while still reproducing the desired effects. This ambition suggests that the models used will be close to this minimal model.

In Sec. 2.3 the attempt to replicate the processes happening during the measurement is explained. The explanation includes the definition of the theoretical quantity 'electrical current' which is calculated during the simulation as well as a guide to its extraction from simulation. The quantity that is calculated in theory and simulations is also compared to the quantity measured in experiment, and differences are commented on.

2.1 The basic assumptions and notation in this work

The experiments discussed in this thesis take place on the scale of a few nanometres, see the experiments discussed in Sec. 2.2. This fact necessitates the use of quantum mechanics to describe the outcome of such experiments. Therefore the language of second quantization is applied in the scope of this work. The creation and annihilation operators are denoted by $\hat{c}_x^\dagger$ and $\hat{c}_x$ with lower indices containing information like position, energy band, momentum, spin and so on.

The quantity of interest is the expectation value of the measurement. The calculated current expectation values are often referred to as 'resulting currents' for convenience. The experimental setups are assumed to consist of two baths at different chemical potentials with two leads attached, which are connected to a structure at the quench at time $t = 0$. The two baths are considered to be at their respective equilibrium at zero temperature before they are connected via leads and structure, meaning that the leads are simulated starting from their respective ground states. It is assumed that the systems consisting of the two leads and the structure are closed, meaning that pure states $|\Psi\rangle$ are simulated. The influence of baths on the system is either neglected or incorporated into properties of the Hamiltonian $\hat{\mathcal{H}}$ of the system. Also only the conduction band is simulated, and only the fully polarized limit is considered, i.e. the spin is neglected. The electrical charge defined as

$$\left\langle \hat{Q} \right\rangle = -e \sum_{x'=-\frac{M}{2}}^{\frac{M}{2}} \left\langle \hat{c}_{x'}^\dagger \hat{c}_{x'} \right\rangle,\tag{2.1}$$

where M is the system size and e is the absolute value of the electron charge, is conserved in the simulations.

The connecting area between structure and leads is supposed to be small, $k_F a \ll 1$, with a the diameter of the area. Therefore the systems are treated as one-dimensional, see the discussion in Sec. 2.2. Although one-dimensional systems in general show Luttinger liquid behaviour [29], a Fermi liquid language [30, 31, 32, 33] is used throughout this thesis, i.e. the annihilation and creation operators obey Fermi statistics.

Energies are given relative to the Fermi energy of a system without external voltage applied and at half filling. Systems are considered to be at half filling unless stated otherwise. The electrochemical potentials are refered to as chemical potentials throughout this thesis, and an inclusion of electrostatic potentials in the definition of the chemical potential is implied.
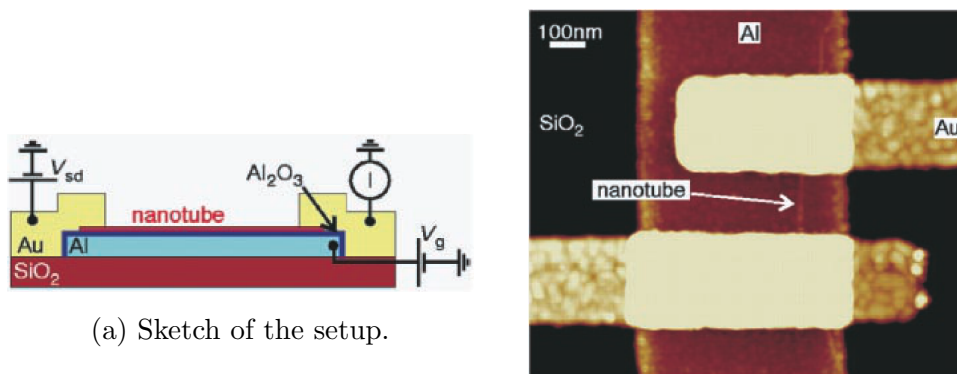
(a) Sketch of the setup.

(b) Scanning tunneling microscope picture.

Figure 2.1: Field effect transistor built of a carbon nanotube, taken from Ref. [34]. The nanotube is put on an insulator and attached to two leads connected to two electron reservoirs, a source and a drain. The gate voltage of the transistor is denoted by V_g, the applied voltage between source and drain by V_{sd}.

In this work the system size is finite, and hard wall boundaries are used. As a last note, this thesis does not differ between elementary particles and quasiparticles, and both kinds of particles are called particles for simplicity.

2.2 From quantum mechanical devices to their theoretical models

When looking for smaller electronic circuits, there is ongoing research on a huge variety of realizations of the basic ingredients like diodes and transistors, with each one needing different experiments to probe its properties.

2.2.1 Examples of relevant experiments

Examples of different realizations are given in Ref. [34, 35, 36] and shown in Figs. 2.1–2.3. In the situation shown in Fig. 2.1, a nanotube is used as electronic device, namely as field transistor [34]. In the measurement, a voltage source and an amperemeter connected to a second bath are wired to a gold lead each. The gold leads are then connected electrically via said nanotube placed on an insulating surface. There is an aluminium layer below the insulating Al_2O_3 layer, which is coupled to another voltage source. This voltage

Figure 2.2: STM picture of a one electron transistor built of a two dimensional electron gas (2DEG) and metallic gates, taken from ref. [35]. Grey areas on the top and bottom are the leads of the 2DEG. White areas are the metallic gates. The gate on the right and the top and bottom gate on the left are used to control the tunneling barrier between leads and the grey quantum dot in the middle. The gate in the middle left is used to adjust a gate voltage. The 2DEG is realized on the border of a GaAs- and a AlGaAs-compound.

source is used to tune the distribution of the electrons in the nanotube, acting as a gate voltage.

Carbon nanotubes like the one used in this experiment usually are built out of graphene layers. The layers are rolled in order to form tubes. There are several ways to roll them. One distinguishes between different directions relative to the carbon lattice in which the layers are rolled and the number of times the layer is wrapped around itself. The direction of rolling then decides whether the nanotube shows metallic, insulating or semiconducting behavior [37].

Another relevant system [35], a one electron transistor, consists of a two-dimensional electron gas (2DEG), and is shown in Fig. 2.2. The transistor is realized as a quantum dot coupled to two leads, with a gate voltage controlling the properties of the dot.

The 2DEG forms at the interface between gallium arsenide (GaAs) and an aluminium gallium arsenide (AlGaAs) layer, followed by an additional, n-doped AlGaAs layer [38]. The AlGaAs is a GaAs structure, where a not specified amount of gallium is substituted with aluminium. Since the AlGaAs has a larger band gap than GaAs, see e.g. Ref. [39], electrons from the doped energy level can move to the conduction band of the GaAs where
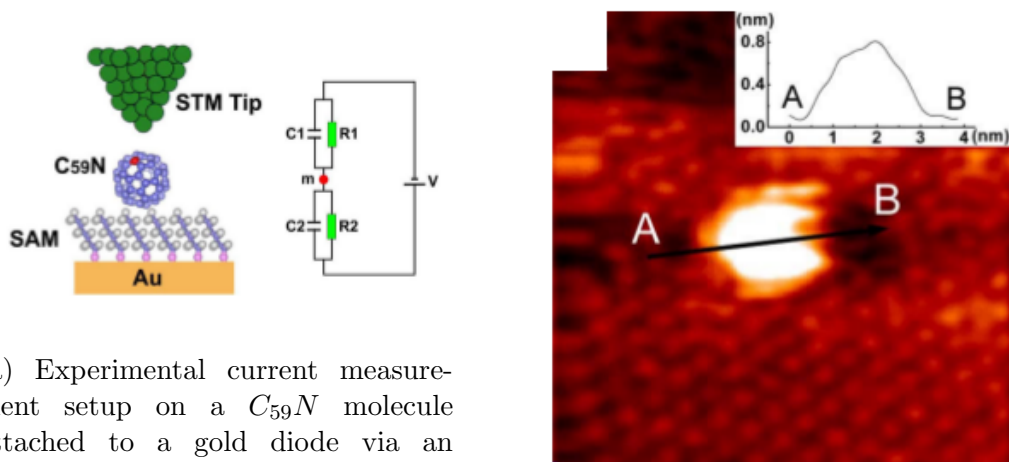
(a) Experimental current measurement setup on a $C_{59}N$ molecule attached to a gold diode via an alkanethiol self assembled monolayer (SAM). Voltage was put between gold diode and the scanning tunneling microscope (STM) tip. Schematic diagram on the right hand side.

(b) STM picture of the molecule on the SAM. In the top right corner, there is a line profile shown along the line between A and B.

Figure 2.3: The setup of a molecular current measurement, taken from Ref. [36].

they are confined to the border of the compound by a potential formed due to their interaction with the dopant atoms, see e.g. Refs. [40] and [41]. Therefore, GaAs hosts electrons in its conduction band which cannot move perpendicular to the surface, hence one finds a 2DEG. Application of metal electrodes on top of the AlGaAs and GaAs mixtures leads to a structure inside the 2DEG. By setting the electrodes to chemical potentials different from the one in the GaAs mixture, an electric field is created below the electrodes which is felt in the 2DEG and forces electrons out of the regions below the electrodes. In this way structures like one-dimensional leads or quantum dots can be achieved within the 2DEG. Parameters of the structures like the tunneling between different parts can be controlled by the variation of the different electrode chemical potentials.

The third example of relevant experiments [36], namely current measurements on molecules, is seen in Fig. 2.3. In the past molecules were defined as the smallest particle of a pure chemical substance that still keeps the properties of the substance. In that sense, molecules are a natural choice in the search for smaller devices with given electric properties. In Fig. 2.3 there is a single $C_{59}N$ molecule attached to a gold electrode via a substrate. The measurement takes place using a STM tip as second electrode as described above.

As pointed out in Ref. [42] the idea of molecular electronic devices developed from electron transfer research within molecules [43, 44, 45]. The same molecular structure that served as a model system in this research area [46, 47] was proposed in Ref. [6] as a possible molecular diode. The first current measurements on molecules used multilayered molecular films and monolayers of molecules [48] created via the Langmuir-Blodgett (LB) technique. The metal electrode was dipped into a liquid whose surface was covered with the molecules. Then a bias voltage was applied between the electrode and a scanning tunneling microscope (STM) which served as second electrode, and the current flow was measured with an amperemeter. Nowadays currents can also be measured through single molecules using the mechanically controlled break junction technique [49, 50] (MCB). Two electrodes with an LB film between them are attached to a piezo element which bends under applied voltage. The bending then opens or closes a gap between the electrodes. This way the number of molecules connecting them is adjustable. The point of only a single molecule connecting the electrodes then is fine tuned using conduction measurements.

2.2.2 Modeling the general pattern of the presented examples

Although very different in their details, there is common ground between the named experiments. All of them are two terminal transport setups. They include two different electron reservoirs or baths kept at different chemical potentials. Two macroscopic leads connect one bath each to a very small structure, which is much smaller than leads or bath. After the voltage is applied, a current flows between the baths and is measured in a measurement device in one of the leads. An instructive introduction into calculations for such setups is given e.g. in Ref. [51].

This general pattern, which is sketched in Fig. 2.4, is described by a theoretical model in the following lines. The starting assumption is that the diameters of the areas where structure and leads connect are small. This means that $k_F a \ll 1$ with Fermi wave vector k_F and a being the diameter of the coupling areas. This assumption causes a restriction to one single transverse transport channel. The result is a description of the leads as one-dimensional chains without interaction. This line of reasoning is shown more explicitly in the simplifying calculation performed in the next paragraph.

The coupling area transverse to the current flow is approximated by a box potential with infinitely high potential walls [52]. The transverse part of propagating waves must be of the form $\sin(k_x x)$ for the transverse direction
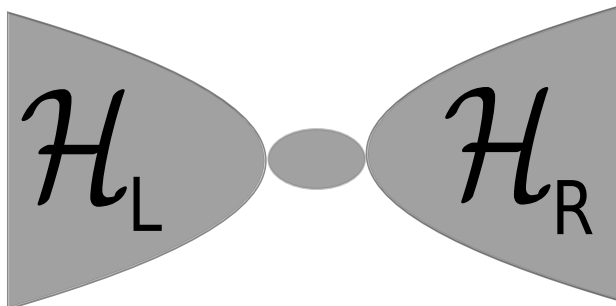
Figure 2.4: The situation modeled in this thesis. The oval blob in the middle represents a structure, probe or system under investigation. It is coupled via few atoms to macroscopic leads. Only the ends of the leads, the round grey areas on the left and the right of the structure, are shown in this sketch. For simplicity, the model includes the effects of the baths in the leads.

x, with the hard wall boundary conditions giving $2k_x a = n\pi$, n integer. The time-independent Schrödinger equation yields for the energy contribution from the transverse direction

$$E_x(n) = \frac{\hbar^2 k_x^2(n)}{2m} = \frac{\hbar^2 n^2 \pi^2}{8ma^2}. \tag{2.2}$$

The difference between the lowest two energies, and thus the energy needed to excite propagating particles in the transverse direction, is

$$\Delta E_x = \frac{3\pi^2 \hbar^2}{8ma^2}, \tag{2.3}$$

The highest energy E_F available in longitudinal direction is supposed to be much smaller than this transverse energy difference, meaning that no energy is available to excite the particles in transverse direction. This means that

$$\frac{k_F^2}{2m} \ll \frac{3\pi^2}{8ma^2}, \tag{2.4}$$

and as a consequence,

$$k_F a \ll 1. \tag{2.5}$$

In this limit the energy needed for excitations in transverse directions exceeds the excitation energy available. Higher excitations are frozen out. An analogous discussion is valid for the second transverse direction y. Particles therefore all have the same behavior in transverse directions, described by

the same transverse quantum numbers k_x and k_y. This means that they are all situated in the same transverse channel described by the lowest transverse quantum numbers, and only this one transverse channel contributes to the current. As a result the structure is coupled to only one state of the lead. An orthogonal basis of the Hamiltonian of the lead which has the one state that couples to the structure as basis state automatically yields a tight-binding Hamiltonian without interactions, as is shown at the end of this section. To summarize, the assumption of a small connection between structure and leads enables the description of a lead by a one dimensional tridiagonal so-called tight binding Hamiltonian without interactions yielding Hamiltonians for the left (L) and the right (R) lead

$$\hat{\mathcal{H}}_{\mathrm{L}} = -J \sum_{\nu=-\frac{1}{2}}^{\frac{1}{2}} \sum_{x=-\frac{M}{2}}^{-2} \left(\hat{c}_{x,\nu}^{\dagger} \hat{c}_{x+1,\nu} + \hat{c}_{x+1,\nu}^{\dagger} \hat{c}_{x,\nu} \right),$$

$$\hat{\mathcal{H}}_{\mathrm{R}} = -J \sum_{\nu=-\frac{1}{2}}^{\frac{1}{2}} \sum_{x=1}^{\frac{M}{2}-1} \left(\hat{c}_{x,\nu}^{\dagger} \hat{c}_{x+1,\nu} + \hat{c}_{x+1,\nu}^{\dagger} \hat{c}_{x,\nu} \right). \tag{2.6}$$

M is the system size, and ν sums over the spin degree of freedom. Neglecting inhomogeneities in the leads yields a constant nondiagonal element $-J$ for the Hamiltonians used in this work, which is also called hopping amplitude.

This form of the Hamiltonian is obtained via an orthonormalization using the Gram-Schmidt method [53] with respect to the state the structure couples to. In the new basis the Hamiltonian has the form of a Hessenberg matrix, i.e. the matrix elements h_{ij} vanish for $i > j + 1$. This is true since the eigenstates are expressed exclusively via the previously orthonormalized states and the original state. On top of that, the Hamiltonian has to be hermitian hence being a tridiagonal matrix in the chosen basis. This can be seen e.g. from a comparison to the Krylov space construction in appendix A.3.3. The hermiticity requirement sets all matrix elements beyond the elements of the first off-diagonal line to zero.

2.2.3 Introduction of the noninteracting resonant level model

For the simplest model of a probe coupled to two leads described by tight-binding Hamiltonians, the structure can be replaced by a single site with again no interactions between electrons on the site and any other electrons. When omitting the bath, the resulting Hamiltonian for the simplest case of
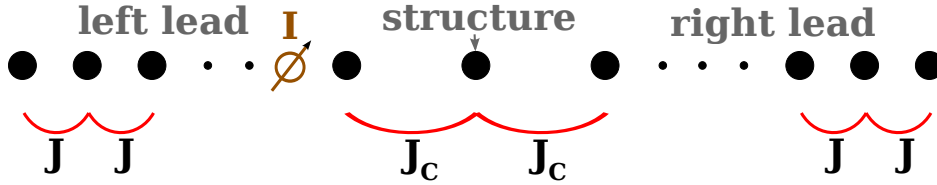
Figure 2.5: Drawing of the RLM. The red lines denote the hopping elements included in the Hamiltonian used. J and J_c are the hopping parameters of the system. As in Fig. 2.4 the baths are included in the leads.

negligible spin degree of freedom, or the fully polarized limit, reads

$$\hat{\mathcal{H}} = \hat{\mathcal{H}}_{\mathrm{L}} + \hat{\mathcal{H}}_{\mathrm{R}} + \hat{\mathcal{H}}_{\mathrm{L/R}} + \hat{\mathcal{H}}_{\mathrm{g}},$$
$$\hat{\mathcal{H}}_{\mathrm{L/R}} = -J_c \left(\hat{c}_0^\dagger \hat{c}_1 + \hat{c}_1^\dagger \hat{c}_0 \right) - J_c \left(\hat{c}_{-1}^\dagger \hat{c}_0 + \hat{c}_0^\dagger \hat{c}_{-1} \right),$$
$$\hat{\mathcal{H}}_{\mathrm{g}} = eV_g \hat{c}_0^\dagger \hat{c}_0. \tag{2.7}$$

Here, $\hat{\mathcal{H}}_{\mathrm{L/R}}$ accounts for the tunneling between structure and the first sites of the two leads and V_{g} is a gate voltage applied to the structure. The electron charge is denoted by e. For the remainder of the thesis $V_{\mathrm{g}} = 0$. Since all effects discussed in this thesis can be observed without spin-spin interactions, only models in the fully polarized limit are used, leading to spinless fermions. At the end, a structureless probe is attached to two chains. This model is named noninteracting resonant level model (RLM), sketched in Fig. 2.5. Its name stems from the resonance ocurring in a narrow energy range, which can be observed as a transmission probability of 1 for particles in that energy range. Since the RLM is noninteracting its exact eigenbasis is known and the current voltage characteristics can be calculated analytically, as has been done e.g. in Ref. [54]. Many theoretical models are small extensions of the RLM due to the ambition to reduce a problem as much as possible without losing the effects under investigation. The RLM is broached as a toy model to test a new method in chapter 5 and as noninteracting limit of a model proposed in chapter 3.

2.3 Measurements of electrical currents

In this section, the way the current is created and the exact definition of the measured quantity are discussed with focus on transfer to theory. First the current operator is defined. Then different ways to cause a current flow in a theoretical model are presented, and their differences are pointed out. The

discussion also involves a derivation of the current voltage statistics for the RLM in Sec. 2.3.4.

2.3.1 Definition of the electrical current operator

In experiments, current measurements usually are performed by inclusion of an amperemeter in the electronic circuit. Amperemeters often measure potential differences at left and right side of a small ohmic resistance, which then allows for reconstruction of the current via Ohm's law $U = RI$. The theoretical treatments presented here do not want to reconstruct this way of measurement. First, not all of the influences on the ohmic resistance, including electron phonon interactions, interactions with impurities and electron electron interactions, can be written down in a model that is supposed to be simple. Then, the current is only measured this way in experiments because there is no direct access to the movement of electric charges in the wire. Instead the current is accessed via its definition in the continuity equation as the change of electric charge over time, see e.g. Ref. [55]:

$$\frac{\mathrm{d}\left\langle \hat{Q} \right\rangle (\vec{x}, t)}{\mathrm{d}t} + \vec{\nabla} \left\langle \vec{\hat{j}} \right\rangle (\vec{x}, t) = 0, \tag{2.8}$$

with charge operator $\hat{Q}$ and current density operator $\vec{\hat{j}}$. In one dimension this reduces to

$$\frac{\mathrm{d}\left\langle \hat{Q} \right\rangle (x, t)}{\mathrm{d}t} + \left(\left\langle \hat{I}_r \right\rangle (x, t) - \left\langle \hat{I}_l \right\rangle (x, t) \right) = 0. \tag{2.9}$$

The formula expresses that the change of electric charge at a certain position x adds up with the difference between net current flowing to the right and net current flowing in from the left to zero. Not the difference in currents is of interest but the net current flow to the right. Therefore the equation is summed over all sites to the left, starting from position x. Because of $\langle \hat{I}_l \rangle (x) = \langle \hat{I}_r \rangle (x - 1)$ and the hard wall boundary conditions, which state that there is no current from the left at the leftmost site, the result reads for the expectation value $\langle \hat{Q}_x \rangle$ of the accumulated charge up to position x

$$\left\langle \hat{I}_r \right\rangle (x) := \left\langle \hat{I}_x \right\rangle = -\frac{\mathrm{d}\left\langle \hat{Q}_x \right\rangle}{\mathrm{d}t} = -\frac{i}{\hbar} \left\langle \left[\hat{\mathcal{H}}, \hat{Q}_x \right]_- \right\rangle. \tag{2.10}$$

In the last step the Ehrenfest theorem was used to replace the time derivative. $\langle \hat{I}_x \rangle$ is the net current between site x and site $x + 1$. The charge is expressed

in terms of the number of particles left of position $x + 1$ via $\hat{Q}_x = -e\hat{N}_x$. This gives

$$\left\langle \hat{I}_x \right\rangle = \frac{ie}{\hbar} \left\langle \left[\hat{\mathcal{H}}, \sum_{x'=-\frac{M}{2}}^{x} \hat{c}_{x'}^\dagger \hat{c}_{x'} \right]_- \right\rangle. \tag{2.11}$$

The RLM consists of nearest neighbor hopping and density terms. If only those terms are present in the vicinity of x^1, one finds

$$\left[\hat{\mathcal{H}}, \sum_{x'=-\frac{M}{2}}^{x} \hat{c}_{x'}^\dagger \hat{c}_{x'} \right]_- = 2i \left(J_{x+1,x} \mathrm{Im} \left\{ \hat{c}_{x+1}^\dagger \hat{c}_x \right\} \right), \tag{2.12}$$

with $2i\mathrm{Im}\{\hat{c}_{x+1}^\dagger \hat{c}_x\} = \hat{c}_{x+1}^\dagger \hat{c}_x - \hat{c}_x \hat{c}_{x+1}^\dagger$. In the derivation of this formula, the anticommutator relations for the ladder operators lead to commutator relations for combinations of ladder operators,

$$\left[\hat{c}_z^\dagger \hat{c}_x, \hat{c}_y^\dagger \right]_- = \hat{c}_z^\dagger \delta_{x,y}$$
$$\left[\hat{c}_z^\dagger \hat{c}_x, \hat{c}_y \right]_- = -\delta_{z,y} \hat{c}_x$$
$$\rightarrow \left[\hat{c}_x^\dagger \hat{c}_y, \hat{c}_z^\dagger \hat{c}_w \right]_- = \hat{c}_x^\dagger \hat{c}_w \delta_{y,z} - \hat{c}_z^\dagger \hat{c}_y \delta_{x,w}. \tag{2.13}$$

$J_{x+1,x}$ corresponds to the value of the hopping between site x and $x+1$ where the current is calculated. This leads to a net current flow of [55]

$$\left\langle \hat{I}_x \right\rangle = -\frac{2e}{\hbar} J_{x+1,x} \mathrm{Im} \left\{ \left\langle \hat{c}_{x+1}^\dagger \hat{c}_x \right\rangle \right\}. \tag{2.14}$$

2.3.2   Application of a bias voltage

The next step after the definition of the current for the simulation of experiment is to model the way this current is created. In experiments, the leads usually are at equilibrium with the structure and at the same chemical potential as the structure. To generate the current, a connection between the leads and the two baths at different chemical potentials which act as source and drain is established. The reaction of the leads to the bath then depends on the properties of the leads, as well as the properties of the bath which is assumed to be large and metallic. The leads are divided into metallic and semiconducting leads. In metallic leads the energy bands are shifted when connected to the bath, while in semiconductors the key effect is a change in particle density within the leads. The next two paragraphs give a short explanation of these different effects.

---

[1]Since the general form of the investigated models contains noninteracting tight-binding leads, chosing a position x within the leads will yield this form of the current.

Behavior of the leads upon connection with the baths

If the leads are metallic, particles moving from source to lead will add electric charge to the lead. Due to the high number of mobile particles in metals [56] the charge is screened within the lead. The additional charge is located at the boundaries of the lead. Due to the displacement of the particles needed in order to screen the charge the energies in the metallic lead now are shifted, resulting in shifted energy bands. At the same time the amount of particles that actually move to the lead until the chemical potentials in lead and bath coincide can be neglected in comparison with the charge carriers in the leads. As a result, the energy band of the metallic lead will change so that chemical potential of bath and lead will coincide without noticeable change in the number of quasiparticles in the lead. The resulting energy level adjusting is found e.g. in Ref. [38]. The process of particle exchange happens between lead and structure through a much weaker link. One approximates the adaption of the lead to the bath as instantaneous on the relevant timescale in the structure lead dynamics.

For semiconducting leads the situation is different and more complicated, see Ref. [38] for details. Only few charge carriers are available. Depending on the details of lead and bath, the lead bath contact can be e.g. ohmic or a shottky diode. Upon contact of lead and bath, if the energy band of the lead is deformed, it is only deformed significantly in the vicinity of the bath. This is due to the smaller amount of charge carriers available for the screening. If electric current is allowed to flow, the energy band is filled up to the Fermi energy of the bath without changing its energy globally. Since the initial carrier density in the lead is small the number of additional particles added from the bath cannot be neglected. Therefore the density of charge carrying particles will change.

Modeling the leads upon connection with the bath

When simulating the situation numerically, the leads are represented by small chains due to limitations in computational power. For the same reason, the baths are omitted and the leads themselves are treated as source and drain, whereby the effects of the baths are included in the properties in the leads. For the two different situations described above, two different methods are needed, see Fig. 2.6. In both cases the problem is separated in time into two different parts. These parts can be described in short as initial state preparation for the equilibrium situation before the quench and time evolution during the nonequilibrium situation after the quench. As a matter of notation, the system before the quench is described by a Hamiltonian

(a) Scattering theory situation, modeled by inclusion of a voltage term in $\hat{\mathcal{H}}_s$.

(b) Situation in metallic leads, modeled by bias in $\hat{\mathcal{H}}_t$.
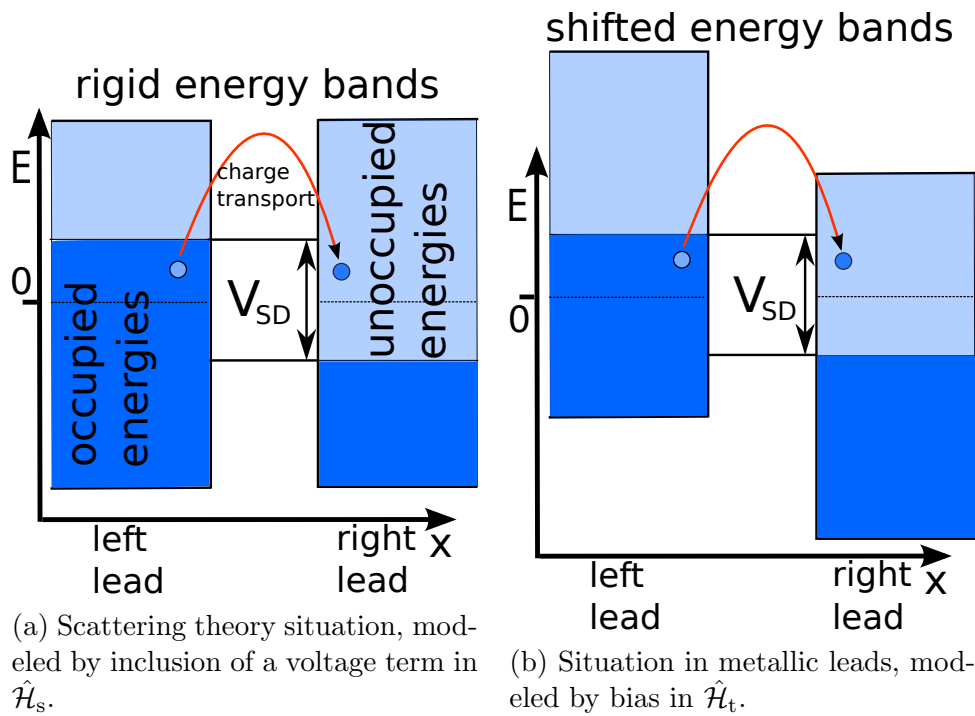
Figure 2.6: Energy bands of the two leads attached to the structure for two physically different situations leading to current flow through the structure. The illustrated situation happens right after the quench. The leads are connected via the structure, whose energy levels depend on details of the model and are not sketched here.

$$\mathcal{H} = \mathcal{H}_{\mathrm{L}} + \mathcal{H}_{\mathrm{L/R}} + \mathcal{H}_{\mathrm{R}}$$

situation
in
scattering
theory
$$\mathcal{H}_{\mathrm{s}} = \mathcal{H} + \mathcal{H}_{\mathrm{V}}$$
$$\mathcal{H}_{\mathrm{t}} = \mathcal{H}$$

situation
in
metallic
leads
$$\mathcal{H}_{\mathrm{s}} = \mathcal{H}$$
$$\mathcal{H}_{\mathrm{t}} = \mathcal{H} - \mathcal{H}_{\mathrm{V}}$$

equilibrium   0   non-equilibrium   time

initial state   quench
preparation   time evolution
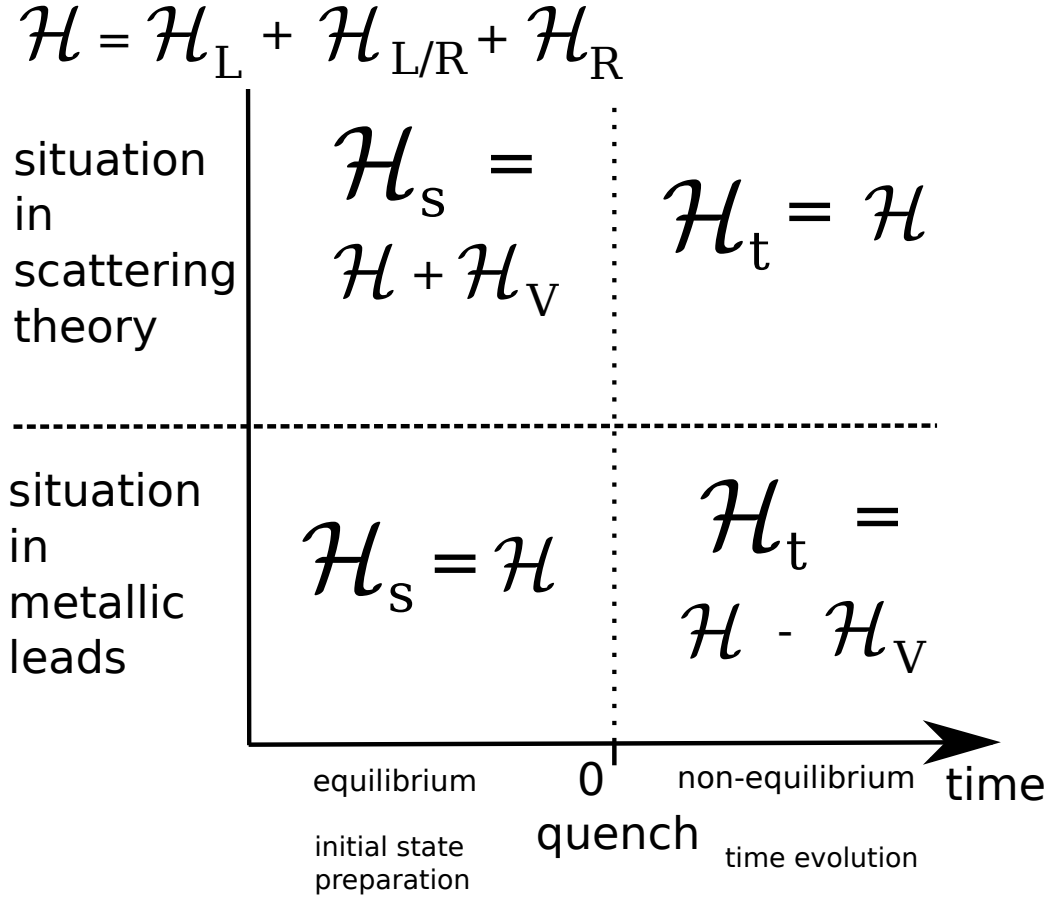
Figure 2.7: Overview of the composition of the initial Hamiltonian $\hat{\mathcal{H}}_{\mathrm{s}}$ and the time evolution Hamiltonian $\hat{\mathcal{H}}_{\mathrm{t}}$, depending on the situation one intends to simulate. The effect of the inclusion of the voltage term $\hat{\mathcal{H}}_{\mathrm{V}}$ in either $\hat{\mathcal{H}}_{\mathrm{s}}$ or $\hat{\mathcal{H}}_{\mathrm{t}}$ on the density or the shift of energy bands is seen in Fig. 2.6.

labeled $\hat{\mathcal{H}}_{\mathrm{s}}$, while the system after the quench is described by $\hat{\mathcal{H}}_{\mathrm{t}}$. While the next three paragraphs discuss the cases in more detail, an overview on the approaches for different situations is given in Figs. 2.7 and 2.8.

The first part of the problem is the preparation of the system before the quench, which means before the system is changed on a short timescale. In the context of the experiments discussed above the quench is the process of connecting leads to the structure. This part differs from the procedure in experiments due to the need to include the effect of the baths in the Hamiltonian of the leads. The simulations model the leads as being connected to the structure before the quench, and being target of a rapid change in their electrostatic potentials at the quench. Before the quench the system

Inclusion of $\hat{\mathcal{H}}_{\mathrm{V}}$ in:	$\hat{\mathcal{H}}_{\mathrm{s}}$	$\hat{\mathcal{H}}_{\mathrm{t}}$
Induced changes in:	The initial particle density in the leads.	The energy levels in the leads.
The reason for the induced changes:	The density is obtained as ground state of $\hat{\mathcal{H}}_{\mathrm{s}}$.	The energy levels influence the time evolution.

Figure 2.8: Overview of the various possibilities to use the voltage term $\hat{\mathcal{H}}_{\mathrm{V}}$. The effect of the inclusion of the voltage term $\hat{\mathcal{H}}_{\mathrm{V}}$ in either the initial Hamiltonian $\hat{\mathcal{H}}_{\mathrm{s}}$ or the time evolution Hamiltonian $\hat{\mathcal{H}}_{\mathrm{t}}$ on the density or the shift of energy bands is seen in Fig. 2.6.

is assumed to be in equilibrium in its ground state. The second part is the time evolution of the system. Since the energy offset of the bands influences time evolution, effects of the bath on the energy bands are included here. In the second part, the current is measured. The evolution of the system also differs from the situation in experiment due to the concessions which have to be made to system size. Details of this are discussed in Sec. 2.3.3.

In case of semiconducting leads or reproduction of scattering theory results, an initial density distribution inequality in the two leads is needed. Therefore the electrostatic potentials in the leads before the quench are changed by a voltage term. For the case of electrostatic potentials being placed symmetrically around the chemical potential of the structure, which means $2\mu_{\mathrm{R/L}} = \pm eV_{\mathrm{SD}}$, the term

$$
\begin{aligned}
\hat{\mathcal{H}}_{\mathrm{V}} &= \left(\mu_{\mathrm{R}} \sum_{x}^{\text{right lead}} \hat{n}_x + \mu_{\mathrm{L}} \sum_{x}^{\text{left lead}} \hat{n}_x \right) \\
&= \frac{eV_{\mathrm{SD}}}{2} \left(\sum_{x}^{\text{right lead}} \hat{n}_x - \sum_{x}^{\text{left lead}} \hat{n}_x \right)
\end{aligned} \tag{2.15}
$$

is added to the Hamiltonian $\hat{\mathcal{H}}_{\mathrm{s}}$. Time evolution then is carried out without this charge imbalance or voltage term.

In case of metallic leads the energy bands of the leads have to shift relative to each other while still having the same charge carrier density. The initial state is prepared using the unmodified Hamiltonian of the system, yielding the same particle density in both leads. For time evolution, the voltage term (2.15) is subtracted from the Hamiltonian in order to change the energy bands of the leads. In the previous case the energy of the source had to be lowered in order to attract more particles to the source and to increase its filling. Here, the energy of particles in the source has to be increased to allow them to move to the drain, thus the difference in sign of the voltage term
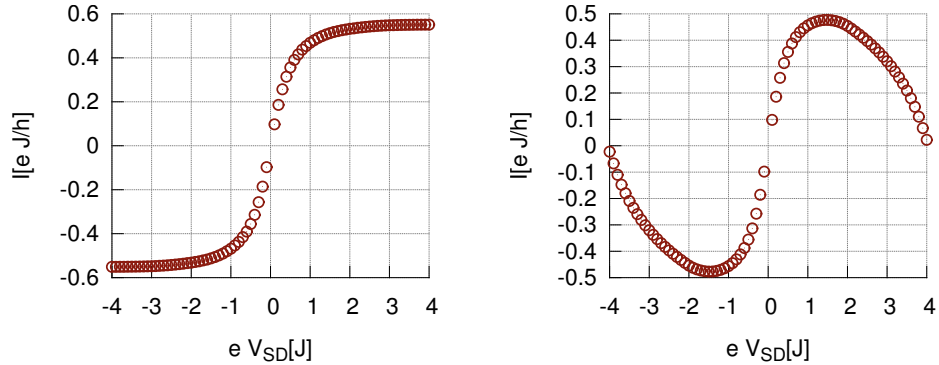
(a) Voltage term added in $\hat{\mathcal{H}}_{s}$.   (b) Voltage term added in $\hat{\mathcal{H}}_{t}$.

Figure 2.9: Current over applied bias voltage in the RLM. The system size is $M = 130$ and the lead to probe hopping amplitude is $J_{c} = 0.3J$ with J being the lead hopping amplitude.

e.g. in Fig. 2.7. This sign difference leads to positive currents for positive voltages, as shown in chapters 4, 5 and 6.

Comparison of the two prescriptions available for the leads

The two options named here correspond to two physically different processes leading to different currents, as seen in Figs. 2.9 and 2.10. An explanation for the different results between those two cases can be found e.g. in Ref. [55]. For small voltages, the two cases coincide. Their results differ most for large voltages, so it is instructive to look at the different situations in the large voltage region. In scattering theory, if the votage term is large enough, the left lead will be fully occupied with charge carriers with none available in the right lead. Therefore all possible energy channels will contribute to the current. As a result, the current saturates at its maximum value. In the other situation, for voltages larger than $eV_{\mathrm{SD}} > 4J$, the overlap between the two energy bands reduces to zero. Due to energy conservation no energy level corresponds to a wavefunction extending over the two leads and allowing for transport between left and right lead. No channel contributes to the current, so the current drops to zero. A current flow can also be created by insertion of a current source instead of the applied voltage. This case is discussed in Sec. 2.3.5.
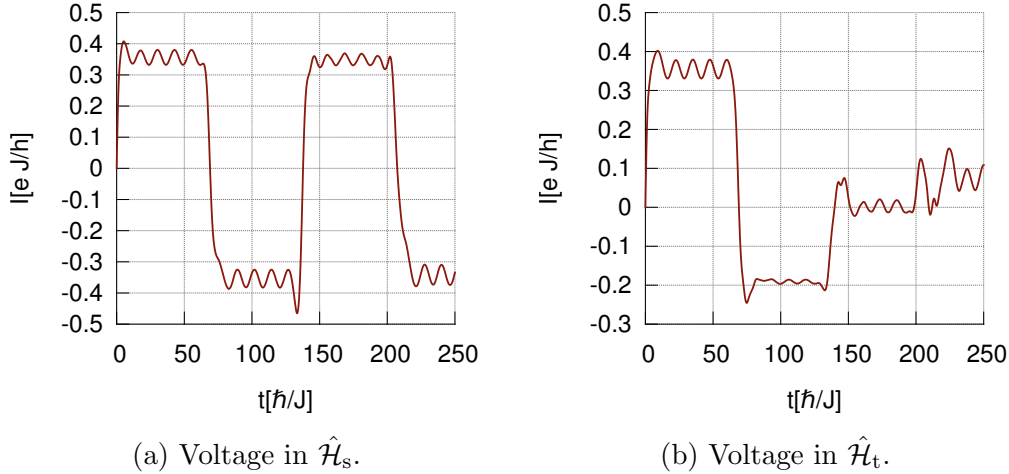
(a) Voltage in $\hat{\mathcal{H}}_{\mathrm{s}}$.

(b) Voltage in $\hat{\mathcal{H}}_{\mathrm{t}}$.

Figure 2.10: Current over time in the RLM. Parameters are system size $M = 130$, lead to probe hopping $J_c = 0.3J$ and applied bias voltage $V_{\mathrm{SD}} = 0.5J$ with J being lead hopping.

2.3.3 Extraction of electrical current values

Comparison of simulated currents with experiments

After setting up the system, the expectation value of the current operator is calculated for the chosen bias voltage. The current obtained in the described simulations differs from the current obtained in experiment for long times, see Ref. [57]. For long times the leads can no longer be regarded as baths since charge carriers, after moving through the measurement position, will see the boundaries of the system and return to the measurement position. Also, the small, finite system size of the system results in gaps between the energy levels. At half filling, the Fermi vector is $2k_F = \pi$, so the energy for states with k-momentum near the Fermi vector, $k = k_F + \Delta k$, reads

$$E = -2J \cos\left(\frac{\pi}{2} + \Delta k\right) \approx 2J\Delta k = \frac{4\pi J}{M}. \tag{2.16}$$

The energy gap is the difference of this energy and the Fermi energy $E_{\mathrm{F}} = 0$. The current shows oszillations with amplitude proportional to the energy gap and frequency being charge times voltage over $\hbar$. These oszillations look similar to Josephson oscillations between two gapped superconductors and are not present in experiments with large leads and thus vanishing gaps. The expectation values of simulated currents calculated within this work qualitatively look like the one shown in Fig. 2.10.

In experiments, the current after the quench first enters a transient regime which then decays towards a steady state. Measurements then are made in the steady state. This transient regime can be seen in Fig. 2.10 or, more prominently, in Fig. 2.11. For the RLM, the transient current decays exponentially with a decay rate Γ of $\hbar J \Gamma = 2 J_c^2$ [13]. After the transient regime, a quasi steady state or current plateau with the discussed oscillations on top of the steady state current sets in. At the return time $2tJ = M\hbar$ of charge carriers with Fermi velocity $\hbar v_F = 2J$ after the quench the current suddenly drops and the quasi steady state is destroyed. The sudden drop of the current marks the beginning of interference of the particles returning from the boundaries with the desired current.

Details on the extraction of the current

The steady state value is extracted using a fit including the oscillatory terms. The fitting range is the time interval between the decay of the transient regime and the sudden drop of the current. At the time of the fit, the charge carriers only know about the finite size of the system through the finite gap in energy between ground state and first excited state. The effect of the energy gap is averaged out by the fit. The steady state current in experiment is approximated by this extracted current. The fitting procedure has to be stopped at the drop of the current. At this point information on the boundaries of the system reaches the position where the current is calculated. Since no boundaries are encountered in experiments the result crucially differs from the experiment starting at this point in time.

Here, oszillations and interferences are mentioned as effects caused by the finite size of the system. There are also other effects of the finite size of the system on the extracted current, like the even-odd effect or a density shift in the leads. They are discussed extensively in Ref. [55] and are beyond the scope of this work. They are accounted for by an investigation of the dependence of extracted current on the system size.

2.3.4 Electric current in the noninteracting resonant level model

Since the RLM does not involve interaction, its electric current can be calculated analytically using the scattering ansatz proposed by Landauer and Büttiker [8, 9, 10]. The result, whose derivation is repeated here, is given e.g. in Refs. [58, 54]. Without interaction, particles with different energy do not see each other. As a consequence, it is natural to use a single particle picture. Each single particle energy channel contributes separately to the
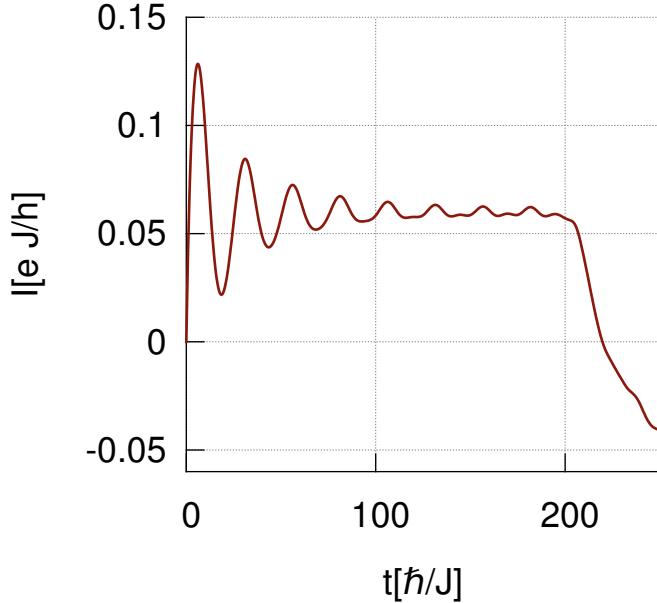
Figure 2.11: Current over time for the RLM with $M = 400$, $J_c = 0.1J$ and $V_{SD} = 0.5J$. The voltage term is added to $\hat{\mathcal{H}}_s$.

current. A derivation of this is given in Sec. 3.1. Unlike in Sec. 3.1 a scattering picture is used so time-dependence is of no interest now. In comparison to the calculation in Sec. 3.1 the time evolution operator is set to unity here. Without loss of generality the left bath is taken as the particle source. The idea is now that the voltage corresponds to occupation of higher energy levels in the left bath than in the right bath, see Fig. 2.6a in Sec. 2.3.2, but leaves the energy bands unchanged. In other words, the voltage does not enter the Hamiltonian but only the initial conditions. The assumption behind this is that the voltage is caused by the distribution function in the baths. These baths are far away from the structure. The leads do not change their energy levels at the quench but are filled up to the chemical potentials in the baths. The whole information about the chemical potential is stored in the density distribution of the incoming waves but not in their form. The assumption gives good results for small voltages $eV_{SD} \ll 2J$, a limit which is called wide-band limes, or for semiconducting leads. Therefore scattering theory is often used to obtain the linear response of the system to a small external voltage, called linear conductance. For other cases, generalizations of the method presented here are available [59].

As a result, particles with energies higher than the highest occupied

energy level of the right bath will move to the right and will scatter at the structure leading either to reflection or transmission of the particle. Since the voltage does not enter the Hamiltonian the eigenstates of the system are also not effected by the voltage, and for $M \to \infty$ are asymptotically plain waves[2] incoming from the left which are scattered at the structure. The creation operator is transformed in between the position and energy bases by

$$\sqrt{M}\hat{c}_k^\dagger = \sum_{x=-M}^{-1} \left(e^{ikx} + re^{-ikx} \right) \hat{c}_x^\dagger + d\hat{c}_0^\dagger \sum_{x=1}^{M} te^{ikx}\hat{c}_x^\dagger. \tag{2.17}$$

The parameters $t(k)$, $d(k)$ and $r(k)$ as well as the energy E_k are obtained from the eigenvector requirement

$$\left[\hat{\mathcal{H}}, \hat{c}_k^\dagger \right] = E_k \hat{c}_k^\dagger \tag{2.18}$$

by insertion of Eq. (2.17) and solution of the resulting system of equations. The current between position $x = 0$ and $x = 1$ resulting from particles traveling towards an empty lead is

$$\left\langle \hat{I}_0 \right\rangle = -\frac{2e}{\hbar} J_{1,0} \sum_k \text{Im} \left\{ \langle \Psi_k | \hat{c}_1^\dagger \hat{c}_0 | \Psi_k \rangle \right\}, \tag{2.19}$$

with $J_{1,0} = J_c$ and $|\Psi_k\rangle$ being the plane waves traveling to the right. Transformation of the ladder operators between position and energy basis using

$$\hat{c}_1^\dagger = \sum_l \hat{c}_l^\dagger U_{l,1}^\dagger,$$

$$\hat{c}_0 = \sum_m U_{0,m}\hat{c}_m,$$

$$U_{0,m} = \frac{d^*}{\sqrt{M}} = \frac{t^* J}{\sqrt{M} J_c},$$

$$U_{l,1}^\dagger = \frac{t}{\sqrt{M}} \exp(il), \tag{2.20}$$

where $U_{x,n}$ denotes the transformation matrix element between position x and energy label n, leads to

$$\left\langle \hat{I}_0 \right\rangle = -\frac{2e}{M\hbar} J \sum_k |t|^2 \text{Im} \left\{ \exp(ik) \right\}. \tag{2.21}$$

---

[2]Since the systems under consideration are large but still finite, the eigenstates are still normalized by the square root of the system size.

Writing the sum as an integration over energy via the density of states with $M\Delta k = 2\pi$ and $E_k = -2J\cos(k)$ finally gives

$$\left\langle \hat{I}_0 \right\rangle = -\frac{eJ}{2\pi\hbar} \int \mathrm{d}E_k \left|t\right|^2 . \qquad (2.22)$$

Here, one also needs to account for the distribution functions of incoming and outgoing waves since only empty states in the right lead can be occupied, and only if there is a particle with that energy in the left lead. Thus the energy range at which a net current will flow is limited, and the corrected current reads

$$\left\langle \hat{I}_0 \right\rangle = -\frac{eJ}{2\pi\hbar} \int \mathrm{d}E_k \left|t\right|^2 \left(f\left(E_k - \mu_{\mathrm{L}}\right) - f\left(E_k - \mu_{\mathrm{R}}\right)\right) . \qquad (2.23)$$

Here, $\mu_{\mathrm{R/L}}$ denotes the chemical potential in the left and right bath, respectively, and $f(E)$ is the Fermi distribution function for energy E. In this work, models of current measurement setups always assume a symmetric bias, so $2\mu_{\mathrm{R/L}} = \pm eV_{\mathrm{SD}}$ with voltage V_{SD} being caused by the difference in chemical potential between left and right bath. The energy is measured relative to the Fermi energy with no voltage applied. Since the baths are assumed to be in their respective ground states, $f(E) = \Theta(-E)$ and

$$\left\langle \hat{I}_0 \right\rangle = -\frac{eJ}{2\pi\hbar} \int_{-\frac{V_{\mathrm{SD}}}{2}}^{\frac{V_{\mathrm{SD}}}{2}} \mathrm{d}E_k \left|t\right|^2 . \qquad (2.24)$$

For large voltages $eV_{\mathrm{SD}} \gtrsim J$, one has to check from the details of the simulated setup whether the finite width of the energy bands $(4J)$ needs to be considered [57]. It can be included via modification of the integration borders, leading to

$$\left\langle \hat{I}_0 \right\rangle = -\frac{eJ}{2\pi\hbar} \int_{-\min\left\{\frac{V_{\mathrm{SD}}}{2}, 2J-\frac{V_{\mathrm{SD}}}{2}\right\}}^{\min\left\{\frac{V_{\mathrm{SD}}}{2}, 2J-\frac{V_{\mathrm{SD}}}{2}\right\}} \mathrm{d}E_k \left|t\right|^2 . \qquad (2.25)$$

From Eq. (2.18) one finds for small voltages and the Hamilton operator given

in Eq. (2.7) that

$$t = \frac{2i\sin(k)\tilde{J}_c^2}{\tilde{E}_k + 2\tilde{J}_c^2\exp(ik)}, \tag{2.26}$$

$$|t|^2 = \frac{\left(4 - \tilde{E}_k^2\right)\tilde{J}_c^4}{\tilde{J}_c^4 + \tilde{E}_k^2\left(1 - 2\tilde{J}_c^2\right)}$$

$$= a\left(\frac{4(1+a)}{4a + \tilde{E}_k^2} - 1\right), \tag{2.27}$$

$$a = \frac{\tilde{J}_c^4}{1 - 2\tilde{J}_c^2}, \tag{2.28}$$

where tilded parameters are given in units of J, so $J\tilde{O} = O$. The current then reads

$$\left\langle\hat{I}_0\right\rangle = -\frac{eJ}{h}a\left(\frac{4(1+a)}{\sqrt{a}}\arctan\frac{\tilde{V}_{SD}}{4\sqrt{a}} - \tilde{V}_{SD}\right). \tag{2.29}$$

For small $J_c \ll J$ the linear term can be neglected and the current is proportional to an arcus tangens of the voltage. It should be highlighted that the dispersion relation $E(k)$ obtained from Eq. (2.18) follows from equations for positions deep within the leads. The structure has no influence on this result, so it is valid for any choice of structure.

2.3.5 Electrical currents created by current sources

This section covers a known correspondence between the current created by voltage sources and by certain current sources in the RLM [25]. The main goal is the establishment of a connection between the current of a time-dependent system, in this case represented by a Hamiltonian including a time-dependent phase, and the current of a time-independent system. The correspondence is used in chapter 5 to test the good quality of the work on simulation of time-dependent systems presented in that chapter, in analogy to the work in Ref. [25]. The derivation of the correspondence goes along the lines of the tunneling current calculation in Ref. [60]. The situation under investigation is the one with metallic leads, so the energy bands are shifted during time evolution. Starting point of the derivation is the current expectation value

$$\left\langle\hat{I}_{-1}\right\rangle = -\frac{d\left\langle\hat{Q}_{-1}\right\rangle}{dt}. \tag{2.30}$$

This expression is now evaluated in the interaction picture, which is also called Dirac picture. The Hamiltonian of the system during time evolution reads

$$\hat{\mathcal{H}} = \hat{\mathcal{H}}_\mathrm{L} + \hat{\mathcal{H}}_\mathrm{R} + \hat{\mathcal{H}}_\mathrm{L/R} - \hat{\mathcal{H}}_\mathrm{V}, \tag{2.31}$$

and the term $\hat{\mathcal{H}}_\mathrm{L/R}$ is split from the time evolution of the operators. This means that states and operators follow the Heisenberg and Schwinger-Tomonaga equations, with starting time $t_0 = 0$,

$$i\hbar \frac{\mathrm{d}}{\mathrm{d}t} \left| \Psi(t) \right\rangle = \hat{\mathcal{H}}_\mathrm{L/R}(t) \left| \Psi(t) \right\rangle, \tag{2.32}$$

$$i\hbar \frac{\mathrm{d}}{\mathrm{d}t} \hat{\mathrm{Q}}_{-1}(t) = \left[\hat{\mathrm{Q}}_{-1}(t), \hat{\mathcal{H}}_\mathrm{L}(t) + \hat{\mathcal{H}}_\mathrm{R}(t) - \hat{\mathcal{H}}_\mathrm{V}(t) \right]_- = 0,$$

$$i\hbar \frac{\mathrm{d}}{\mathrm{d}t} \hat{\mathcal{H}}_\mathrm{L}(t) = \left[\hat{\mathcal{H}}_\mathrm{L}(t), \hat{\mathcal{H}}_\mathrm{L}(t) + \hat{\mathcal{H}}_\mathrm{R}(t) - \hat{\mathcal{H}}_\mathrm{V}(t) \right]_- = 0,$$

$$i\hbar \frac{\mathrm{d}}{\mathrm{d}t} \hat{\mathcal{H}}_\mathrm{R}(t) = \left[\hat{\mathcal{H}}_\mathrm{R}(t), \hat{\mathcal{H}}_\mathrm{L}(t) + \hat{\mathcal{H}}_\mathrm{R}(t) - \hat{\mathcal{H}}_\mathrm{V}(t) \right]_- = 0,$$

$$i\hbar \frac{\mathrm{d}}{\mathrm{d}t} \hat{\mathcal{H}}_\mathrm{V}(t) = \left[\hat{\mathcal{H}}_\mathrm{V}(t), \hat{\mathcal{H}}_\mathrm{L}(t) + \hat{\mathcal{H}}_\mathrm{R}(t) - \hat{\mathcal{H}}_\mathrm{V}(t) \right]_- = 0,$$

$$i\hbar \frac{\mathrm{d}}{\mathrm{d}t} \hat{\mathcal{H}}_\mathrm{L/R}(t) = \left[\hat{\mathcal{H}}_\mathrm{L/R}(t), \hat{\mathcal{H}}_\mathrm{L}(t) + \hat{\mathcal{H}}_\mathrm{R}(t) - \hat{\mathcal{H}}_\mathrm{V}(t) \right]_-. \tag{2.33}$$

Under time evolution of a system with no coupling between the leads and the structure, the charge in the left lead cannot change, hence the time derivative vanishes. Similar reasoning goes for the particle density in left and right lead separately and thus for the voltage term. This argument gives the reason for the time-independence of the intra lead Hamiltonians. Inserting Eq. (2.32) into Eq. (2.30) yields

$$\left\langle \hat{I}_{-1} \right\rangle = -\frac{i}{\hbar} \left\langle \Psi(t) \right| \left[\hat{\mathcal{H}}_\mathrm{L/R}(t), \hat{\mathrm{Q}}_{-1} \right]_- \left| \Psi(t) \right\rangle$$

$$= -\frac{i}{\hbar} \left\langle \Psi_0 \right| \hat{T} \exp\left\{ \frac{i}{\hbar} \int_0^t \mathrm{d}t' \hat{\mathcal{H}}_\mathrm{L/R}(t') \right\}$$

$$\left[\hat{\mathcal{H}}_\mathrm{L/R}(t), \hat{\mathrm{Q}}_{-1} \right]_- \hat{T} \exp\left\{ -\frac{i}{\hbar} \int_0^t \mathrm{d}t' \hat{\mathcal{H}}_\mathrm{L/R}(t') \right\} \left| \Psi_0 \right\rangle, \tag{2.34}$$

with time ordering operator $\hat{T}$ imposing an ordering of the operators in the Taylor expansion of the exponential function with decreasing t, i.e. the Hamiltonians at earliest times have to stand on the right. Operators at time $t = 0$ are written without explicit time-dependence. Time evolution of

each $\hat{\mathcal{H}}_{\text{L/R}}(t)$ then reads

$$\hat{\mathcal{H}}_{\text{L/R}}(t) = \exp\left\{\frac{i}{\hbar}\left(\hat{\mathcal{H}}_{\text{L}} + \hat{\mathcal{H}}_{\text{R}} - \hat{\mathcal{H}}_{\text{V}}\right)t\right\}$$
$$\hat{\mathcal{H}}_{\text{L/R}}\exp\left\{-\frac{i}{\hbar}\left(\hat{\mathcal{H}}_{\text{L}} + \hat{\mathcal{H}}_{\text{R}} - \hat{\mathcal{H}}_{\text{V}}\right)t\right\}. \qquad (2.35)$$

The use of the fact that the operators $\hat{\mathcal{H}}_{\text{L}}$, $\hat{\mathcal{H}}_{\text{R}}$ and $\hat{\mathcal{H}}_{\text{V}}$ commute with each other and that

$$\exp\left\{\frac{i}{\hbar}\hat{\mathcal{H}}_{\text{V}}t\right\} = \prod_x^{\text{right lead}}\left(\hat{\text{n}}_x\left(\exp\left\{\frac{i}{\hbar}\frac{eV}{2}t\right\} - 1\right) + 1\right)$$
$$\prod_x^{\text{left lead}}\left(\hat{\text{n}}_x\left(\exp\left\{-\frac{i}{\hbar}\frac{eV}{2}t\right\} - 1\right) + 1\right), \qquad (2.36)$$
$$\hat{\text{n}}_x\hat{\text{c}}_y^\dagger = \hat{\text{c}}_y^\dagger\left(\delta_{x,y} + \hat{\text{n}}_x\left(1 - \delta_{x,y}\right)\right),$$
$$\hat{\text{n}}_x\hat{\text{c}}_y = \hat{\text{c}}_y\hat{\text{n}}_x\left(1 - \delta_{x,y}\right),$$
$$\hat{\text{c}}_y^\dagger\hat{\text{n}}_x = \hat{\text{n}}_x\left(1 - \delta_{x,y}\right)\hat{\text{c}}_y^\dagger,$$
$$\hat{\text{c}}_y\hat{\text{n}}_x = \left(\delta_{x,y} + \hat{\text{n}}_x\left(1 - \delta_{x,y}\right)\right)\hat{\text{c}}_y, \qquad (2.37)$$

leads to

$$\hat{\mathcal{H}}_{\text{L/R}}(t) = \exp\left\{\frac{i}{\hbar}\left(\hat{\mathcal{H}}_{\text{L}} + \hat{\mathcal{H}}_{\text{R}}\right)t\right\}\left(\hat{\text{n}}_{-1}\left(\exp\left\{\frac{i}{\hbar}\frac{eV}{2}t\right\} - 1\right) + 1\right)$$
$$\left(\hat{\text{n}}_1\left(\exp\left\{-\frac{i}{\hbar}\frac{eV}{2}t\right\} - 1\right) + 1\right)\hat{\mathcal{H}}_{\text{L/R}}\left(\hat{\text{n}}_{-1}\left(\exp\left\{-\frac{i}{\hbar}\frac{eV}{2}t\right\} - 1\right) + 1\right)$$
$$\left(\hat{\text{n}}_1\left(\exp\left\{\frac{i}{\hbar}\frac{eV}{2}t\right\} - 1\right) + 1\right)\exp\left\{-\frac{i}{\hbar}\left(\hat{\mathcal{H}}_{\text{L}} + \hat{\mathcal{H}}_{\text{R}}\right)t\right\}$$
$$= \exp\left\{\frac{i}{\hbar}\left(\hat{\mathcal{H}}_{\text{L}} + \hat{\mathcal{H}}_{\text{R}}\right)t\right\}\hat{\mathcal{H}}_{\text{L/R}}'(t)\exp\left\{-\frac{i}{\hbar}\left(\hat{\mathcal{H}}_{\text{L}} + \hat{\mathcal{H}}_{\text{R}}\right)t\right\}. \quad (2.38)$$
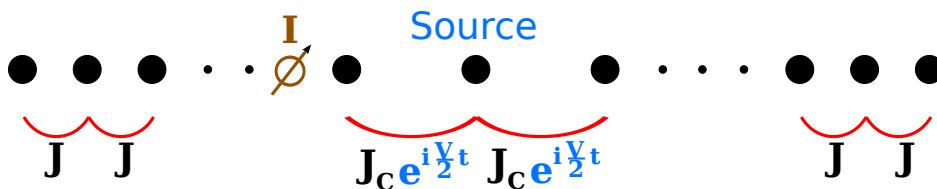
Figure 2.12: RLM with time-dependent phase acting as a current source in the system. $\hbar = 1$ and $e = 1$ in this sketch.

At this point, the whole voltage influence on time evolution of the current expectation value is hidden in $\hat{\mathcal{H}}'_{\mathrm{L/R}}(t)$, with

$$
\begin{aligned}
\hat{\mathcal{H}}'_{\mathrm{L/R}}(t) = & -J_c \exp\left\{\frac{i}{\hbar}\frac{eV}{2}t\right\}\hat{c}^{\dagger}_{-1}\hat{c}_0 \\
& -J_c\hat{c}^{\dagger}_0\hat{c}_{-1} \exp\left\{-\frac{i}{\hbar}\frac{eV}{2}t\right\} \\
& -J_c\hat{c}^{\dagger}_0\hat{c}_1 \exp\left\{\frac{i}{\hbar}\frac{eV}{2}t\right\} \\
& -J_c \exp\left\{-\frac{i}{\hbar}\frac{eV}{2}t\right\}\hat{c}^{\dagger}_1\hat{c}_0 \\
= & -J'_c\left(\hat{c}^{\dagger}_{-1}\hat{c}_0 + \hat{c}^{\dagger}_0\hat{c}_1\right) + \mathrm{h.c.}.
\end{aligned}
\tag{2.39}
$$

The same result is obtained for the modeling of a setup that does not include the voltage term in the time evolution Hamiltonian, which means that the leads do not feel the influence of source and drain in form of energy band shifts, so no voltage source is included in the model. Instead, the voltage adds a time-dependent phase to the hopping

$$
J'_c = \exp\left\{\frac{i}{\hbar}\frac{eV}{2}t\right\}J_c,
\tag{2.40}
$$

which then acts as current source in the system. The resulting model is sketched in Fig. 2.12.

Chapter 3

Numerical techniques in transport simulations involving electrical currents

So far a motivation of the work presented in this thesis and an explanation of the theoretical modeling of the current measurements were provided. In this chapter the numerical techniques used for the initial setup and the time evolution of the systems under investigation are presented.

In order to calculate any expectation values for a given system, operators need to be applied to states, and eigenstates of operators like the Hamiltonian of the system need to be found. Numerical performance of these computations –the action of operators onto states or the diagonalization of operators – requires states and operators to be expressed in vector or matrix form. In the scope of this thesis they have to be represented in a finite basis on a computer.

In the non-interacting case the Hilbert space can be written in form of a direct sum of separate spaces where the Hamiltonian and other observables of interest only act within one of the spaces. This is due to the large number of conserved quantities, like the energies, spins and momenta of each particle. The operators are expressed as matrices in this significantly smaller space. This makes numerical computations with these operators feasible and allows one to solve the problem numerically without approximations. The known formula used to solve the problem is derived in Sec. 3.1.

However, most cases of interest include interaction. The Hilbert space as the natural choice of a representation basis is then too large. Usage of symmetries and conserved quantities in this case does not suffice to reduce the problem to a manageable size. Subspaces small enough to perform computations in them can not contain all the information stored in the Hilbert

space. In numerical simulations information pertaining to the system is necessarily lost and the problem can no longer be solved exactly. In this thesis the Hilbert space of such systems is approximated by a subspace containing the most relevant information required for the description of the physical system. This subspace yields optimal approximations to exact results in the sense which is discussed in Sec. 3.3.3. The implementation of this known approximation is provided by Peter Schmitteckert in the scope of this work, and its discussion is included for the sake of completeness.

In Sec. 3.2 an overview of the approximations used to prepare the initial state is given. First the procedure to generate a basis of reduced dimensionality for a specified system size is discussed in detail. In this procedure the size of the system is slowly increased while the size of the basis is kept at a constant value. Then a way to improve the overlap of the basis states and the low lying unprojected states is presented. The combination of these two procedures allows for the initial state preparation. Different generalizations of the previous methods are discussed in Sec. 3.3, giving good approximations of the time evolution of the initial state.

Most simulations of current measurements only deal with two time-independent Hamiltonians to describe their systems at different times. This corresponds to situations where the system experiences one quench but no other change over time. Section 3.3 covers methods dealing with that situation. For some applications, it might be essential to use a Hamiltonian with a time-dependency beyond the initial quench. Cases that come to mind are e.g. systems reacting to time-dependent voltages or magnetic fields but also systems subject to time-dependent strain. One main part of this work is focused on a method tailored to these problems. At the beginning of Sec. 3.3 one way to account for this with limited applicability is described. A new implementation that overcomes the limitations of the previous method is described in chapter 5.

3.1 Exact diagonalisation of quadratic many body Hamiltonians

In general, the Hilbert space for a system consisting of M sites with f degrees of freedom (DOF) per site has a dimension of $d = f^M$, scaling exponentially with system size. The number of DOF f and thus d strongly depend on the type of particles which are considered. For fermions the most common cases are spin 1/2 particles, e.g. electrons, and spinless fermions. In case of spinless fermions each site can be either occupied or empty and thus contributes

$f = 2$ degrees of freedom. For spin $1/2$ particles each site is either full,
empty or contain either a spin up or a spin down particle, contributing $f = 4$
degrees of freedom. In both cases the Hilbert space becomes huge already
for moderate system sizes. Calculations for interacting systems using modern
computational techniques without approximations break down at a system
size of a little bit more than forty sites [61]. When dealing with noninteracting
problems the relevant subspace one needs to look at scales only linearly with
system size, $d \propto M$. This allows to simulate noninteracting systems up
to much larger system sizes. In this section it is shown how currents are
calculated for noninteracting problems with spinless fermions and how the
required space collapses to the small subspace.

In order to calculate currents one has to evaluate expectation values of
the form

$$\left\langle \hat{c}_x^\dagger \hat{c}_y \right\rangle, \tag{3.1}$$

where $\hat{c}_x^\dagger$ and $\hat{c}_y$ are creation and annihilation operators of the considered
particles at positions x and y. For example, the current between two sites x
and x+1 in a noninteracting region[1] is given by

$$I_{x,x+1} = -2J_c \frac{e}{\hbar} \mathrm{Im}\left\{ \left\langle \hat{c}_{x+1}^\dagger \hat{c}_x \right\rangle \right\}, \tag{3.2}$$

where J_c is the coefficient of the hopping between the two sites. For time-
independent Hamiltonians expectation values of the form

$$
\begin{aligned}
\left\langle \hat{c}_x^\dagger \hat{c}_y \right\rangle &= \frac{n}{D} \equiv \frac{\langle \Psi(t)| \hat{c}_x^\dagger \hat{c}_y |\Psi(t)\rangle}{\langle \Psi(t) | \Psi(t)\rangle} \\
&= \frac{\langle \Psi(0)| \exp\left\{ \frac{i}{\hbar}\hat{\mathcal{H}}_{\mathrm t}^\dagger t \right\} \hat{c}_x^\dagger \hat{c}_y \exp\left\{ -\frac{i}{\hbar}\hat{\mathcal{H}}_{\mathrm t} t \right\} |\Psi(0)\rangle}{\langle \Psi(0)| \exp\left\{ \frac{i}{\hbar}\hat{\mathcal{H}}_{\mathrm t}^\dagger t \right\} \exp\left\{ -\frac{i}{\hbar}\hat{\mathcal{H}}_{\mathrm t} t \right\} |\Psi(0)\rangle},
\end{aligned}
\tag{3.3}
$$

have to be evaluated, where $\hat{\mathcal{H}}_{\mathrm t}$ is the time evolution Hamiltonian of the
system after quenching, assumed to be time-independent. A generalization
to time-dependent Hamiltonians will be given at the end of the section. For
hermitian Hamiltonians the denominator D becomes one due to probability
conservation. For application attempts to nonhermitian Hamiltonians, see
Sec. 6.4, $D \neq 1$ and as a consequence the norm of the wavefunctions has to
be considered. Let us turn our attention to the expression in the numerator
n. The first step is to commute the time evolution with the creation and

---

[1]All models considered within this thesis contain noninteracting leads. Therefore the
current is of this form in all cases of interest.

annihilation operators. The creation and annihilation operators are rotated into the eigenbasis of the time evolution Hamiltonian $\hat{\mathcal{H}}_t$ of the system at $t > 0$, which in its eigenbasis reads

$$\hat{\mathcal{H}}_t = \sum_{c=0}^{M-1} \epsilon_c^t \hat{c}_c^{t\dagger} \hat{c}_c^t \tag{3.4}$$

with eigenenergies ϵ_c^t. The transformation is defined via

$$\hat{c}_y = \sum_{b=0}^{M-1} U_{yb}^t \hat{c}_b^t, \tag{3.5}$$

with U^t transforming between position space and energy space for $t > 0$. In practice, U^t and ϵ_c^t are obtained using *LAPACK* [62] routines. The commutation is performed using

$$\exp\left\{-i\hat{\mathcal{H}}_t t\right\} = \prod_{c=0}^{N-1} \left(1 - \hat{n}_c^t \left(\exp\left\{-i\epsilon_c^t t\right\} - 1\right)\right), \tag{3.6}$$

with operators $\hat{n}_c^t$ of the occupation number of the eigenenergies for $t > 0$ and

$$\begin{aligned} \hat{n}_a^t \hat{c}_a^{t\dagger} &= \hat{c}_a^{t\dagger}, \\ \hat{n}_b^t \hat{c}_b^t \left|\Psi\left(0\right)\right\rangle &= 0, \\ \hat{c}_a^{t\dagger} \hat{n}_a^t \left|\Psi\left(0\right)\right\rangle &= 0, \\ \hat{c}_b^t \hat{n}_b^t &= \hat{c}_b^t. \end{aligned} \tag{3.7}$$

This yields

$$n = \sum_{a,b=0}^{M-1} U_{yb}^t \exp\left\{-i\epsilon_b^t t\right\} \left\langle\Psi\left(0\right)\right| \hat{c}_a^{t\dagger} f\left(\left\{\hat{n}^t\right\}\right) \hat{c}_b^t \left|\Psi\left(0\right)\right\rangle \times$$
$$\exp\left\{i\epsilon_a^{t*}t\right\} U_{ax}^{t\ -1}, \tag{3.8}$$

with

$$f\left(\left\{\hat{n}^t\right\}\right) = \prod_{c\neq a,b} \left(\left(1 + \hat{n}_c^t \left(\exp\left\{i\epsilon_c^{t*}t\right\} - 1\right)\right)\right.$$
$$\left.\left(1 + \hat{n}_c^t \left(\exp\left\{-i\epsilon_c^t t\right\} - 1\right)\right)\right). \tag{3.9}$$

In case of hermitian Hamiltonians and therefore real eigenvalues the equation $f\left(\left\{\hat{n}^t\right\}\right) = 1$ holds. In chapter 5 quadratic nonhermitian Hamiltonians for

non-interacting problems will be encountered. There holds $f(\{\hat{n}^t\}) \neq 1$ and this method cannot be applied. The operators $\hat{c}_a^{t\dagger}$ and $\hat{c}_b$ are rotated back to the site representation and from there to the eigenbasis of the Hamiltonian

$$\hat{\mathcal{H}}_s = \sum_{c=0}^{M-1} \epsilon_\gamma^s \hat{c}_\gamma^{s\dagger} \hat{c}_\gamma^s \tag{3.10}$$

before the quench via the transformation matrix U^s. This gives

$$n = \sum_{w,z=-\frac{M}{2}}^{\frac{M}{2}-1} \mathcal{U}_{y,w}(t) \Phi_{w,z}^n \mathcal{U}_{z,x}^\dagger(t) \tag{3.11}$$

with

$$\mathcal{U}_{y,w}(t) \equiv \sum_{b=0}^{M-1} U_{yb}^t \exp\{-i\epsilon_b^t t\} U_{bw}^{t\,-1},$$

$$\Phi_{w,z}^n \equiv \sum_{\alpha,\beta=0}^{M-1} U_{w\beta}^s \langle \Psi(0)| \hat{c}_\alpha^{s\dagger} \hat{c}_\beta^s |\Psi(0)\rangle U_{\alpha z}^{s\,-1}. \tag{3.12}$$

Since this work is about physics at zero temperature, the initial state is the ground state of $\hat{\mathcal{H}}_s$. Therefore exactly the N_{el} lowest eigen levels of H^s are occupied with N_{el} being the particle number,

$$\hat{c}_\beta^s |\Psi(0)\rangle = \Theta(N_{el} - \beta - \epsilon)|\Psi_\beta\rangle,$$
$$\langle \Psi(0)| \hat{c}_\alpha^{s\dagger} = \langle \Psi_\alpha| \Theta(N_{el} - \alpha - \epsilon). \tag{3.13}$$

$|\Psi_\beta\rangle$ denotes the Fock state that is the ground state with an empty position at energy ϵ_β^s and ϵ is a small number introduced to get the right occupation. Orthonormality of the Fock states,

$$\langle \Psi_\alpha|\Psi_\beta\rangle = \delta_{\alpha,\beta}, \tag{3.14}$$

leads to

$$\Phi_{w,z}^n = \sum_{\alpha=0}^{N_{el}-1} U_{w\alpha}^s U_{\alpha z}^{s\,-1}. \tag{3.15}$$

As a result only the eigenenergies of the Hamiltonians $\hat{\mathcal{H}}_s$ and $\hat{\mathcal{H}}_t$ and the transformation matrices of single particle creation and annihilation operators between these basis sets are needed in order to calculate the desired quantities. These transformation matrices operate on M states and are therefore

M by M matrices, which gives a huge advantage over calculations using representations on the 2^M-state Fock basis.

This formula enables an easy way of calculating expectation values at intermediate timesteps $t_n = n\Delta t$ and incorporating time-dependent Hamiltonians. The exponential function of the Hamiltonian is approximated by the first order Magnus expansion, discussed in chapter 5,

$$\exp\left\{-\frac{i}{\hbar}\hat{\mathcal{H}}_\mathrm{t}(t)\,t\right\} \approx \prod_{n=1}^{n_{max}} \exp\left\{-\frac{i}{\hbar}\int_{t_{n-1}}^{t_n}\hat{\mathcal{H}}_\mathrm{t}(t')\,\mathrm{d}t'\right\}$$

$$\approx \prod_n \exp\left\{-\frac{i}{\hbar}\hat{\mathcal{H}}_\mathrm{t}(t_n)\,\Delta t\right\}. \tag{3.16}$$

where the decomposition is exact for Hamiltonians $\hat{\mathcal{H}}_\mathrm{t}$ constant in time. The last step holds approximately for slowly varying Hamiltonians. It omits terms of the form

$$\exp\left\{-\left(\frac{\Delta t}{\hbar}\right)^2\left[\hat{\mathcal{H}}_\mathrm{t}(t_j),\hat{\mathcal{H}}_\mathrm{t}(t_k)\right]_-\right\}, \tag{3.17}$$

corresponding to an approximation of order

$$\mathcal{O}\left(\exp\left\{-\left(\frac{J\Delta t}{\hbar}\right)^2\right\}\right). \tag{3.18}$$

This is a good approximation for $J\Delta t \ll \hbar$, where J is the energy scale at which the Hamiltonian varies over time, or if the commutator of the Hamiltonian at different times is small. It leads to an expansion of the time evolution

$$\mathcal{U}(t) = \prod_n \mathcal{U}(n,\Delta t),$$

$$\mathcal{U}_{y,w}(n,\Delta t) \equiv \sum_{b=0}^{M-1} U_{yb}^{t,n}\exp\left\{-i\epsilon_b^{t,n}\Delta t\right\}U_{bw}^{t,n-1}. \tag{3.19}$$

In this notation $U_{yb}^{t,n}$ diagonalizes $\hat{\mathcal{H}}_\mathrm{t}(t_n)$. The numerator then reads in matrix notation

$$n(t) = \left(\hat{T}\prod_n \mathcal{U}(n,\Delta t)\right)\Phi^n\left(\hat{T}^\dagger\prod_n \mathcal{U}^\dagger(n,\Delta t)\right) \tag{3.20}$$

$$= \mathcal{U}(n_{max},\Delta t)\,n(t-\Delta t)\,\mathcal{U}^\dagger(n_{max},\Delta t), \tag{3.21}$$

with time ordering $\hat{T}$ putting earliest times to the right and conjugated time ordering putting them to the left. The result is obtained from steps analogous to the previous calculations, with basis transformations in between each

time evolution step to commute the single steps with $\hat{c}_x^\dagger$ and $\hat{c}_y$. In practice, expectation values are calculated for the first timestep. Then the time evolution $\mathcal{U}(n, \Delta t)$ is applied to the result to get the result for the next timestep and so on.

3.2 The time-independent DMRG procedure

In case of systems including interaction, the Hilbert space does not split into a small relevant space and a rest space. Thus, states and operators have to be represented in the full Hilbert space and are too large to be stored even on a modern computer. Therefore approximations have to be used. There exists a variety of solutions to this problem. The one primarily used in the context of this work is the Density Matrix Renormalization Group technique [24, 63, 26, 64, 65] (in short: DMRG), which is the most common numerical method for one dimensional systems. It was proposed by Steven White in 1992 [24] as a generalization of the numerical renormalization group procedure invented by Kenneth Wilson [23]. In short, it tries to construct a reduced Hilbert space consisting of the states with the highest weight in the density matrix, following the idea that these states contribute most to the physical attributes of the system. It keeps N_{Cut}^2 states, N_{Cut} being the number of states kept per system half. It owes its name to the similarities to other renormalization group techniques, where one adjusts some system parameters while stepwise changing another parameter. In the most basic DMRG the system size is changed leading to a change of the basis states. However this correspondence is not exact because in DMRG steps information is lost, so there exists no inverse operation. This is a necessary ingredient for operations to form a group.

There are several algorithms with different tasks running under the DMRG tag. One combines them depending on the goals one wants to achieve. Out of those the infinite lattice DMRG (iDMRG) and time-independent finite lattice DMRG (DMRG) will be described on the next few pages. These algorithms are used to obtain generic ground state properties of the system. For current transport calculations, they are used to generate the initial state of the system before the quench. The initial state is obtained as the ground state of the initial Hamiltonian represented in the new basis. This representation is computed by the DMRG. Section 3.3 covers time-dependent finite lattice DMRG including dynamic (adaptive DMRG) [66, 67, 68, 27] and static Hilbert spaces (fully time-dependent DMRG) [25, 69, 26]. Adaptive DMRG and fully time-dependent DMRG (full td-DMRG) are used to investigate dynamic properties of the system. In the framework of this thesis they are used

to describe the system at different times and allow for current calculations at those times. Afterwards, there will be a few words regarding the applicability of the technique.

3.2.1   iDMRG

The iDMRG algorithm is a tool tailored for the investigation of the properties of a large system at low energies. Its purpose is to represent the low energy eigenstates of a system of gradually increasing size by a fixed number of basis states. This basis of course has to be adjusted each time the system changes. Starting point of the iDMRG procedure is a small system of a handful of sites, which is small enough so that its exact Hilbert space can be stored on a computer. It then iteratively produces bases for systems growing to an arbitrary size, even to infinite size at the prize of infinite iterations, hence the name.

The iterations are summed up briefly as two-stepped procedures: in a first step, the extension of the system, the basis obtained from the previous iteration is extended to include more sites. In the more complicated second step, this basis of increased size is reduced to a basis of the desired size. The basic idea behind this reduction is to build a many-body density matrix out of the low energy states of the system, and then keep the desired number of eigenstates of the density matrix with the highest eigenvalues. The eigenvalues of density matrices are called weights. The principle behind this idea is that chosing the eigenstates of a density matrix with the highest weight gives the best suited basis to approximate the states contributing to the density matrix. Details for this scheme and measures of the good quality of this approximation are given in Sec. 3.3.3.

In order to fully comprehend the second step yet another idea needs to be motivated. As stated before the algorithm starts from a small system and then adapts the basis with increasing system size. However, calculations in closed small systems lead to eigenstates of the small system which are localized in larger systems since the models used contain hard wall boundary conditions. The ground state of the larger system S is a delocalized state, and a combination of localized states is a bad approximation for delocalized states. This can be seen from the number of nodes of the states, which are the points with zero amplitude in the wavefunction. In general, the wavefunctions of the low energy eigenstates will have only few nodes where its value drops to zero. Due to the hard wall boundary conditions applied, two of the nodes will be at the two borders of the system. Combining the ground states of two smaller systems A and B always creates a node at the border of the two systems, as scetched in Fig. 3.1.
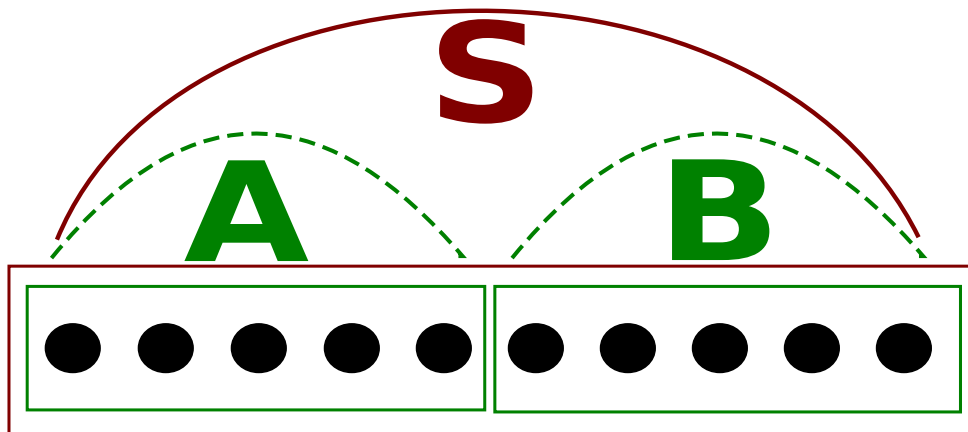
Figure 3.1: Red straight line: The ground state wavefunction of a system S consisting of two blocks A and B. Green, dashed lines: the ground state wavefunctions of the blocks A and B.

In order to overcome this, the small system A is coupled to a bath B. The states are calculated for the combined, closed system S_{red} which for small systems A and B still is smaller than the system S of desired size. Then the bath degrees of freedom are traced out from the density matrix of system S in order to obtain the density matrix for an open system A. From this density matrix, states for an open system are obtained. This way the computed states are not localized in A any more. There is no need for a node at the border of system A and bath B. Combinations of states computed this way approximate the ground state of a larger system S much better. However, there is still a node at the other border of A. In order to create a bath with size equal to the system size at each step in the iteration two systems A and B are grown at the same time. In the calculation of the basis of one of the systems, the other system acts as a bath. This way both system and bath grow at same speed. After the growth of the systems ends, the systems A and B are combined to form the large system S of the desired size. Since the wavefunctions of both systems still have a node at the outer border which does not connect A and B, the growth of the system starts at the borders of the system S. This way the two nodes are at the same position as the nodes of the wavefunctions of S. A more in-depth description of the algorithm is now given by the example of the construction of a one dimensional chain of sites.
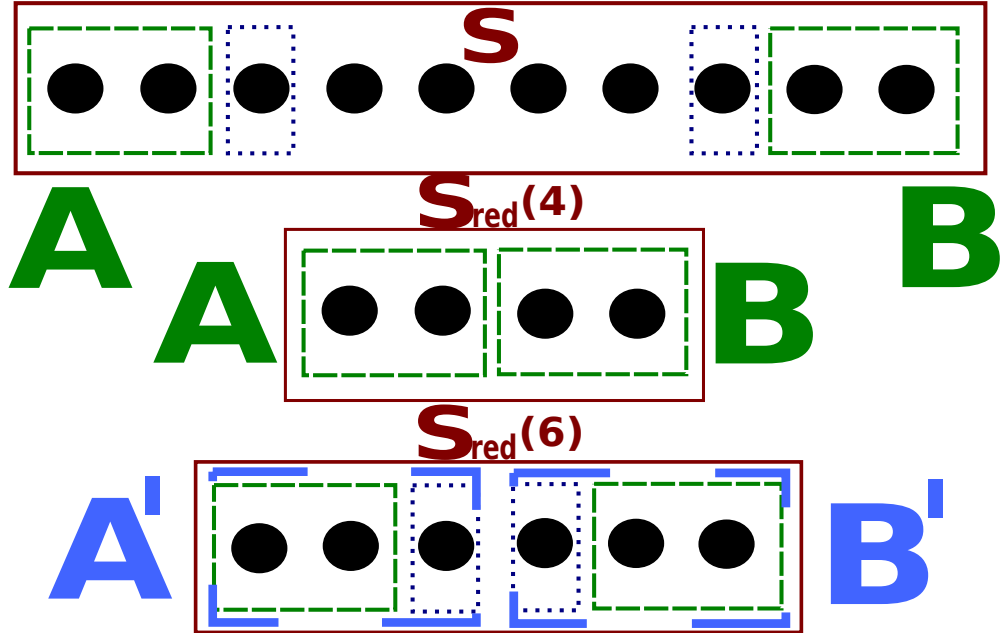
Figure 3.2: iDMRG base construction prescription. Top: Chain S. Middle: Starting system S_{red} of size four, consisting of blocks A and B. Bottom: Increasing size of S_{red} to six by adding one site to each block respectively. The blocks now are A' and B' and contain tree sites instead of two.

Initial step of the algorithm

The iDMRG normally creates systems from the borders towards the middle, the way it is sketched in Fig. 3.2. It choses a few sites beginning from the left end of the chain S as 'block A' and a few sites beginning from the right end as 'block B'. Those blocks are the two halves of the system S_{red} of reduced size. The basis for A and B at this step is chosen as their exactly known Hilbert space. The basis is written in tensor product form. This helps to reduce the size of matrices one has to deal with and speeds up the computation. E.g. the approximated state space Ω_S of system S is decomposed into subspaces ω_x of the blocks A and B representing the states at position x as

$$
\begin{aligned}
\Omega_S &= \omega_A \otimes \omega_B \\
\omega_A &= \omega_1 \otimes \omega_2 \otimes \cdots \otimes \omega_{\frac{M}{2}}, \\
\omega_B &= \omega_{\frac{M}{2}+1} \otimes \omega_{\frac{M}{2}+2} \otimes \cdots \otimes \omega_M,
\end{aligned}
\tag{3.22}
$$

with M being the size of S and $\omega_{A/B}$ the subspace of block A/B. The performance of the algorithm is increased by dissection of Ω_S into a direct sum

of subspaces with different quantum numbers. More information on this is given in appendix B.1.

The important part is not the exact form of the base states but the operators expressed in this basis. Therefore creation and annihilation operators acting on the states included in the blocks are stored. E.g. for Block A consisting of just two sites, with each site being either in an occupied ($|1\rangle$) or unoccupied ($|0\rangle$) state, the creation operator acting on site 1 would read for the basis $\{|1\rangle_1|1\rangle_2, |1\rangle_1|0\rangle_2, |0\rangle_1|1\rangle_2, |0\rangle_1|0\rangle_2\}$

$$\hat{c}_1^\dagger(2) = \begin{pmatrix} 0 & 1 & 0 & 0 \\ 0 & 0 & 0 & 0 \\ 0 & 0 & 0 & 1 \\ 0 & 0 & 0 & 0 \end{pmatrix}. \tag{3.23}$$

Since a tensorial notation is used, it reads in the basis of $\{|1\rangle, |0\rangle\}_1 \otimes \{|1\rangle, |0\rangle\}_2$

$$\hat{c}_1^\dagger(2) = \begin{pmatrix} 0 & 1 \\ 0 & 0 \end{pmatrix}_1 \otimes \begin{pmatrix} 1 & 0 \\ 0 & 1 \end{pmatrix}_2. \tag{3.24}$$

The annihilation operator acting on site two reads

$$\hat{c}_2(2) = \begin{pmatrix} 1 & 0 \\ 0 & 1 \end{pmatrix}_1 \otimes \begin{pmatrix} 0 & 0 \\ 1 & 0 \end{pmatrix}_2. \tag{3.25}$$

The Hamiltonian describing the two blocks as closed systems is constructed out of the annihilation and creation operators. This means that the part of the Hamiltonian of the full system which connects different sites within blocks is constructed out of the operators which are given a representation above. For the given example the Hamiltonian $\hat{\mathcal{H}}(x)$ of an $x = 2$-site block within the leads is

$$\hat{\mathcal{H}}(2) = -J\left(\hat{c}_1^\dagger(2)\,\hat{c}_2(2) + \hat{c}_2^\dagger(2)\,\hat{c}_1(2)\right),$$
$$= -J\left(\begin{pmatrix} 0 & 1 \\ 0 & 0 \end{pmatrix}_1 \otimes \begin{pmatrix} 0 & 0 \\ 1 & 0 \end{pmatrix}_2 + \begin{pmatrix} 0 & 0 \\ 1 & 0 \end{pmatrix}_1 \otimes \begin{pmatrix} 0 & 1 \\ 0 & 0 \end{pmatrix}_2\right). \tag{3.26}$$

Any other operators of interest, like the current operator, can later be composed out of the stored ladder operators.

Increasing the system size of single blocks

Now that the starting point is given the size of S_{red} will be increased by two. This corresponds to the addition of one site to each of the blocks A and B, respectively to form the blocks A' and B'. The increment of size follows the

same algorithm at each point in the procedure. A site is added to each of the blocks respectively towards the middle of the chain. All operators included so far in the calculations concerning block A have to be expressed in a representation defined on the larger Hilbert space of block A'. The subspaces of A' are written as tensor products of subspaces of A and subspaces of the added site. If an operator is presented by the matrix $\hat{O}_A$ in block A, then its representation in block A' is given by

$$\hat{O}_{A'} = \hat{O}_A \otimes \begin{pmatrix} 1 & 0 \\ 0 & 1 \end{pmatrix}_x, \tag{3.27}$$

where x is the position of the added site. Next, the ladder operators acting on the freshly added site are expressed in the expanded basis. They only have nontrivial representations in the one-site subspaces and are represented by tensor products of unity matrices in the subspaces of blocks A or B. E.g. if block A contains m sites, then the creation operator of the newly added site at position $m + 1$ is given by

$$\hat{c}^{\dagger}_{m+1}(m+1) = \begin{pmatrix} 1 & 0 \\ 0 & 1 \end{pmatrix}_1 \otimes \cdots \otimes \begin{pmatrix} 1 & 0 \\ 0 & 1 \end{pmatrix}_m \otimes \begin{pmatrix} 0 & 1 \\ 0 & 0 \end{pmatrix}_{m+1}. \tag{3.28}$$

So far only the Hamiltonian describing the old block was extended to a representation in the new block. The Hamiltonian acting on all sites included in the new block is needed. The Hamiltonian governing the expanded system is written down as combination of terms: on the one hand the Hamiltonian of block A with its operators expressed in the Hilbert space of A' contributes. On the other hand new terms which connect the added site with block A are included. E.g. assume that the newly added site located at position $m + 1$ lies within leads which only contain a constant nearest neighbor hopping with amplitude $-J$. If $\hat{\mathcal{H}}_A(m + 1)$ is the Hamiltonian of block A expressed through $\hat{c}^{\dagger}_x(m + 1)$ and $\hat{c}_x(m + 1)$, then

$$\hat{\mathcal{H}}_{A'}(m+1) = \hat{\mathcal{H}}_A(m+1) - J\left(\hat{c}^{\dagger}_m(m+1)\,\hat{c}_{m+1}(m+1) + \text{h.c.}\right). \tag{3.29}$$

Reduction of basis space

Now that the size of the blocks is increased, the bigger sized $S_{\text{red}}(n + 2)$ is obtained by connecting the two blocks. The operators are extended to a representation in $S_{\text{red}}(n + 2)$ by forming a tensor product between the subspaces of the two blocks. The operators are represented by unity matrices in the respective other block. Then the two Hamiltonians of A and B as well as a hopping term between the two parts are summed up to form the

new Hamiltonian of $S_{\mathrm{red}}(n+2)$. If the number of basis states is still smaller than the treshold, the procedure of increasing the system size is repeated. Else this number is reduced as follows. Since the goal is to approximate the halves of the lowest lying energy eigenstates in their respective block, these eigenstates are calculated for $S_{\mathrm{red}}(n+2)$. The composite Hamiltonian of $S_{\mathrm{red}}(n+2)$ is diagonalized using a modified Jacobi-Davidson algorithm described in appendix A.2 and making use of the representation of the matrix through tensor products. From this the p lowest energy eigenstates are obtained, where p is chosen freely depending on how excited the state of the system is supposed to be. A density matrix $\hat{\rho}_S$ of the sum of those states is formed,

$$
\begin{aligned}
\hat{\rho}_{\mathrm{S}} =& \frac{1}{p} \sum_m |\Psi_m\rangle \langle \Psi_m| , \\
=& \frac{1}{p} \sum_{i,j,k,l,m} \left(\langle i,k|\Psi_m\rangle \langle \Psi_m|j,l\rangle \right) |i,k\rangle \langle j,l| .
\end{aligned}
\tag{3.30}
$$

Here, i,j are indices of the states of one block, k,l are state indices of the second block and m runs over the different states defined in system $S_{\mathrm{red}}(n+2)$ which were added to the density matrix. In the second line of Eq. (3.30) the density matrix is represented in the bases of blocks A and B. The aim is to obtain states which are only defined in block A or B. One reduced density matrix is built for each block by tracing out the degrees of freedom belonging to the other block, respectively. This corresponds to writing the elements

$$
\rho_{i,j} = \frac{1}{p} \sum_k \sum_m \left(\langle i,k|\Psi_m\rangle \right) \left(\langle \Psi_m|j,k\rangle \right)
\tag{3.31}
$$

into the reduced density matrix

$$
\hat{\rho}_{\mathrm{A/B}} = \sum_{i,j} \rho_{i,j} |i\rangle \langle j| .
\tag{3.32}
$$

In this notation, i,j are indices of the states of the kept block and k is the index of states of the traced out block. The N_{Cut} highest eigenstates of the reduced density matrices, obtained by diagonalization using *LAPACK* routines [62], form the new bases in the two blocks with increased size, respectively. The obtained N_{Cut} eigenstates are written into the columns of a projection matrix. The previously stored operators then are projected onto the new bases. This is done separately for all subspaces of interest.

The density matrix of $S_{\mathrm{red}}(n+2)$ can also be formed for a state which is the sum of the lowest energy eigenstates, just as before, plus the sum of

states obtained by applying an operator of interest to those lowest energy eigenstates. If the operator of interest is denoted by $\hat{O}$ and $\hat{O}|\Psi_m\rangle = |\Phi_m\rangle$, then the resulting density matrix entries read

$$\rho_{i,j} = \frac{1}{2p} \sum_k \sum_m \left(\langle i,k|\Psi_m\rangle \langle \Psi_m|j,k\rangle + \langle i,k|\Phi_m\rangle \langle \Phi_m|j,k\rangle \right). \qquad (3.33)$$

This way the expectation values of $\hat{O}$ are approximated with a lower error in this step since their weight is considered in the density matrix explicitly. However, the energy eigenstates are approximated with a higher margin of error in this case. This fact can overshadow the advantage of a better initial approximation, since the low energy eigenstates and eigenenergies are important for the time evolution of the state of the system. Therefore it must be weighted whether to include the additional states.

As a result, one site was added to each block while keeping the number of basis states low and computable. This procedure of increasing the system size and then approximating the bases of the blocks is repeated until the desired system size is reached. If interested in ground state properties only, iDMRG can be used to obtain them. Then the repetition continues until the expectation value for the ground state properties of interest converges.

3.2.2 DMRG

The iDMRG gives a reasonable but crude idea of the real lowest lying states of the system. The algorithm discussed now takes the basis produced by iDMRG as its starting point. Then it iteratively improves that basis with respect to the approximation of the low energy eigenstates. The adjustment of the basis is done under the restriction of a constant number of basis states, just as before. The additional constraint for the DMRG is that the size of the system S now stays fixed. The algorithm is built upon two main ideas.

The first idea is a reformation process of the blocks of the system. This process is split into single steps which update only one site of the block per step, and which are similar to the initial construction steps done during iDMRG. This time however the overall system size is kept fixed while varying the size of the two blocks. Since the system size heavily influences the properties of the system's states this yields a more accurate description of the system. In order to use DMRG the blocks of differing sizes computed during the runtime of the iDMRG have to be stored and kept.

The second idea is to iteratively improve the basis. Better initial guesses of the optimal basis lead to better bases resulting from the reformation process. Therefore, after rebuilding the system once and having more accurate
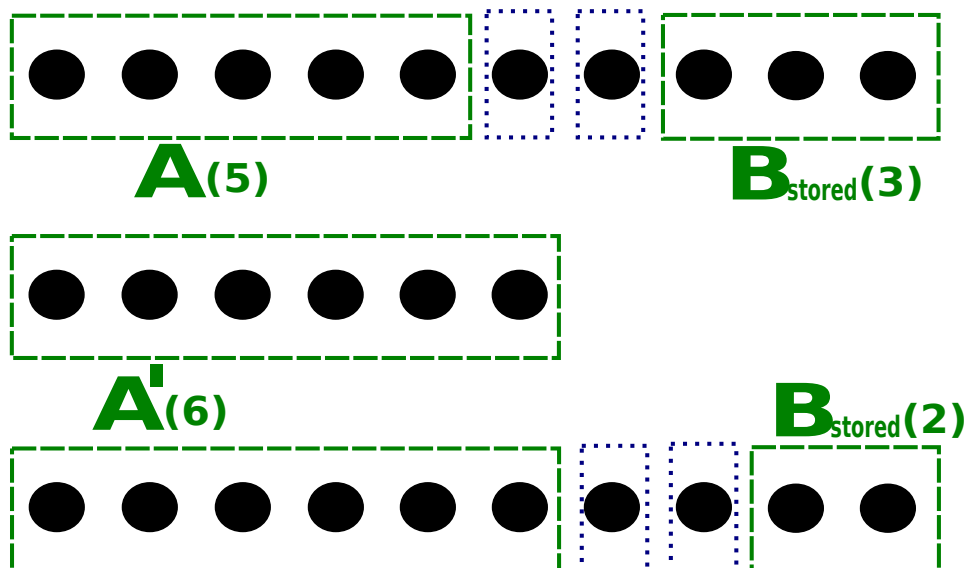
Figure 3.3: First and second step of a sweep. Starting point is the situation after the iDMRG runs which are shown in Fig. 3.2. From iDMRG a system S consiting of ten sites is constructed. This system is composed of the two blocks A and B, each containing five sites. The upper and middle figures show the first step of a sweep. At the start of the first step, shown in the upper figure, a system is constructed containing block A, two additional sites and a block B for the remaining system. The required block B has already been calculated in the third last iDMRG step, which lead to an expanded block size of three sites. Overall, the system still contains 10 sites. The size of block A is increased by one and A' is generated and stored. A' is shown in the middle figure. The lower figure pictures the beginning of the second step. Now the system S contains the updated block A', two additional sites with the exactly known basis and a smaller block B with only two sites, which was stored in the iDMRG step before the block B with 3 sites was generated and stored. From this point the growth of block A continues and the sequence is repeated up to the smallest stored version of block B with an exact basis.

blocks than in the first rebuild, it is rebuilt again. This leads to more accurate blocks, which can be used to make even more appropriate blocks by rebuilding the system again, and so on. This idea is similar to other iterative schemes known in physics such as the iterative solution of the Dyson series discussed e.g. in Ref. [70]. Each rebuild of the system is called a sweep.

The algorithm starts with a step similar to the iDMRG iteration. However, block A is taken at its full size obtained from the last iDMRG step that was performed before. Operators defined on block A in that iDMRG step are also kept. Block B and corresponding operators are obtained from earlier iDMRG steps. This earlier step is chosen such that block B is 2 sites smaller than block A, so after adding 2 sites the original size of S is restored, see Fig. 3.3. Only the properties of operators acting on block A of increased size are of interest since those of block B with decreasing size are already known. Hence the reduction of basis size is only applied for block A, e.g. only the reduced density matrix with block B traced out is created.

A more detailed explanation of such a single step can be found in appendix B.2, where the step is revisited in a different context. Since S is at the final size and all positions of the full Hamiltonian are included, all operators can be included in each step. This is repeated with blocks A of increasing and blocks B of decreasing size until the exactly known basis for block B is used, see Fig. 3.4.
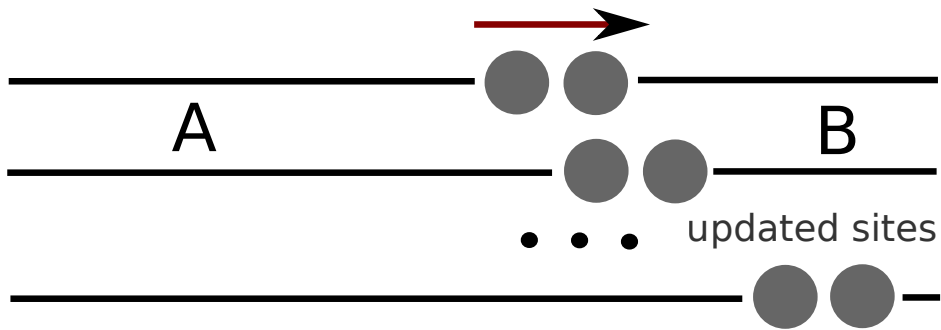

Figure 3.4: Sketch of a sweep to the right. In this sketch, A and B denote the two blocks and ●● are the two respective sites which are added in the beginning of each step, and whose representation is updated during the step.

Starting from the exactly known basis of block B, similar steps are taken with increasing size of block B and decreasing size of block A, see Fig. 3.5.
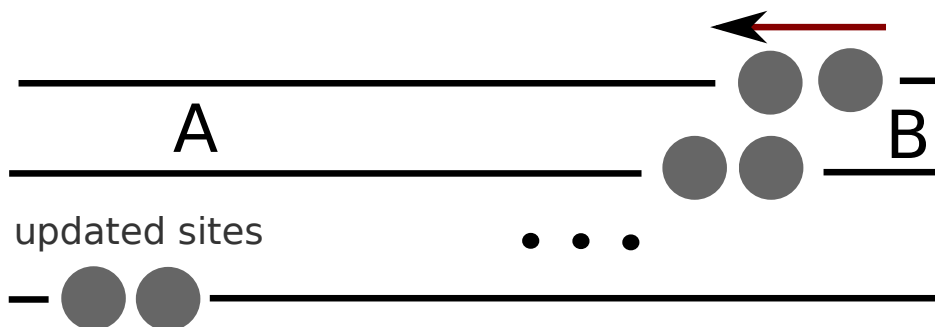
Figure 3.5: Sketch of a sweep to the left.

Now the already existing blocks B of various sizes are replaced by their newly calculated and improved counterparts. Once the smallest block A is reached, the direction is changed again and the blocks A are improved. After reaching the middle of the system again, each block of each size has been calculated once with a constant system size, and one sweep is finished. This can then be continued to improve the results. Afterwards the resulting operators can be used to calculate the ground state properties of interest, or the initial state as ground state of the initial Hamiltonian.

3.3   Time evolution using DMRG

After the DMRG methods to obtain ground state properties have been discussed in the previous sections, this section deals with DMRG procedures for the treatment of the dynamics of the system. The first such procedure was proposed for low energy excitations in Ref. [25]. Cazalilla and Marston used the algorithm of Sec. 3.2.2 to create a low energy basis. They used this basis to express the initial state and to evolve it in time, arguing that for short times the system could still be adequately described by the low energy states of the initial Hamiltonian. However in Ref. [69] Luo et al. show cases where the basis approximating the low energy states of the initial Hamiltonian is not suitable to describe the time evolved states. In this section two solutions to the problem of adequate bases for time evolved states are presented, the adaptive DMRG and fully time-dependent DMRG (full td-DMRG). The topic of DMRG is concluded by remarks on the good quality of the DMRG approximation and the applicability of the DMRG algorithms presented in Secs. 3.2.1, 3.2.2 and 3.3.

3.3.1 Adaptive DMRG

Adaptive DMRG carries out the time evolution step by step. In each timestep the basis approximating the time evolved state is adapted to the change due to time evolution, hence the name. The algorithm again consists of sweeps through the system and starts after a normal DMRG sweep. Its exact form depends on the implementation of time evolution. The two proposed implementations discussed in this section are based on the Suzuki-Trotter [71, 72, 73] and Runge-Kutta [74, 75, 76] approximations, which are given in appendices A.3.1 and A.3.2, respectively.

Suzuki-Trotter based time evolution

The procedure for the Suzuki-Trotter time evolution [66, 67] will be discussed first. After evaluating the ground state properties of interest, e.g. the initial state calculation, block A of half the system size and block B with two sites less are loaded, see the upper subfigure of Fig. 3.3. Then the standard DMRG procedure described in Ref. 3.2.2 is carried out until just before the calculation of energy eigenvalues of S_{red}. In time-independent DMRG, the Jacobi-Davidson algorithm to diagonalize the Hamiltonian of S_{red} would be carried out now. In adaptive DMRG the wavefunction of the initial state is evolved in time instead using the Suzuki-Trotter algorithm for half a time step, and the diagonalization is skipped. The wavefunction is obtained by the basis transformations discussed in appendix B.2. The first order Suzuki-Trotter algorithm approximates a time evolution operator of the form $\exp\left\{(h_{1,...,M/2+1} + h_{M/2+1,...,M})\Delta t\right\}$, where $h_{x,...,y}$ acts on sites x till y, by

$$\exp\left\{h_{1,...,M/2+1}\Delta t\right\}\exp\left\{h_{M/2+1,...,M}\Delta t\right\} + \mathcal{O}(\Delta t^2). \qquad (3.34)$$

In a second step, the second order algorithm approximates

$$\begin{aligned}
\exp\left\{(A_{M/2+1,M/2+2} + ... + B_{M-1,M})\Delta t\right\} = \exp\left\{A_{M/2+1,M/2+2}\frac{\Delta t}{2}\right\} \times ... \\
... \times \exp\left\{B_{M-1,M}\Delta t\right\} \times ... \\
... \times \exp\left\{A_{M/2+1,M/2+2}\frac{\Delta t}{2}\right\} \\
+ \mathcal{O}(\Delta t^3), \qquad (3.35)
\end{aligned}$$

where $A_{x,x+1}$ acts on the sites x and x+1 and M is the system size. In the scope of this thesis, $A_{x,x+1}$ consists of the prefactor $-i/\hbar$ and those terms of the Hamiltonian that act only on the two sites x and $x+1$, e.g. the hopping

between these two sites. The time evolution is executed only locally on the
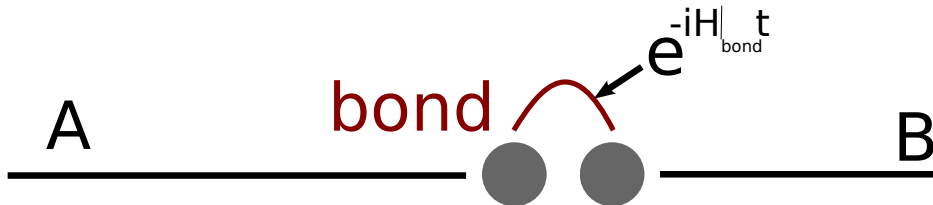bond between the two newly added sites, see Fig. 3.6.

Figure 3.6: Sketch showing the time evolution operator that acts locally on
the two added sites.

E.g. in the first step, where sites $M/2+1$ and $M/2+2$ are added, only the
part $\exp\{A_{M/2+1,M/2+2}\Delta t/2\}$ is applied. This means that only those terms in
the Suzuki-Trotter approximated time evolution operator are applied to the
wavefunction that consist only of creation and annihilation operators acting
on the two added sites. The representation of the Hilbert space of the two
added sites, in the given example the sites $M/2+1$ and $M/2+2$, is still exact
at this point during the algorithm. Therefore no approximation error occurs
due to the time evolution of some approximated states. The only approxima-
tion error in this step is the one resulting from the decomposition of the time
evolution operator, which is the Suzuki-Trotter error. The course of action
described here corresponds to application of a second order Suzuki-Trotter
decomposition of the time evolution operator. A generalization to other or-
ders is straightforward and reduces the mentioned error. In the next step
where sites $M/2+2$ and $M/2+3$ are added, only $\exp\{A_{M/2+1,M/2+2}\Delta t/2\}$
is applied. After one sweep has been concluded, a whole time evolution op-
erator will have been applied to the initial wavefunctions and further time
evolution can be performed by more sweeps. This method is very powerful
for Hamiltonians including only on-site and nearest neighbor interactions and
hoppings where the effort computation time scales linearly in time and the
needed resources do not scale in time, but not applicable otherwise.

Runge-Kutta based time evolution

Time evolution schemes using Runge-Kutta are an example of methods suit-
able for a more general set of systems. One such scheme is implemented in
Ref. [68]. This implementation is discussed in the next few paragraphs. Here,
the time evolution operator in its Runge-Kutta approximation is applied af-
ter each half sweep, which means whenever the two sites are being added in
the center of the system. Again the time evolution replaces the diagonal-

ization of the Hamiltonian and the search for the lowest energy eigenstates which would be performed in time-independent DMRG. The time evolution of the wavefunctions is not only carried out to the next timestep to obtain $|\Psi(t+\Delta t)\rangle$ from $|\Psi(t)\rangle$, but also for $|\Psi(t+\Delta t/3)\rangle$ and $|\Psi(t+2/3\Delta t)\rangle$, where a generalization to a different number of intermediate timesteps is possible. The obtained wavefunctions are still a rough approximation for time evolved wavefunctions themselves. However, they provide additional directions in the basis in which the time evolution can then be carried out in better approximation. The obtained states all are added to the density matrix, which then is traced out as normal. This way the resulting basis states are also optimized to approximate the time evolved low energy states well up in the interval between t and $t + \Delta t$. Time evolution of the states of interest is carried out in this basis. Expectation values at $t + \Delta t$ are evaluated, then the next half of a sweep is executed, again with time evolution of the states in its last step.

The strength of adaptive td-DMRG methods is their ability to simulate systems up to arbitrary large times with a fixed number of states which are dynamically adapted during time evolution. However the methods share the weakness that any approximation error made to the states grows during time evolution since the erroneous states are used to find an optimal basis at the next time step. The next section presents a method which does not suffer this runaway error since it uses a static Hilbert space. This comes at the cost of a time-dependence of the size of this static Hilbert space if the approximation error is to be kept constant.

3.3.2 Full td-DMRG

Instead of adapting the basis to the time evolution of the initial state one can also use a static basis which already is optimized to approximate the low lying energy eigenstates at each timestep. This has been proposed in Ref. [26] and is called full td-DMRG. Full td-DMRG does not start after the initial DMRG sweeps, but replaces them. At each step in a sweep after performing the Jacobi-Davidson algorithm to find the low energy eigenstates, these states are evolved in time for the desired number of timesteps. This time evolution is carried out using the time evolution Hamiltonian expressed in the current basis and can be done using any time evolution scheme. In the scope of this thesis a method that searches the Krylov space for the closest match to $\exp\{-i(\hat{\mathcal{H}}_t - E_0)\Delta t\}|\Psi\rangle$ is used. The method is described in appendix A.3.3, reviews are also available e.g. in Ref. [77]. All the states obtained from timesteps during time evolution are included in the density

matrix. The reduced density matrix is calculated via

$$\rho_{i,j} = N \sum_k \sum_l \left(\sum_n \langle \Psi_l\left(n\Delta t\right) | j,k \rangle \right) \left(\sum_o \langle i,k | \Psi_l\left(o\Delta t\right) \rangle \right), \qquad (3.36)$$

with N being a normalization factor that is irrelevant for the determination
of the eigenstates. After enough sweeps when the results converged, the
initial state is calculated as ground state of the initial Hamiltonian. This
state is then evolved in time using the time evolution Hamiltonian. At each
step in the time evolution the current expectation values as well as any other
expectation values can be calculated using the respective operators and the
time evolved states. All operators occurring here are expressed in terms of
creation and annihilation operators, which again are represented in the basis
found by the full td-DMRG.

The method actually used in this work is an adaption of full td-DMRG.
After the iDMRG, full td-DMRG is used with a small number of kept states
for a small time interval for the initial sweeps. Expectation values up to the
interval border are calculated. Then, additional sweeps are carried out with
a larger number of states. In those sweeps, states that are evolved further in
time are added to the density matrix, so a larger time range is considered.
This is repeated with a growing number of kept states and time intervals.
Before each change in the time interval, expectation values are calculated for
the present time interval. This reduces overall computation time and gives
preliminary results for the time evolution which are nonetheless at usual
precision for the time interval under consideration.

3.3.3 Assumptions in DMRG and field of usage

In the motivation of the iDMRG procedure two main points were made. The
first statement is that keeping the states with the highest weight in the den-
sity matrix leads to the best approximation of the unprojected wavefunction
and therefore to the best approximation of the expectation value. The second
statement is that by tracing out the environment block parts of wavefunctions
are obtained which can be composed to the low energy eigenstates of larger
systems. In this section measures for the approximations made by the two
points are presented and motivated. The link between these measures and
the success of DMRG in one-dimensional problems is shown. This discussion
can also be found in various reviews on the topic, see e.g. Ref. [63, 64, 65].

Consider a system U divided into two smaller systems S and E with bases
$\{|i\rangle\}$ and $\{|j\rangle\}$, so that it is formed by the tensor product of the two smaller
systems. The dimension of S be N_S, the dimension of E be N_E. A state of

U then is given by

$$|\Psi\rangle = \sum_{i=1}^{N_S}\sum_{j=1}^{N_E}\phi_{ij}\,|i\rangle\,|j\rangle\,. \tag{3.37}$$

A state in S, called $|\tilde{\Psi}\rangle$, is intended to approximate $|\Psi\rangle$. It is given by

$$\left|\tilde{\Psi}\right\rangle = \sum_{i=1}^{N_S}\sum_{j=1}^{N_E}c_i\,|i\rangle\,|j\rangle\,. \tag{3.38}$$

The good quality of the approximation is then determined by the distance between the two states in Hilbert space, defined by the 2-norm

$$\left|\left||\Psi\rangle - \left|\tilde{\Psi}\right\rangle\right|\right|^2 = \left(\langle\Psi| - \left\langle\tilde{\Psi}\right|\right)\left(|\Psi\rangle - \left|\tilde{\Psi}\right\rangle\right)$$
$$= \langle\Psi|\Psi\rangle + \left\langle\tilde{\Psi}|\tilde{\Psi}\right\rangle - 2\mathrm{Re}\left\{\left\langle\tilde{\Psi}|\Psi\right\rangle\right\}$$
$$= 1 + \sum_{i=1}^{N_S}c_i c_i^* - 2\mathrm{Re}\left\{\sum_{i=1}^{N_S}\sum_{j=1}^{N_E}c_i^*\phi_{ij}\right\}$$
$$= 1 + \sum_{i=1}^{N_S}\left(\mathrm{Re}\left\{c_i\right\}^2 + \mathrm{Im}\left\{c_i\right\}^2\right)$$
$$- 2\sum_{i=1}^{N_S}\sum_{j=1}^{N_E}\left(\mathrm{Re}\left\{c_i\right\}\mathrm{Re}\left\{\phi_{ij}\right\} + \mathrm{Im}\left\{c_i\right\}\mathrm{Im}\left\{\phi_{ij}\right\}\right). \tag{3.39}$$

Let the size of S, N_S, be given. Let the separation of U into S and E and thus the exact form of S be adjustable. Different realizations of the separation are determined by the coefficients ϕ_{ij} of $|\Psi\rangle$ in the realized bases. Minimizing the distance with respect to the real and imaginary part, Re{...} and Im{...}, of the coefficients c_k and ϕ_{lm} thus gives the optimal approximation of $|\Psi\rangle$ for given N_S. The choice of ϕ_{lm} determines the basis $\{|i\rangle\}$, the choice of c_k determines the approximating state $|\tilde{\Psi}\rangle$. Minimizing with respect to Im$\{c_k\}$ gives

$$\mathrm{Re}\left\{c_k\right\} - \sum_{j=1}^{N_E}\mathrm{Re}\left\{\phi_{kj}\right\} = 0. \tag{3.40}$$

Using this and the complex conjugated equation gives for the 2-norm

$$\left|\left||\Psi\rangle - \left|\tilde{\Psi}\right\rangle\right|\right|^2 = 1 - \sum_{i=1}^{N_S}\sum_{j,k=1}^{N_E}\phi_{ki}^*\phi_{ij} \tag{3.41}$$

Comparison of the resulting equation to the density matrix in its general
form in the basis $\{|i\rangle |j\rangle\}$ and in its eigenbasis $|\alpha\rangle$,

$$\hat{\rho} = |\Psi\rangle \langle\Psi|$$

$$= \sum_{j,k=1}^{N_E} \sum_{i,l=1}^{N_S} \phi_{kl}^* \phi_{ij} |i\rangle |j\rangle \langle k| \langle l|$$

$$= \sum_{\alpha=1}^{N_E \times N_S} w_\alpha |\alpha\rangle \langle\alpha|, \tag{3.42}$$

shows that Eq. (3.41) corresponds to the basis states $|i\rangle$ being a subset of
the eigenstates $|\alpha\rangle$ of the density matrix with eigenvalues, or weight, w_α. No
limitations to the explicit form of the basis states $|j\rangle$ were made. They are
rotated to the eigenstates of the density matrix. Eq. (3.41) then reads

$$\left|\left||\Psi\rangle - \left|\tilde{\Psi}\right\rangle\right|\right|^2 = 1 - \sum_{i=1}^{N_S \times N_E} w_\alpha \tag{3.43}$$

and can be minimized for a fixed number of states by keeping the states with
the highest weight. This corresponds to S being spanned by the eigenstates
$|\alpha\rangle$ with heighest weight w_α. The approximation error, or the distance of the
two states, then is given by the discarded weight $\epsilon = 1 - \sum_{i=1}^{N_S} w_\alpha$.

Up to a prefactor the same approximation error is obtained for expecta-
tion values. In the normalized eigenbasis of the density matrix, one finds

$$\left\langle\hat{A}\right\rangle = \sum_{\alpha=1}^{N_E \times N_S} w_\alpha \langle\alpha| \hat{A} |\alpha\rangle$$

$$= \sum_{\alpha=1}^{N_S} w_\alpha \langle\alpha| \hat{A} |\alpha\rangle + \sum_{\alpha=1+N_S}^{N_E \times N_S} w_\alpha \langle\alpha| \hat{A} |\alpha\rangle$$

$$\leq (1-\epsilon) \left\langle\hat{A}\right\rangle_{\text{red}} + A_{\max}\epsilon, \tag{3.44}$$

where $A_{\max}$ is the maximum eigenvalue of $\hat{A}$ and $\langle\hat{A}\rangle_{\text{red}}$ is the expectation
value of $\hat{A}$ in the reduced, approximated basis. The DMRG requires ϵ to
be small in order to be appropriate. Thus the difference between expecta-
tion value in the full Hilbert space and in the basis created by DMRG is
proportional to ϵ.

In DMRG, the whole system is separated into a system block and an
environment block to create entangled states. If the system is in a pure state
in one of the blocks, the wavefunction is composed of pure wavefunctions

within the respective blocks and thus has nodes at the edges of the blocks. A measure for the entanglement is the von Neumann entropy

$$S = - \sum_\alpha w_\alpha \log_2 \{w_\alpha\} . \tag{3.45}$$

For pure states the weight is proportional to a kronecker delta and $S = 0$. When truncating states with small weight, also contributions to S are discarded and information on the correlations between the two parts of the system is lost. In that sense the DMRG truncation of states with lowest weight can also be understood as the maximization of kept S for a fixed number of basis states. Therefore the discarded von Neumann entropy also serves as measure for the good quality of the DMRG approximation. High entropy implies strongly entangled states which means that the weights of the different density matrix eigenstates vary slowly. As a result, more states need to be kept for a higher entropy in order to keep the discarded weight small. In this work the number of kept states was varied dynamically at each step of the algorithm to keep the discarded weight and entropy below fixed thresholds, as proposed in Ref. [78].

In Ref. [63] the shape of the weight distribution ist discussed. For gapped one-dimensional systems discussed in the scope of this thesis, the weight falls off exponentially. Therefore only a small number of basis states is needed in one dimension to reduce the discarded weight to a negligible amount. In the DMRG simulations the gap originates in the finite size of the system. Also the dependence of entropy on the system size is discussed. For a gapped one-dimensional system the entropy scales logarithmically with system size up to a maximum depending on the correlation length in the system. This means that in one dimension the DMRG procedure can be performed up to large system sizes without the need of increasing the kept number of states. For those reasons DMRG is a powerful method in one dimension, especially for systems involving only short ranged interactions and couplings.

Chapter 4

Models for molecular diodes

In this chapter the numerical transport calculation methods presented in chapter 3 are used as a tool to study an open question in the field of molecular electronics.

The aim of this field is to realize basic electronic modules that consist of single molecules and therefore allow the composition of electronic devices of atomic scales. The chapter refers to work published in Ref. [2].

The first step in molecular electronics has been the paper of Aviram and Ratner [6] (AR), who gave a first theoretical proposal for a molecule based diode. Up until then, electron transport has been investigated for single electrons within molecules [43, 44, 45, 42]. In those studies two molecular subunits of a certain kind are encountered [46, 47]. The highest occupied molecular orbital (HOMO) of one of the subunits is situated close to the Fermi energy and serves as electron donor, so an electron is easily available for transport. In the other subunit, the lowest unoccupied molecular orbital (LUMO) is close to the Fermi energy and therefore functions as an acceptor to catch the transfered electron. AR have suggested that polarizable molecular units containing this donor and acceptor and connecting them via an electron bridge would show direction dependent current, also called current rectification, when coupled to external leads.

Afterwards experiments have mainly tried to realize the molecular structure proposed by AR, or they have used other strongly polarized molecules. Although rectification has been observed, there is still discussion about mechanisms contributing to or causing the respective rectification [79, 80, 81, 82, 83, 84]. For example, many molecules with a donor-bridge-acceptor structure did not show any rectification [85], casting doubts on the AR proposal. Also [86] for example reviews two more mechanisms besides the AR proposal and its adaptions, and rates their applicability to the molecule under investigation in that paper. Both additional mechanisms assume a polar-

ized molecule but look at different effects of the polarization. In the first mechanism an 'asymmetric field' [86] acts on the molecule. As a result the energy levels of the molecule adjust to the energy band of one of the leads. The other case introduces a fixed asymmetry in the tunneling rate between molecule and leads, leading to an 'asymmetric charging' [86] of the molecule for the two different bias directions. It might help the understanding and improvement of molecular diodes if the mechanisms responsible for the respective rectification could be identified. However, the special case of these two mechanisms illustrates the problems encountered when testing single mechanisms separately in experiment. In order to realize one of the two, a polarization has to be introduced in the molecule which most likely will also add contributions from the other effect [86]. The entanglement of the two effects increases the difficulty of a separation of their contributions to rectification. Also other unwanted effects like the chemical binding of molecules to one of the leads [83, 86] can influence the results of the experiments. In the work presented here [2] these mechanisms are approached from a different perspective. They are investigated by extraction of particular molecular properties given by energy levels, interactions and tunneling rates, which define these mechanisms. The properties then are embedded into simple models, and their abilities to cause current asymmetries within the models are tested. This then hints at the usability of mechanisms built around the embedded properties. Some proposals for molecular diodes are built around mechanisms between the molecule and a specific material coupled to it, e.g. gold [36]. If those molecules are instead coupled to a different kind of lead, the functionality of the diode no longer is guaranteed. In this chapter, the focus lies on universally usable diodes. Therefore, the current asymmetries should be independent of the specific form of the environment of the molecule. After a short description of the applied methods given in Sec. 4.1, the most commonly discussed mechanisms are tested under these considerations in Secs. 4.2 and 4.3. In Sec. 4.4 a different mechanism is proposed and tested, with an application given in Sec. 4.5.

4.1   Methods

In literature [86] the rectification ratio, defined as

$$r = \frac{I\left(V\right)}{-I\left(-V\right)},\tag{4.1}$$

often is used as a measure for the ability to rectify. Since this quantity can diverge for vanishing $I(-V)$, this chapter instead uses the current asymmetry,

defined as

$$A\left(V\right) = \frac{I\left(V\right) + I\left(-V\right)}{I\left(V\right) - I\left(-V\right)}, \tag{4.2}$$

with I being a current. This current is generated and extracted as described in chapter 2. However, for the results obtained the values of the current asymmetry do not need to be calculated since rectification is evident from the plotted data.

The setup corresponding to scattering theory calculations is used to test mechanisms for their ability to rectify currents. More information on the setup, as well as the comparison of simulations using the same assumptions as scattering theory and simulations using shifted energy bands, can be found in Sec. 2.3.2. In the scattering theory calculations, the dispersion relation and the density of states cancel each other. The two terms cancel in the step between Eq. (2.21) and Eq. (2.22). The dispersion relation appears in Eq. (2.21) due to the assumption of plane waves, which is integral to scattering theory. Due to the cancellation the results obtained via scattering theory do not depend on band structure effects like the finite bandwidth, e.g. the current will not vanish for voltages larger than the bandwidth. This leads to the conclusion that rectification achieved in scattering theory does not depend on the specific form of the leads. The corresponding models allow for universally applicable diodes. Currents are also calculated using the second setup corresponding to metallic leads. On the onme hand this is done as a comparison. On the other hand it allows one to discuss the influence of the band structure of the leads on the results.

For noninteracting models the scattering theory calculations are performed analytically, for interacting models the DMRG is used. For the setup leading to shifted bands exact diagonalization is applied in the noninteracting case, and the DMRG is used in the interacting case. The numerical calculations involve systems of finite size M. Since only integer numbers of particles N are possible in those systems and the systems are prepared either at half filling or at quarter filling, it holds either $M = 2N$ or $M = 4N$. The system size is even. In cases of molecules being represented by an odd number of sites, an odd number of sites has to be distributed among the two leads. Thus the sizes of the two leads differs by at least one site. This size difference is used for finite size estimates. Comparing the current for a system where the left lead is the larger one with the current in case of a larger right lead hints at the error induced by leads of finite size.
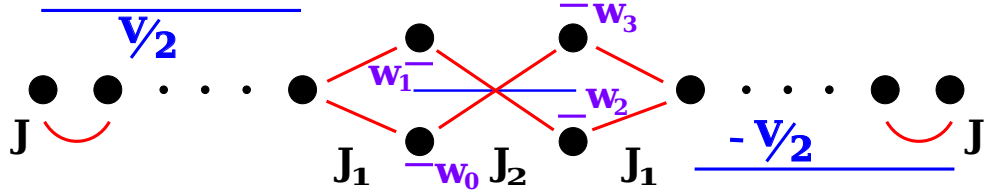
Figure 4.1: Sketch of the system modeled by Eq. (4.3). Red lines connecting dots describe hopping terms, blue, long lines describe the quenched potential, and purple, short lines the energy levels of the two-level systems.

4.2 The Aviram-Ratner proposal

In their paper, AR look at a class of molecules consisting of donor and acceptor subunits. The subunits are coupled by a bridge part and symmetrically connected to the two leads. The donor and acceptor are approximated by two-level systems, keeping only HOMO and LUMO of each subunit. The acceptor upper level has slightly higher energy than the Fermi surface, the donor lower level has an energy closely below the Fermi surface. In the proposal, different kinds of interactions are assumed implicitly. Incomplete screening leads to an electric field. The field causes each of the two two-level systems to adjust their energy to the energy band of one of the leads similar to the 'asymmetric field' case discussed earlier. The chemical potential is supposed to increase or decrease linearly between the leads, so the leads act as parallel-plate capacitors with the molecule in between. Additionally, interactions between system and bath cause the relaxation of electrons after hopping on a two level system. According to AR, a shift in chemical potentials leads to significant current flow from donor to acceptor for a donor HOMO with higher energy relative to the chemical potential than the energy of the acceptor LUMO. Due to the small difference in energy between donor HOMO and acceptor LUMO this situation is already realized for small voltages. Significant current flow in the other direction requires a donor HOMO with higher energy than the Fermi energy in the nearby lead. The difference between donor HOMO and Fermi energy in the nearest lead depends on the chosen parameters. In general it deviates from the energy difference between donor HOMO and acceptor LUMO, hence the rectification.

This situation is modeled without electric field and system bath interactions for several reasons. As stated before, the different mechanisms should be separated in models in order to analyze their individual contributions to rectification. The adjustment of energy levels due to the electric field is essentially the same mechanism as the one containing an 'asymmetric field'

and a molecule represented by one level. As argued e.g. in chapter 5 of
Ref. [51] the 'asymmetric field' depends on form and other qualities of the
leads. There is experimental evidence suggesting that the electric field dif-
fers from the one assumed by AR for some realizations of the two leads [83].
Mechanisms relying on such external factors are not considered in this work.
Interactions between system and bath leading to relaxation effects clearly
also need external factors to work and therefore are disregarded here. As
will be shown in the rest of this section, the remaining model after omission
of the named interactions does not rectify currents in scattering theory. The
proposed mechanism is not sufficient for rectification independent of external
factors.

The investigated model is sketched in Fig. 4.1 and is described by the
Hamiltonian

$$\hat{\mathcal{H}} = - J \sum_{x=-\infty}^{-1} \left(c_x^\dagger c_{x-1} \right) - J \sum_{x=5}^{\infty} \left(c_x^\dagger c_{x-1} \right)$$
$$- J_1 \left(c_0^\dagger c_{-1} + c_1^\dagger c_{-1} + c_4^\dagger c_3 + c_4^\dagger c_2 \right) + \text{h.c.}$$
$$- J_2 \left(c_2^\dagger c_0 + c_3^\dagger c_0 + c_2^\dagger c_1 + c_3^\dagger c_1 \right) + \text{h.c.}$$
$$+ \sum_{i=0}^{3} w_i \hat{n}_i. \tag{4.3}$$

Here, J is the lead hopping, J_1 denotes hopping from leads to the two-level
systems, J_2 hopping between the two-level systems and the w_i are the energies
of the different energy levels. The plane wave ansatz in Eq. (2.17) for the
eigenfunctions has to be modified to

$$c_k^\dagger = \sum_{x=-\infty}^{-1} \left(e^{ikx} + r e^{-ikx} \right) c_x^\dagger$$
$$+ \sum_{x=4}^{\infty} t e^{ikx} c_x^\dagger$$
$$+ \sum_{i=0}^{3} a_i \, c_i^\dagger, \tag{4.4}$$

with r being the reflection and t the transmission amplitude, and a_i are the
amplitudes on the two-level systems. The transmission amplitude is obtained
from the requirement of the ansatz being an eigenstate with eigenenergy E_k:

$$\left[\hat{\mathcal{H}}, c_k^\dagger \right] = E_k c_k^\dagger. \tag{4.5}$$
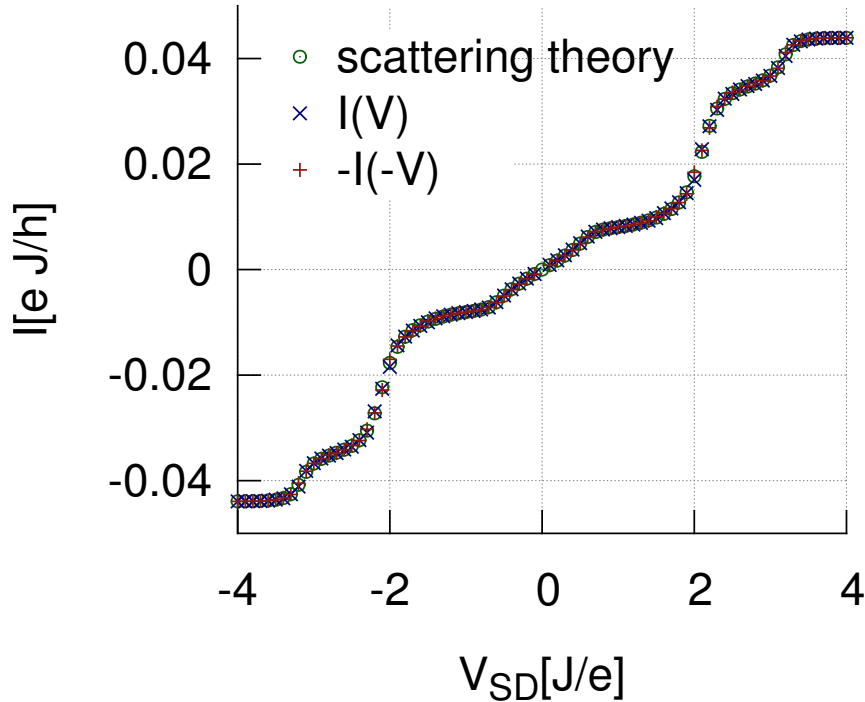
Figure 4.2: Result for the model given by Eq. (4.3), calculated via scattering theory (the blue 'x') and via exact diagonalization (the red '+'). The green circles denoting $-I(-V)$ are meant to visualize the size of the asymmetry. Parameters are $J_1 = 0.3J$, $J_2 = 0.09J$, $w_0 = -J$, $w_1 = 0.3J$, $w_2 = -0.3J$, $w_3 = 1.5J$ and for the diagonalization $M = 500$.

The current is calculated via Eq. (2.24) [8, 9, 10],

$$I = \frac{e}{h} \int_{-\frac{eV}{2}}^{\frac{eV}{2}} \mathrm{d}E \, |t(E)|^2 \,. \tag{4.6}$$

Fig. 4.2 shows the results from this scattering theory ansatz and from exact diagonalization for one set of parameters. The current asymmetry is zero within numerical precision in the whole parameter range.

For shifted energy bands, simulation using exact diagonalization leads to the current given in Fig. 4.3. An additional narrow resonance leads to very long decay times of the transient current, see Fig. 4.4. Fitting a straight line to the logarithm of the current between $Jt = 100\hbar$ and $Jt = 400\hbar$ gives a an exponential decaying current proportional to $I_{\text{trans}} \propto$
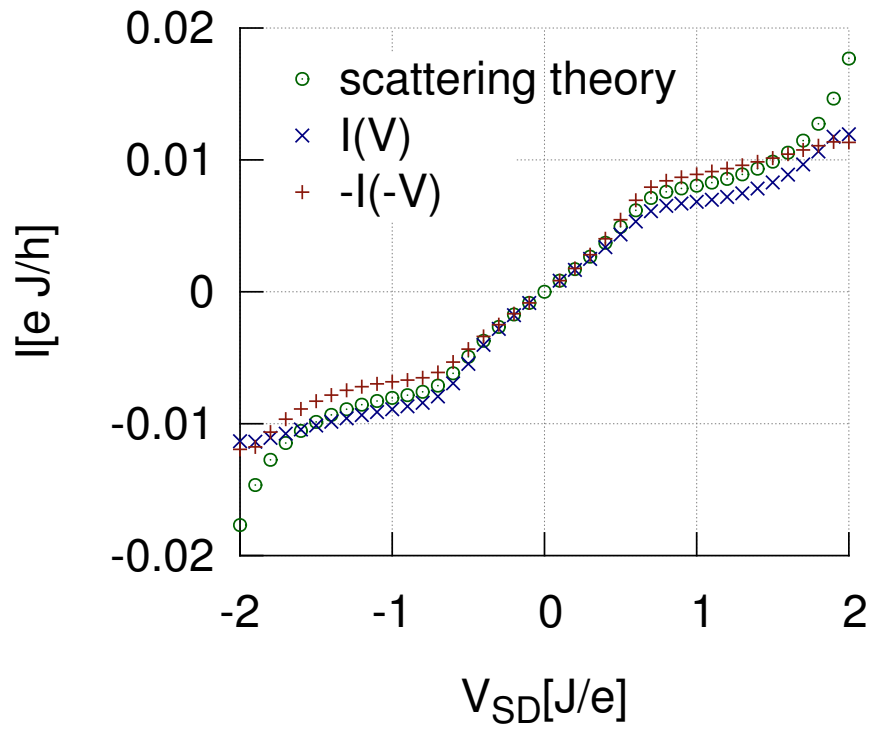
Figure 4.3: Result for the model given by Eq. (4.3) when considering shifted energy bands. The blue 'x' are the analytic results from Fig. 4.2. Parameters are $J_1 = 0.3J$, $J_2 = 0.09J$, $w_0 = -J$, $w_1 = 0.3J$, $w_2 = -0.3J$, $w_3 = 1.5J$, timesteps $J\Delta t = 0.25\hbar$ and System size $M = 1000$.
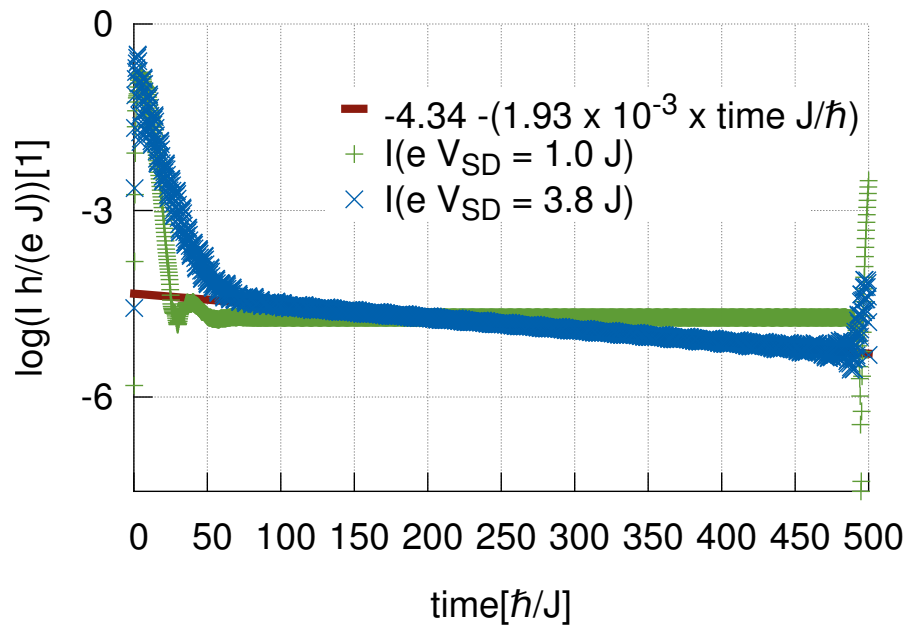
Figure 4.4: Logarithm of dimensionless current vs.time for model (4.3). The green '+' and blue 'x' are plotted data, the red line denotes the fit applied to the exponential decaying transient current. Parameters are $J_1 = 0.3J$, $J_2 = 0.09J$, $w_0 = -J$, $w_1 = 0.3J$, $w_2 = -0.3J$, $w_3 = 1.5J$, timesteps $J\Delta t = 0.25\hbar$ and System size $M = 1000$.

$\exp\left(-\left(0.00193 \pm 4 \cdot 10^{-6}\right) Jt/\hbar\right)$. The current at $Jt = 113\hbar$ has a value of $I = 0.0076\frac{eJ}{\hbar}$, the current obtained analytically for scattering theory calculations including the effect of finite finite bandwidth gives for that voltage $I(3.8J) = 0.0017\frac{eJ}{\hbar}$. In these calculations the upper and lower bound of the integral have to be adapted in case the voltage exceeds the bandwidth. It would take $Jt \gtrsim 3000\hbar$ for the transient current to decay to one percent of the value expected from the scattering theory calculations. A system size of $M \gtrsim 6000$ would be required for the plateau to persist to that time. This transient decay does not affect the currents for voltages in the range of $eV_{\mathrm{SD}} \in [-2J, 2J]$. In the case of shifted energy bands plotted in Fig. 4.3 a slight asymmetry is visible for large voltages. However there is no asymmetry in the scattering theory calculation, see Fig. 4.2. These results demonstrate that that the system described by the Hamiltonian of Eq. 4.3 is not sufficient to describe a diode under the constraints made in this work.

4.3 'Asymmetric charging'

Another candidate to cause rectification is the mechanism of 'asymmetric charging', with differing tunneling rates of the molecule to left and right lead. A more general simple model including this mechanism, an interacting resonant level model (IRLM) with in general asymmetric couplings and interactions sketched in Fig. 4.5, is investigated in Ref. [79]. The Hamiltonian of this model reads

$$
\begin{aligned}
\hat{\mathcal{H}} = &- J \sum_{x=-\infty}^{-2} \left(\hat{c}_x^\dagger \hat{c}_{x+1} + \hat{c}_{x+1}^\dagger \hat{c}_x \right) \\
&- J \sum_{x=1}^{\infty} \left(\hat{c}_x^\dagger \hat{c}_{x+1} + \hat{c}_{x+1}^\dagger \hat{c}_x \right) \\
&- J_{c_2} \left(\hat{c}_0^\dagger \hat{c}_1 + \hat{c}_1^\dagger \hat{c}_0 \right) - J_{c_1} \left(\hat{c}_{-1}^\dagger \hat{c}_0 + \hat{c}_0^\dagger \hat{c}_{-1} \right) \\
&- J_{nn_1} \left(\hat{n}_{-1} \, \hat{n}_0 \right) - J_{nn_2} \left(\hat{n}_0 \, \hat{n}_1 \right) ,
\end{aligned}
\tag{4.7}
$$

with the different J's being various hopping and coupling parameters. The paper concludes that asymmetries in the interactions between structure and leads do not lead to rectification. The 'asymmetric charging' mechanism, represented by asymmetries in the hopping elements between leads and structure, $J_{c_1} \neq J_{c_2}$, can cause an asymmetric I/V curve, but only for a 'nonlinear dispersion' [79]. The effect therefore depends on the band structure of the leads. The linear term in a Taylor expansion around the Fermi surface in the energy dispersion is required to be small compared to higher order terms.
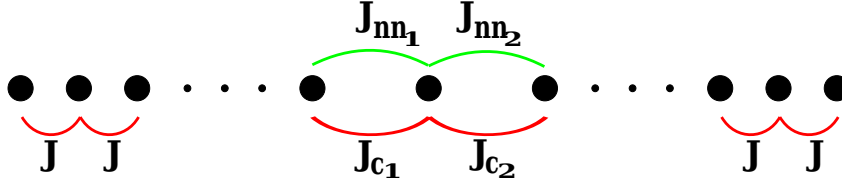
Figure 4.5: Sketch of the model used in Sec. 4.3. Red lines below the dots denote hopping, the green lines above the dots denote density-density interaction.

This statement is verified in this work by DMRG calculations. In order to be sensitive to details of the dispersion, simulations are run for shifted energy bands and for the scattering theory setup. The importance of nonlinear terms in the cosine dispersion relation of the tight binding leads, discussed in Sec. 2.3.4, needs to be increased for the DMRG simulation. Filling the leads only up to crystal momentum $k = \frac{\pi}{4}$ instead of $\frac{\pi}{2}$ yields the desired result.

The resulting currents are displayed in Figs. 4.6-4.9. In Fig. 4.6 the $I(V)$ and $I(-V)$ characteristic are compared for shifted energy bands. As predicted, no asymmetry is found in the I/V characteristic. This also holds true for the case of the initial density distribution influenced by voltage, see Fig. 4.7. Consistent with prediction, the current in Fig. 4.8 is asymmetric with respect to the voltage in the case of shifted energy bands, symmetric interactions and asymmetric junctions. As shown in Fig. 4.9 this asymmetry reduces to the order of the finite size effects in scattering theoretic setups. This verifies the conclusion from Ref. [79]. The asymmetry relies on environmental factors and therefore this mechanism is not in line with the purposes of this work.

4.4 Proposed model and Results

None of the mechanisms investigated so far rectifies currents in scattering theory. Revisiting the scattering theoretic approach [12] helps to understand why. It also clarifies which kind of ingredient is needed for rectification and therefore why the model proposed in this section causes asymmetric I/V. In Sec. 2.3.4 a scattering theoretical expression for the current in case of small voltages is derived using the Landauer approach [8, 9, 10]. The main general result, Eq. (2.24), states that the voltage $eV_{\text{SD}} = \mu_{\text{L}} - \mu_{\text{R}}$ enters the result via the integration borders while the details of the system enter via
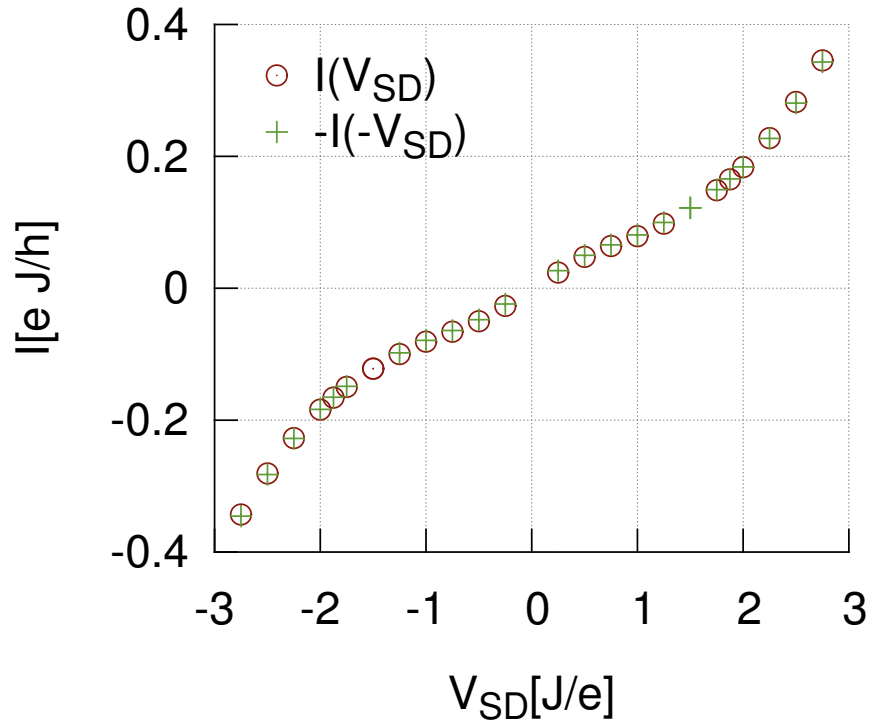
Figure 4.6: Current vs. bias voltage in an IRLM system for a total system size $M = 140$, quarter filling, left lead to impurity density-density interaction $J_{nn_1} = 0.2J$, system to right lead density-density interaction $J_{nn_2} = 0.5J$, timesteps $J\Delta t = 0.25\hbar$ and system to lead hopping $J_c = 0.5J$. Here, the bias voltage affects the time evolution Hamiltonian. The red 'o' mark the current itself, the green '+' mark -I(-U) to visualize the size of the asymmetry.
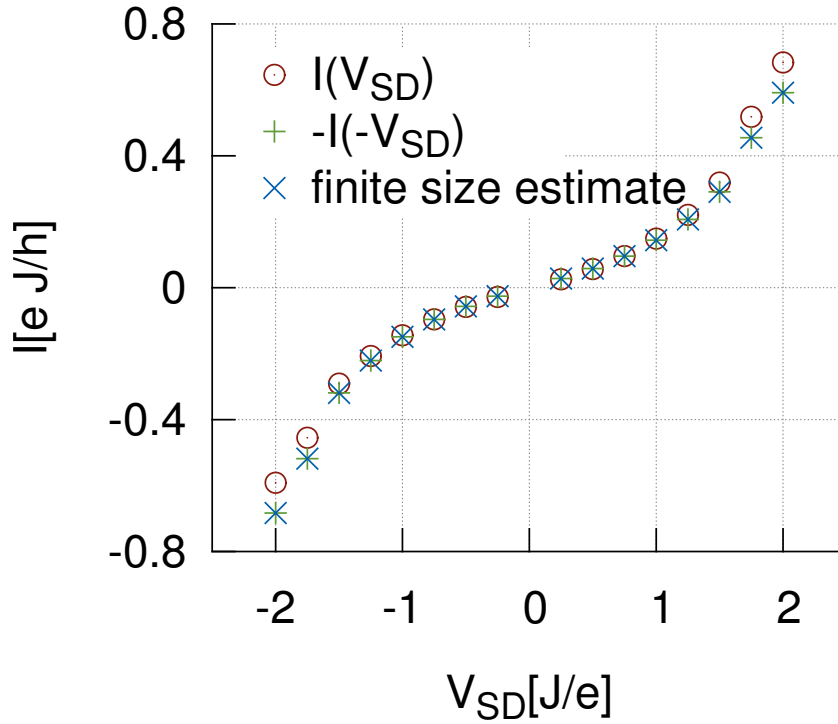
Figure 4.7: Current depending on bias voltage in IRLM system for system size $M = 140$, quarter filling, left lead to system density-density interaction $J_{nn_1} = 0.2J$, system to right lead density-density interaction $J_{nn_2} = 0.8J$, timesteps $J\Delta t = 0.25\hbar$ and system to lead hopping $J_c = 0.5J$. The red 'o' mark the current itself, the green '+' mark -I(-V) to visualize the size of the asymmetry, and the blue 'x' mark the current for swapped left and right lead to give an estimate of the finite size effects. The bias voltage is used to alter the initial state.
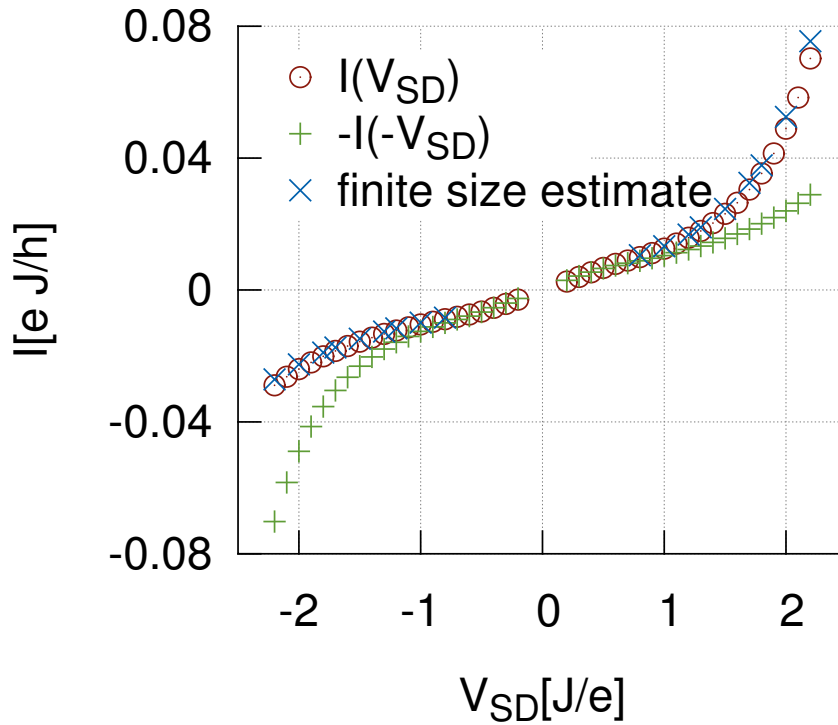
Figure 4.8: Current vs. bias voltage in an IRLM system of total system size $M = 140$, quarter filling, density-density interaction $J_{nn_{1/2}} = 0.5J$, time steps $J\Delta t = 0.25\hbar$, left lead to system hopping $J_{c_1} = 0.2J$ and system to right lead hopping $J_{c_2} = 0.5J$. The bias voltage is included in the time evolution Hamiltonian. The red 'o' mark the current itself, the green '+' mark -I(-U) to visualize the size of the asymmetry, and the blue 'x' mark the current for swapped left and right lead to give an estimate of the finite size effects.
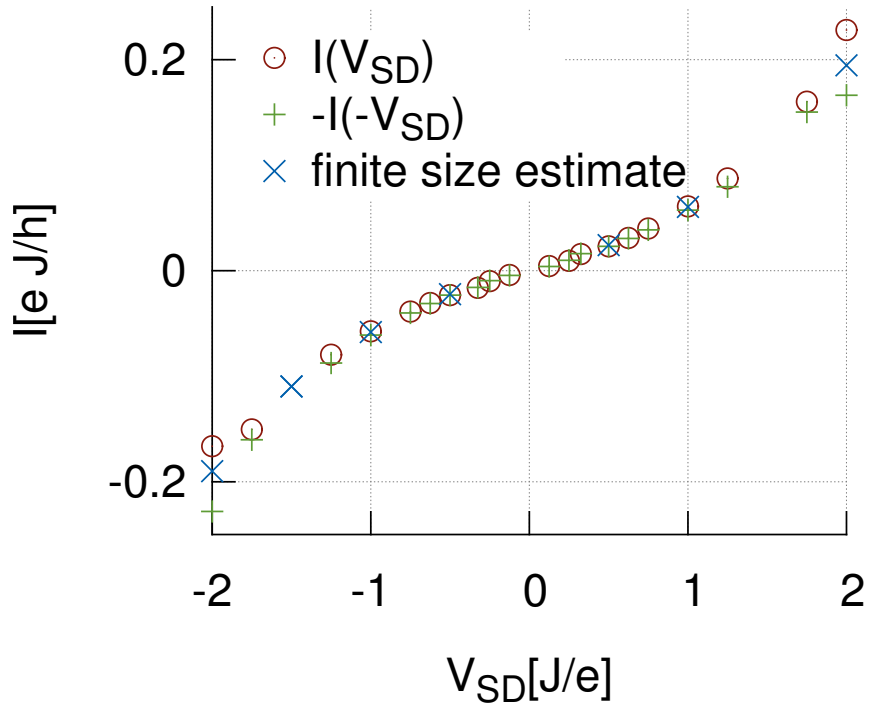
Figure 4.9: Current depending on bias voltage in IRLM system for system size $M = 130$, quarter filling, left lead to system hopping $J_{c_1} = 0.2J$, system to right lead hopping $J_{c_2} = 0.8J$, timesteps $J\Delta t = 0.25\hbar$ and density-density interaction strength $J_{nn_{1/2}} = 0.5J$. The red 'o' mark the current itself, the green '+' mark -I(-V) to visualize the size of the asymmetry, and the blue 'x' mark the current for swapped left and right lead to give an estimate of the finite size effects. In this calculation the bias voltage enters the Hamiltonian that determines the initial state.
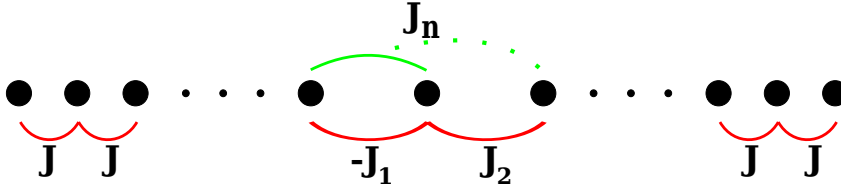
Figure 4.10: Sketch of our proposed model. Red lines below the dots denote hopping, the green lines above the correlated hopping term.

the transmission amplitude $T = |t|^2$:

$$\left\langle \hat{I}_0 \right\rangle = -\frac{eJ}{2\pi\hbar} \int_{-\frac{eV_{\text{SD}}}{2}}^{\frac{eV_{\text{SD}}}{2}} dE\, T. \tag{4.8}$$

In the cases considered above, the transmission amplitude only depends on the energy, $T = T(E)$. In those cases a sign change in the voltage only swaps the integration borders and the equation

$$\left\langle \hat{I}_0 \right\rangle (eV_{\text{SD}}) = -\left\langle \hat{I}_0 \right\rangle (-eV_{\text{SD}}) \tag{4.9}$$

necessarily holds, giving an antisymmetric I/V. In order to introduce an asymmetry a voltage dependence of the transmission needs to be introduced. This corresponds to a system with parameters sensitive for the voltage applied. For scattering theory this statement is equivalent to the condition that the parameters of the system have to be sensitive to the density distribution in the leads. In the model proposed in this work the condition is satisfied by introduction of a correlated hopping interaction, leading to a description of the system via the Hamiltonian sketched in Fig. 4.10:

$$\begin{aligned}
\hat{\mathcal{H}} = &- J \sum_{x=-\frac{M}{2}}^{-2} \left(\hat{c}_x^\dagger \hat{c}_{x+1} + \hat{c}_{x+1}^\dagger \hat{c}_x \right) \\
&- J \sum_{x=1}^{\frac{M}{2}-1} \left(\hat{c}_x^\dagger \hat{c}_{x+1} + \hat{c}_{x+1}^\dagger \hat{c}_x \right) \\
&- J_2 \left(\hat{c}_0^\dagger \hat{c}_1 + \hat{c}_1^\dagger \hat{c}_0 \right) \\
&- (J_n\, \hat{n}_1 - J_1) \left(\hat{c}_{-1}^\dagger \hat{c}_0 + \hat{c}_0^\dagger \hat{c}_{-1} \right).
\end{aligned} \tag{4.10}$$

In terms of mechanisms, the 'asymmetric charging' model discussed in Sec. 4.3 describes molecules with a strong but constant polarization. The model pro-
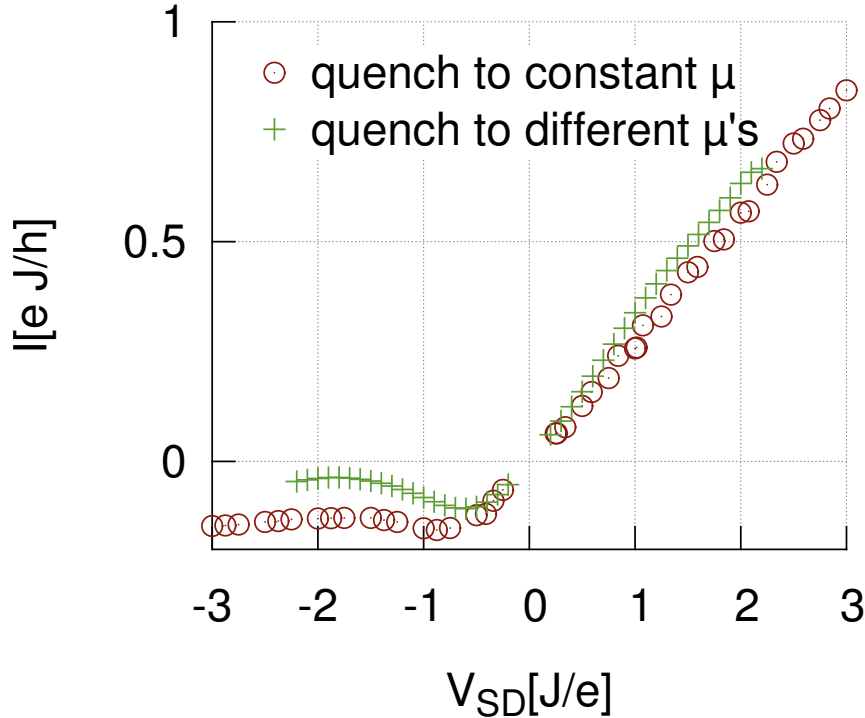
Figure 4.11: Result for the value of the current plateau (measured at $x = 0$) for $J_1 = 0.11J$, $J_2 = 0.5J$, $J_n = 0.5J$, system size $M = 110$ and timestep size $J\Delta t = 0.25\hbar$.

posed in this section describes a strongly polarizable molecule that gets polarized by the applied voltage, with a polarization strength depending on the applied voltage.

Numerical simulation of the current measurement leads to the I/V shown in Fig. 4.11. Due to the finite size of the leads there are finite gaps between the energy levels. This means that new levels are occupied or emptied only after discrete shifts in the electrostatic potentials, leading to the observation of steps in the I/V curve. The steps get smoother for bigger systems. For general parameters the resulting I/V is a mix of the results in the two limiting cases. For a vanishing polarizing hopping term $J_n = 0$ the standard resonant level result is obtained. It is approximately an arcus tangens, as calculated in Eq. (2.29). A pure polarizable hopping, $J_1 = 0$, gives an asymmetric I/V with minimum at roughly $eV_{\rm SD} = -J$. Current values and exact form of course depend on the choice of J_1 and J_n. This situation is plotted in
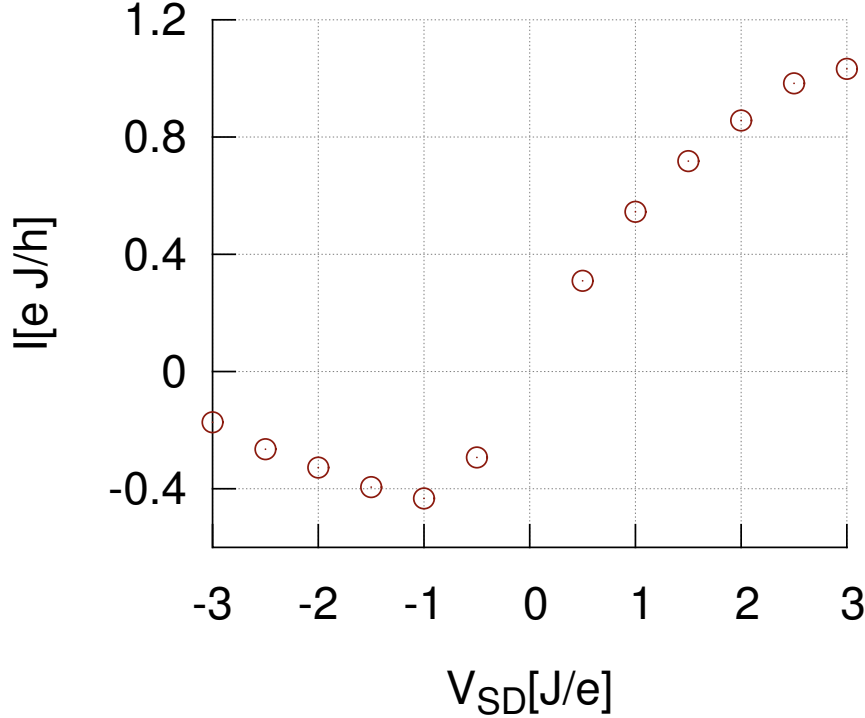
Figure 4.12: Current depending on bias voltage for $J_1 = 0$, $J_2 = 0.5J$, $J_n = -0.5J$, system size $M = 50$ and time step size $J\Delta t = 0.25\hbar$.

Fig. 4.12.

Two of the three regions characterizing a diode, the forward bias region with high conductivity and the reverse bias region with low but finite saturation current, are generated by the interaction. To see the breakdown region, in which electrons from lower bands are excited into the conduction band, more than just one energy band would be needed. The steady states obtained during the simulation of the I/V in Fig. 4.11 as well as the curves fitted to them are shown in Fig. 4.13 for a small selection of voltages. Fig. 4.14 enables a closer look at the transient regime. The behaviour of currents in the large reverse bias regime is showcased by the current at $eV_{\text{SD}} = -2J$. A peak at early times is followed by a fast drop and an unusually fast decay of the transient oscillations.

Fig. 4.11 contains the simulation results for both shifted bands and different occupation numbers in the leads. While the asymmetry is tailored for scattering theory where the density differs for the two leads, it is also
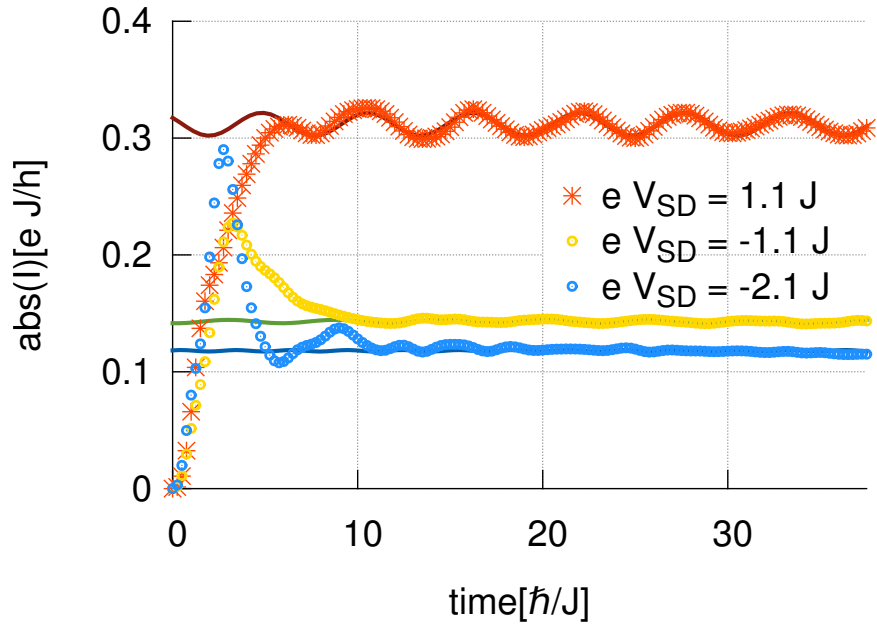
Figure 4.13: Absolute value of the current over time for various bias voltages for $J_1 = 0.11J$, $J_2 = 0.5J$, $J_n = 0.5J$, system size $M = 110$ and timestep size $J\Delta t = 0.25\hbar$. The case of shifted energy bands is plotted. Continuous lines are fits to extract the plateau value of the current for I/V curves.
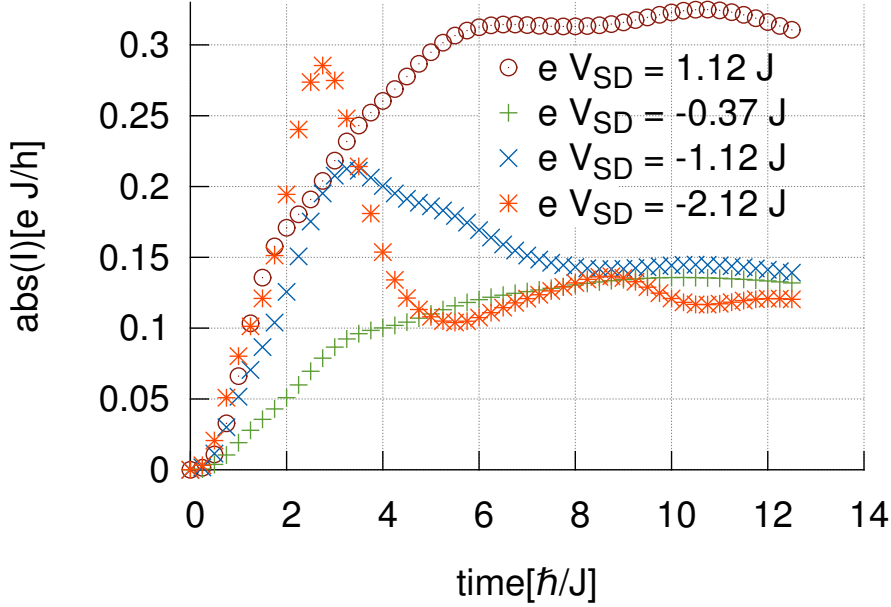
Figure 4.14: Absolute value of the current over time for $J_1 = 0.11J$, $J_2 = 0.5J$, $J_n = 0.5J$, system size $M = 110$ and timestep size $J\Delta t = 0.25\hbar$. Currents are plotted before current suppression ($eV_{SD} = -0.37J$), at its onset ($eV_{SD} = -1.12J$), in the reverse bias regime ($eV_{SD} = -2.12J$) and in the forward bias regime.

observed for the metallic case describing two leads with equal initial particle density. This hints at the robustness of the effect against environmental influences.

4.5 A bridge rectifier

One practical application of diodes is the bridge rectifier [87]. A bridge rectifier has two incoming and two outgoing leads, with an alternating voltage applied between the two incloming leads. The basic operation of the rectifier is to transform the voltage with changing sign into a strictly positive voltage between the two outgoing leads. This is achieved by connecting each incoming lead with each outgoing lead via one diode, respectively. The direction in which current can flow through the diode changes with each permutation of choice of incoming and outgoing lead. This section discusses the realization of the basis operation of a bridge rectifier using the rectification effect of the model proposed in last section.
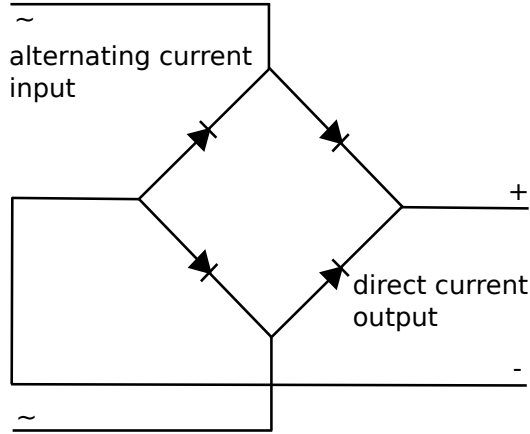
Figure 4.15: An illustration of the basic bridge rectifier setup including four diodes.

In a naive assessment of the situation four uniform diodes are required in the construction of the basic bridge rectifier unit sketched in Fig. 4.15. The change of forward bias direction between the different diodes is then achieved by swapping incoming and outgoing wire at the corresponding diode device. This does not work for the mechanism reduced to the simple model presented here. The molecule is only sensitive to the voltage in the wire connected via the interacting hopping term. However, voltage is only applied to the incoming wires, so it is always them being connected to the molecule via the interacting hopping term. The different directions of rectification are realized by different choices of parameters. The Hamiltonian describing bridge rectifier and leads is

$$\hat{\mathcal{H}} = \hat{\mathcal{H}}_{\mathrm{L1/2}} + \hat{\mathcal{H}}_{\mathrm{LD}} + \hat{\mathcal{H}}_{\mathrm{D}} + \hat{\mathcal{H}}_{\mathrm{DL}} + \hat{\mathcal{H}}_{\mathrm{L3/4}}, \qquad (4.11)$$

with $\hat{\mathcal{H}}_{\mathrm{L1/2}}$ the term covering the incoming leads (one and two) acting as baths, $\hat{\mathcal{H}}_{\mathrm{LD}}$ the connection between incoming leads and diodes, $\hat{\mathcal{H}}_{\mathrm{D}}$ the four diodes, $\hat{\mathcal{H}}_{\mathrm{DL}}$ connections between diodes and outgoing leads and $\hat{\mathcal{H}}_{\mathrm{L3/4}}$ the

outgoing leads (three and four) acting as baths. The single terms read

$$\hat{\mathcal{H}}_{\text{L}1/2} = -J \sum_{x=2}^{2L-1} \left(\hat{c}_x^\dagger \hat{c}_{x-2} + \hat{c}_{x-2}^\dagger \hat{c}_x \right), \tag{4.12}$$

$$\hat{\mathcal{H}}_{\text{D}} = \hat{\mathcal{H}}_{\text{w}1-4} + \hat{\mathcal{H}}_{\text{mol}} + \hat{\mathcal{H}}_{\text{w}5-8}, \tag{4.13}$$

$$\hat{\mathcal{H}}_{\text{w}1-4} = -J \sum_{x=2L+4}^{2L+15} \left(\hat{c}_x^\dagger \hat{c}_{x-4} + \hat{c}_{x-4}^\dagger \hat{c}_x \right), \tag{4.14}$$

$$\hat{\mathcal{H}}_{\text{mol}} = - \sum_{x=2L+20}^{2L+21} \left((J_3 - g_2 \hat{n}_{x-6}) \left(\hat{c}_{x-2}^\dagger \hat{c}_{x+2} + \hat{c}_{x+2}^\dagger \hat{c}_{x-2} \right) \right.$$
$$\left. - (g\hat{n}_{x-8} - J_1) \left(\hat{c}_{x-4}^\dagger \hat{c}_x + \hat{c}_x^\dagger \hat{c}_{x-4} \right) \right)$$
$$- J_2 \sum_{x=2L+16}^{2L+19} \left(\hat{c}_{x-4}^\dagger \hat{c}_x + \hat{c}_x^\dagger \hat{c}_{x-4} \right), \tag{4.15}$$

$$\hat{\mathcal{H}}_{\text{w}5-8} = -J \sum_{x=2L+24}^{2L+35} \left(\hat{c}_x^\dagger \hat{c}_{x-4} + \hat{c}_{x-4}^\dagger \hat{c}_x \right), \tag{4.16}$$

$$\hat{\mathcal{H}}_{\text{L}3/4} = -J \sum_{x=2L+38}^{4L+35} \left(\hat{c}_x^\dagger \hat{c}_{x-2} + \hat{c}_{x-2}^\dagger \hat{c}_x \right), \tag{4.17}$$

$$\hat{\mathcal{H}}_{\text{LD}} = \hat{\mathcal{H}}_{\text{L1D1}} + \hat{\mathcal{H}}_{\text{L1D3}} + \hat{\mathcal{H}}_{\text{L2D2}} + \hat{\mathcal{H}}_{\text{L2D4}}, \tag{4.18}$$

$$\hat{\mathcal{H}}_{\text{L1D1}} = -J \left(\hat{c}_{2L}^\dagger \hat{c}_{2L-2} + \hat{c}_{2L-2}^\dagger \hat{c}_{2L} \right), \tag{4.19}$$

$$\hat{\mathcal{H}}_{\text{L1D3}} = -J \left(\hat{c}_{2L+2}^\dagger \hat{c}_{2L-2} + \hat{c}_{2L-2}^\dagger \hat{c}_{2L+2} \right), \tag{4.20}$$

$$\hat{\mathcal{H}}_{\text{L2D2}} = -J \left(\hat{c}_{2L+1}^\dagger \hat{c}_{2L-1} + \hat{c}_{2L-1}^\dagger \hat{c}_{2L+1} \right), \tag{4.21}$$

$$\hat{\mathcal{H}}_{\text{L2D4}} = -J \left(\hat{c}_{2L+3}^\dagger \hat{c}_{2L-1} + \hat{c}_{2L-1}^\dagger \hat{c}_{2L+3} \right), \tag{4.22}$$

$$\hat{\mathcal{H}}_{\text{DL}} = \hat{\mathcal{H}}_{D1L3} + \hat{\mathcal{H}}_{D2L3} + \hat{\mathcal{H}}_{D3L4} + \hat{\mathcal{H}}_{D4L4}, \tag{4.23}$$

$$\hat{\mathcal{H}}_{D1L3} = -J \left(\hat{c}_{2L+36}^\dagger \hat{c}_{2L+32} + \hat{c}_{2L+32}^\dagger \hat{c}_{2L+36} \right), \tag{4.24}$$

$$\hat{\mathcal{H}}_{D2L3} = -J \left(\hat{c}_{2L+36}^\dagger \hat{c}_{2L+33} + \hat{c}_{2L+33}^\dagger \hat{c}_{2L+36} \right), \tag{4.25}$$

$$\hat{\mathcal{H}}_{D3L4} = -J \left(\hat{c}_{2L+37}^\dagger \hat{c}_{2L+34} + \hat{c}_{2L+34}^\dagger \hat{c}_{2L+37} \right), \tag{4.26}$$

$$\hat{\mathcal{H}}_{D4L4} = -J \left(\hat{c}_{2L+37}^\dagger \hat{c}_{2L+35} + \hat{c}_{2L+35}^\dagger \hat{c}_{2L+37} \right). \tag{4.27}$$

Here, the term $\hat{\mathcal{H}}_{\text{w}1-4}$ denotes wires connecting the leads one and two to the diodes and $\hat{\mathcal{H}}_{\text{w}5-8}$ denotes wires connecting the diodes to leads five till

eight. The term $\hat{\mathcal{H}}_{\mathrm{DxLy}}$ connects the wire outgoing from diode x to lead y, and the term $\hat{\mathcal{H}}_{\mathrm{LyDx}}$ connects incoming lead y to the wire leading to diode x. The variable L gives the length of each lead, such that the system size is $M = 4L + 36$. The sketch in Fig. 4.16 helps getting an overview of the setup. The voltage is applied via the term

$$\hat{\mathcal{H}}_V = \frac{eV_{\mathrm{SD}}}{2} \sum_{x=0}^{2L+11} \left((-1)^x \, \hat{\mathrm{n}}_x \right). \tag{4.28}$$

Instead of a time-dependent alternating voltage, two voltages with same absolute value and different sign are applied in a first step. Parameters $g = 0.5J$, $J_1 = 0.11J$ and $J_2 = 0.5J$ are chosen in order to match the parameters of the system producing the diodelike I/V in Fig. 4.11. The parameter g_2 is chosen such that effective hopping for rectification in both directions has the same scaling with voltage, which means $g_2 = g$. Also J_3 should produce the same effective hopping as for the diode in reverse direction. This means that for zero voltage or average lead density $2n = 1$, the equation

$$n \cdot g - J_1 = J_3 - n \cdot g \tag{4.29}$$

needs to be satisfied, meaning that $J_3 = 0.39J$. The last two conditions lead to four diodes with effectively the same behaviour, and two of them being connected in reverse direction.

The system is investigated by simulating the current through the outgoing leads. For that purpose the current is averaged over the first two sites in each lead, then the difference between the currents of the two outgoing leads is plotted. So the object plotted is

$$I_{\mathrm{diff}} (V_{\mathrm{SD}}) = -\frac{1}{2} \sum_{x=2L+36}^{2L+39} (-1)^x \left\langle \hat{\mathrm{I}}_x \right\rangle (V_{\mathrm{SD}}). \tag{4.30}$$

For $L = 20$ sites per lead no current plateau was reached. Larger systems are unfortunately very costly in computational effort. The result for $L = 40$ after a few timesteps, resulting from 120 days of computation, is shown in Fig. 4.17. The onset of current corresponds to the measurement position being at the beginning of the two leads. After passing the molecule the charge carriers have to travel eight sites with a Fermi velocity of two sites per unit of time before they reach the leads and the current changes. No current plateau is shown. However, the currents clearly have the same sign for applied bias voltages of opposite sign, and do not change sign over time. Therefore, a particle density difference between the two leads accumulates
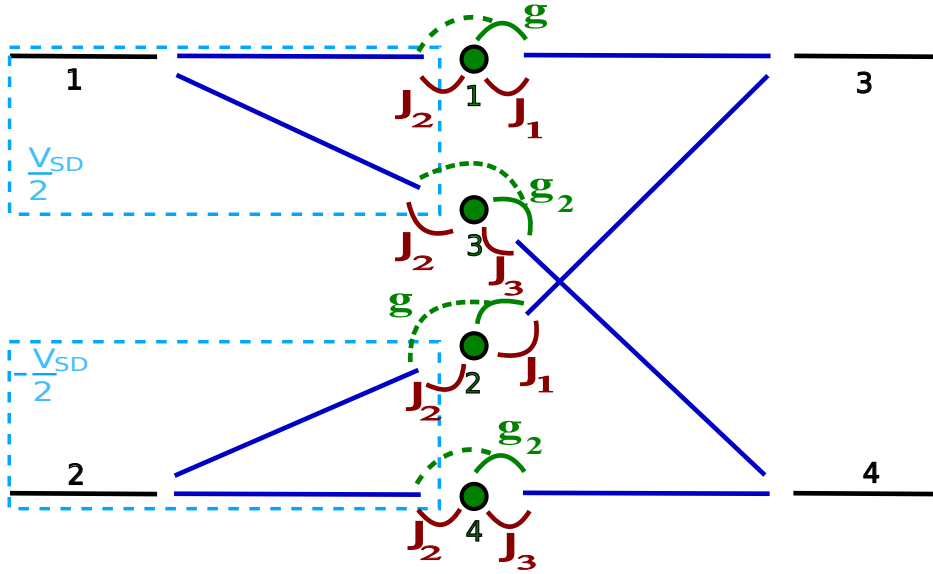
Figure 4.16: Sketch of the bridge rectifier model. Black lines correspond to $\hat{\mathcal{H}}_{\mathrm{L1/2}}$ and $\hat{\mathcal{H}}_{\mathrm{L3/4}}$, blue lines to $\hat{\mathcal{H}}_{\mathrm{w1-4}}$ and $\hat{\mathcal{H}}_{\mathrm{w5-8}}$. Bright blue frames enclose leads which are put at the electrostatic potential given by the bright blue number inside the frame. Green dots denote the sites of the molecules. Terms in $\hat{\mathcal{H}}_{\mathrm{mol}}$ are given explicitly, with normal hopping terms given by continuous red lines and correlated hopping given by green lines. The continuous part connects the sites connected by the hopping, the dotted lines connect the continuous line to the site which influences the hopping. Black lines labeled x are connected to the neighboring blue lines leading to molecules labeled y by $\hat{\mathcal{H}}_{\mathrm{LxDy}}$ or $\hat{\mathcal{H}}_{\mathrm{DyLx}}$.
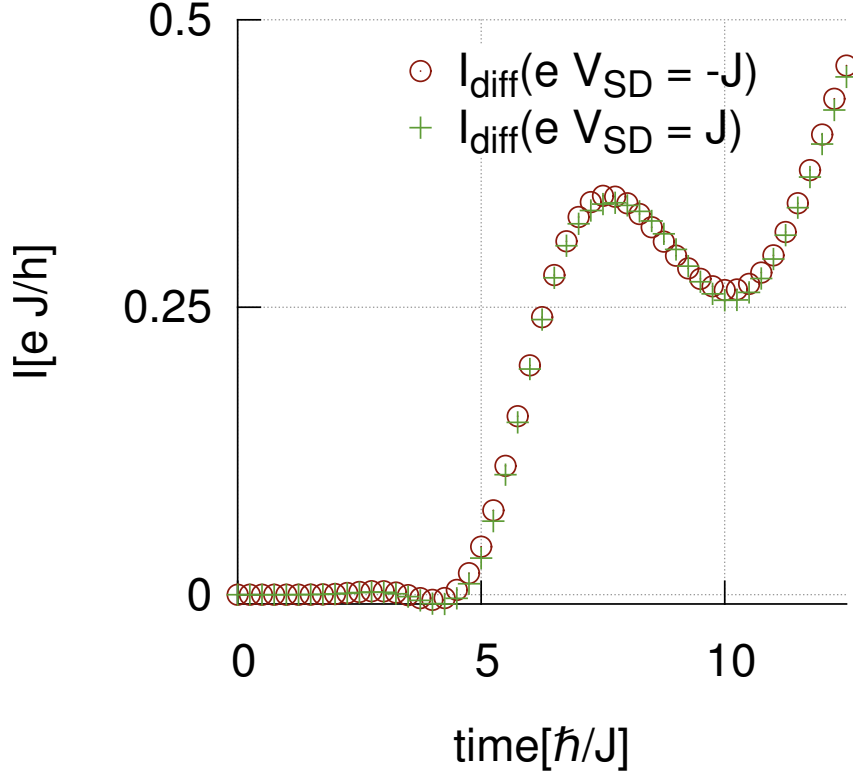
Figure 4.17: Current over time for the model given in Eq. (4.11). Parameters are $L = 40$, $g = 0.5J$, $J_1 = 0.11J$, $J_2 = 0.5J$, $g_2 = 0.5J$ and $J_3 = 0.39J$. Timesteps $J\Delta t = 0.25\hbar$ were used.

over time. The difference does not depend on the applied voltage and can be interpreted as difference in bias potential. This is a strong hint that the rectifier model should work, given enough time for the simulation.

4.6 Conclusion

In this chapter a mechanism causing molecular rectification independently of assumptions on the environment has been searched for. Prominent proposals have been revisited. Although these proposals can rectify under the right conditions, they do not rectify currents universally. The reasons for this have been investigated. The cause of the failure to rectify is found in the assumption of static setups within the models, where the underlying system does not react to the applied voltage. A model is proposed which corresponds to an effective RLM. In this model the effective parameter characterising the

RLM, the resonance width, changes with varying voltage. It changes the behaviour of the whole system, corresponding to the molecule reacting to the applied voltage. This fact allows the molecule to rectify currents by itself, independently of external factors.

This quality allows for universally applicable devices. A model for such a device, namely a bridge rectifier, has been proposed. Its behaviour has been simulated for static applied bias. The simulation strongly hints that the device functions correctly. If not for the high cost in computational time the next step would be to simulate a dynamic bias. This could be achieved by an initial density profile strongly varying over the chain within the single leads, or by application of a time-dependent bias term. An implementation of a time-dependent voltage is discussed in the next chapter.

DMRG for fully time-dependent Hamiltonians

In 1992, Steven White proposed the density matrix renormalization group approach [24] (DMRG) as a generalization of the numerical renormalization group procedure by Kenneth Wilson [23]. The DMRG allowed for the calculation of ground state properties of low dimensional systems. Over time the DMRG was expanded to be applicable to time evolving problems [25, 69, 66, 67, 26, 68, 27]. In previous implementations of the time-dependent DMRG (td-DMRG), e.g. in Ref. [55], the time-dependence during time evolution consists of the switch between two otherwise constant Hamiltonians at a certain point in time. This allows to simulate quenches and hence nonequilibrium transport problems. However, for problems involving e.g. a time-dependent force driving the system or alternating currents, algorithms which are able to deal with more generic time-dependences are needed. In Ref. [25] Cazalilla and Marston use the Magnus expansion [88, 89] to simulate systems with Hamiltonians that change during time evolution. Their implementation uses the basis of the initial states, which is not necessarily suited for the representation of time evolved states and can lead to large errors [69]. This chapter introduces an implementation of the Magnus expansion which approximates time evolved states with only small errors.

The time-dependence of a system is described by the time-dependent Schrödinger equation,

$$i\hbar\partial_t \left|\phi\left(t\right)\right\rangle = \hat{\mathcal{H}}\left(t\right)\left|\phi\left(t\right)\right\rangle.$$

One popular solution to the equation is the Dyson series

$$|\phi(t)\rangle = \hat{T} \exp\left\{-\frac{i}{\hbar} \int_{t_0}^{t} dt' \hat{\mathcal{H}}(t')\right\} |\phi(t_0)\rangle,$$

where $\hat{T}$ denotes time ordering. In the corresponding perturbation theory, the series is approximated by its first few terms. This approximation does not preserve the unitarity of the time evolution operator. An alternative perturbation theory, which is used in this work, instead approximates the time evolution for small timesteps $J_c \Delta t = J_c(t - t_0) \ll \hbar$ by using the first few terms of the Magnus expansion [88, 89]. In this context J_c denotes the relevant energy scale in the Hamiltonian. This procedure is also known as time-dependent exponential perturbation theory. The td-DMRG algorithm evaluates operators of the form $\exp\left\{-\frac{i}{\hbar}\hat{\mathcal{H}}\Delta t\right\}$. Since the Magnus expansion expresses the time evolution as an exponential of a series of operators, as will be shown in the next section, this expansion of time evolution is rewritten as an expansion of the Hamiltonian. The exponential is exactly unitary in contrast to the expansion of the Dyson series, which is only unitary up to leading order in the perturbative expansion. Fully time-dependent Hamiltonians are then implemented by replacing the previously constant Hamiltonian at each step Δt of the time evolution with the first terms of a Magnus series resulting from a time-dependent Schrödinger equation. This procedure yields operators that depend on time. The time interval is then split into small timesteps Δt during which the operators are approximated as constant in time.

Section 5.1 contains an overview of the Magnus expansion. It is followed by an example up to second order, where the resonant level model (RLM, see Eq. (2.7)) with a time-dependent phase in the hopping between probe and leads as presented in Sec. 2.3.5 is considered. Resulting currents for the presented method and the given example are compared to reference results in Sec. 5.4. The reference results are calculated in an equivalent current measurement setup using a time-independent Hamiltonian and the standard td-DMRG algorithm. This serves as crosscheck and test of the extent of error introduced by the truncation.

5.1 Using the Magnus expansion

The Magnus series is a representation of the solution to the linear differential equation

$$\partial_t \hat{Y}(t) = \hat{A}(t) \hat{Y}(t). \tag{5.1}$$

Here, ∂_t is the differentiation towards some parameter t, and $\hat{A}(t)$ and $\hat{Y}(t)$ are some Matrices depending on t, with $\hat{A}$ known and $\hat{Y}$ to be found. This

equation is of great importance in physics. Substitution of $i\hbar\hat{A}$ with the Hamiltonian $\hat{\mathcal{H}}$ and $\hat{Y}$ with the time evolution operator transforms Eq. (5.1) into the Schrödinger equation for the time evolution operator.

Magnus has stated in Ref. [88] that the solution can be written in the form

$$\hat{Y}(t) = \exp\left\{\hat{\Omega}(t,t_0)\right\}\hat{Y}(t_0)$$

$$= \left[\exp\left\{\sum_{n=1}^{\infty}\hat{\Omega}_n(t,t_0)\right\}\right]\hat{Y}(t_0), \tag{5.2}$$

so that

$$\hat{\Omega}(t,t_0) = \sum_{n=1}^{\infty}\hat{\Omega}_n(t,t_0). \tag{5.3}$$

The single contributions $\hat{\Omega}_n$ are chosen such that a truncation after the n-th term approximates the full series up to an order of $\mathcal{O}((J_c\Delta t/\hbar)^{n+1})$. Again, J_c denotes the relevant energy scale of the system. The $\hat{\Omega}_n$ are calculated as shown in Ref. [89], i.e. recursively via

$$\hat{\Omega}_1(t,t_0) = \int_{t_0}^{t}\mathrm{d}t'\hat{A}(t')$$

$$\hat{\Omega}_n(t,t_0) = \sum_{j=1}^{n-1}\frac{B_j}{j!}\int_{t_0}^{t}\mathrm{d}t'\hat{S}_n^{(j)}(t',t_0)$$

$$\hat{S}_n^{(1)}(t',t_0) = \left[\hat{\Omega}_{n-1}(t,t_0),\hat{A}(t')\right]_{-}$$

$$\hat{S}_n^{(j)}(t',t_0) = \sum_{m=1}^{n-j}\left[\hat{\Omega}_m(t,t_0),\hat{S}_{n-m}^{j-1}(t',t_0)\right]_{-}. \tag{5.4}$$

Here, B_j denote the Bernoulli numbers.

As with the Dyson series, truncation of $\hat{\Omega}$ after the n-th order term $\hat{\Omega}_n$

leads to omission of terms of the order

$$\exp\left\{\hat{\Omega}\right\} - \exp\left\{\sum_{k=1} n\hat{\Omega}_k\right\} = \exp\left\{\sum_{k=1} n\hat{\Omega}_k + \mathcal{O}\left(\left(\frac{J_c\Delta t}{\hbar}\right)^{n+1}\right)\right\}$$

$$- \exp\left\{\sum_{k=1} n\hat{\Omega}_k\right\}$$

$$= \left(\exp\left\{\mathcal{O}\left(\left(\frac{J_c\Delta t}{\hbar}\right)^{n+1}\right)\right\} - 1\right) \times$$

$$\times \exp\left\{\sum_{k=1} n\hat{\Omega}_k\right\}$$

$$= \mathcal{O}\left(\left(\frac{J_c\Delta t}{\hbar}\right)^{n+1}\right). \tag{5.5}$$

In some cases, the convergence of the series is enhanced by small or vanishing contributions of the commutator between the Hamiltonians at different times, or between the Hamiltonian and the previous commutators in the series.

5.2 Time-dependent phase

In the case of an RLM with a time-dependent phase of the hopping between probe and leads as discussed in Sec. 2.3.5, the operator has the form

$$i\hbar\hat{A}\left(t\right) = \hat{h}_0 + \hat{h}_0^\dagger + f\left(t\right)\hat{h}_1 + f^*\left(t\right)\hat{h}_1^\dagger. \tag{5.6}$$

This gives the Schrödinger equation for a Hamiltonian which consists of a time-independent part and a part which time-dependence can be written into a scalar function. More general problems will not be discussed here, but their solution can be found in Ref. [90]. The ingredients of $\hat{A}$ read for $t \geq 0$

$$\hat{h}_0 = - J\left(\sum_{x=-\infty}^{-2}\left(\hat{c}_x^\dagger\hat{c}_{x+1}\right) + \sum_{x=1}^{\infty}\left(\hat{c}_x^\dagger\hat{c}_{x+1}\right)\right) + V_g\left(\hat{c}_0^\dagger\hat{c}_0\right), \tag{5.7}$$

$$\hat{h}_1 = - J_c\left(\hat{c}_0^\dagger\hat{c}_1 + \hat{c}_{-1}^\dagger\hat{c}_0\right), \tag{5.8}$$

$$f\left(t\right) = \exp\left(i\frac{V_{\text{SD}}}{2\hbar}t\right). \tag{5.9}$$

J and J_c are hopping constants, V_g is a gate voltage which is set to zero, V_{SD} is the bias voltage and $\hat{c}_x$ and $\hat{c}_x^\dagger$ are the annihilation and creation operator

at site x. In the td-DMRG, time is discretized into timesteps Δt. In this section, the approximated time evolution operator for one single timestep Δt from t_0 to t is calculated. Since the time evolution used in this thesis requires constant Hamiltonians, the Hamiltonian is approximated for small timesteps by $\hat{\Omega}(t)$. Up to second order the series reads

$$\hat{Y}(t, t_0) = \exp\left(\hat{\Omega}(t - t_0)\right),$$

$$\hat{\Omega}(t - t_0) = \hat{\Omega}_1 - \frac{1}{2}\hat{\Omega}_2 + ...$$

$$= \int_{t_0}^{t} dt_1 \hat{A}(t_1) - \frac{1}{2}\int_{t_0}^{t} dt_1 \int_{t_0}^{t_1} dt_2 \left[\hat{A}(t_1), \hat{A}(t_2)\right]_- + ... \quad (5.10)$$

Within the single timestep, this corresponds to the time-independent solution with Hamiltonian

$$\hat{\mathcal{H}} = i\hbar \frac{\hat{\Omega}}{t - t_0}$$

$$= \hat{\mathcal{H}}_1 - \frac{i}{\hbar}\hat{\mathcal{H}}_2 + ..., \quad (5.11)$$

$$\hat{\mathcal{H}}_1 = \hat{h}_0 + \hat{h}_0^\dagger + \hat{h}_1 \mathcal{F}_1(t, t_0) + \hat{h}_1^\dagger \mathcal{F}_{1,cc}(t, t_0),$$

$$\mathcal{F}_1(t, t_0) = \frac{1}{t - t_0}\int_{t_0}^{t} dt_1 f(t_1),$$

$$= \mathrm{Re}\left(\mathcal{F}_1(t, t_0)\right) + i\mathrm{Im}\left(\mathcal{F}_1(t, t_0)\right),$$

$$\mathcal{F}_{1,cc}(t, t_0) = \frac{1}{t - t_0}\int_{t_0}^{t} dt_1 f^*(t_1)$$

$$= \mathrm{Re}\left(\mathcal{F}_1(t, t_0)\right) - i\mathrm{Im}\left(\mathcal{F}_1(t, t_0)\right)$$

$$\rightarrow \hat{\mathcal{H}}_1 = \left(\hat{h}_0 + \hat{h}_0^\dagger\right) + \mathrm{Re}\left(F_1(t, t_0)\right)\left(\hat{h}_1 + \hat{h}_1^\dagger\right)$$

$$+ i\mathrm{Im}\left(F_1(t, t_0)\right)\left(\hat{h}_1 - \hat{h}_1^\dagger\right). \quad (5.12)$$

Note that for $t \to t_0$, $F_1(t, t_0) \to f(t)$ and higher orders in the expansion tend to zero, so that the continuous limit is restored. Also, the antihermitian operator $(\hat{h}_1 - \hat{h}_1^\dagger)$ gets multiplied by a purely imaginary part so that $\hat{\mathcal{H}}_1$ again is hermitian and therefore the time evolution operator up to first order, $\exp\{-\frac{i}{\hbar}\hat{\mathcal{H}}_1\}$, is unitary. The use of Eq. (5.9) leads to

$$\mathrm{Re}\left(\mathcal{F}_1(t, t_0)\right) = \frac{2\hbar\left[\sin\left(\frac{V_{SD}}{2}t\right) - \sin\left(\frac{V_{SD}}{2}t_0\right)\right]}{V_{SD}(t - t_0)},$$

$$\mathrm{Im}\left(\mathcal{F}_1(t, t_0)\right) = \frac{2\hbar\left[\cos\left(\frac{V_{SD}}{2}t_0\right) - \cos\left(\frac{V_{SD}}{2}t\right)\right]}{V_{SD}(t - t_0)}. \quad (5.13)$$

5.3 Second order

Considering terms of second order yields (5.11) with

$$
\begin{aligned}
\hat{\mathcal{H}}_2 =& \frac{1}{2(t-t_0)} \int_{t_0}^{t} \mathrm{d}t_1 \int_{t_0}^{t_1} \mathrm{d}t_2 \left[\hat{A}(t_1), \hat{A}(t_2)\right]_{-} \\
=& \frac{1}{2(t-t_0)} \int_{t_0}^{t} \mathrm{d}t_1 \int_{t_0}^{t_1} \mathrm{d}t_2 \\
& \left[\hat{h}_0 + \hat{h}_0^{\dagger} + f(t_1)\hat{h}_1 + f^*(t_1)\hat{h}_1^{\dagger}, \hat{h}_0 + \hat{h}_0^{\dagger} + f(t_2)\hat{h}_1 + f^*(t_2)\hat{h}_1^{\dagger}\right]_{-} \\
=& \mathcal{F}_{2,1}(t,t_0) \left[\hat{h}_0, \hat{h}_1\right]_{-} + \mathcal{F}_{2,2}(t,t_0) \left[\hat{h}_0^{\dagger}, \hat{h}_1^{\dagger}\right]_{-} \\
& + \mathcal{F}_{2,1}(t,t_0) \left[\hat{h}_0^{\dagger}, \hat{h}_1\right]_{-} + \mathcal{F}_{2,2}(t,t_0) \left[\hat{h}_0, \hat{h}_1^{\dagger}\right]_{-} \\
& + \mathcal{F}_{2,3}(t,t_0) \left[\hat{h}_1^{\dagger}, \hat{h}_1\right]_{-}
\end{aligned}
\tag{5.14}
$$

$$
\begin{aligned}
\mathcal{F}_{2,1}(t,t_0) &= \frac{1}{2(t-t_0)} \int_{t_0}^{t} \mathrm{d}t_1 \int_{t_0}^{t_1} \mathrm{d}t_2 \left(f(t_2) - f(t_1)\right) \\
\mathcal{F}_{2,2}(t,t_0) &= \frac{1}{2(t-t_0)} \int_{t_0}^{t} \mathrm{d}t_1 \int_{t_0}^{t_1} \mathrm{d}t_2 \left(f^*(t_2) - f^*(t_1)\right) \\
\mathcal{F}_{2,3}(t,t_0) &= \frac{1}{2(t-t_0)} \int_{t_0}^{t} \mathrm{d}t_1 \int_{t_0}^{t_1} \mathrm{d}t_2 \left(f^*(t_1)f(t_2) - f(t_1)f^*(t_2)\right)
\end{aligned}
\tag{5.15}
$$

The scalar functions are given by

$$
\begin{aligned}
\mathrm{Re}\left[\mathcal{F}_{2,1}(t,t_0)\right] =& \frac{4\hbar^2}{V_{\mathrm{SD}}^2(t-t_0)} \left(\cos\left(\frac{V_{\mathrm{SD}}}{2}t_0\right) - \cos\left(\frac{V_{\mathrm{SD}}}{2}t\right)\right) \\
& - \frac{\hbar}{V_{\mathrm{SD}}} \left(\sin\left(\frac{V_{\mathrm{SD}}}{2}t\right) + \sin\left(\frac{V_{\mathrm{SD}}}{2}t_0\right)\right) \\
\mathrm{Im}\left[\mathcal{F}_{2,1}(t,t_0)\right] =& \frac{4\hbar^2}{V_{\mathrm{SD}}^2(t-t_0)} \left(\sin\left(\frac{V_{\mathrm{SD}}}{2}t_0\right) - \sin\left(\frac{V_{\mathrm{SD}}}{2}t\right)\right) \\
& + \frac{\hbar}{V_{\mathrm{SD}}} \left(\cos\left(\frac{V_{\mathrm{SD}}}{2}t\right) + \cos\left(\frac{V_{\mathrm{SD}}}{2}t_0\right)\right)
\end{aligned}
$$

$$\mathrm{Re}\left[\mathcal{F}_{2,2}\left(t,t_0\right)\right] = \mathrm{Re}\left[\mathcal{F}_{2,1}\left(t,t_0\right)\right]$$

$$\mathrm{Im}\left[\mathcal{F}_{2,2}\left(t,t_0\right)\right] = -\,\mathrm{Im}\left[\mathcal{F}_{2,1}\left(t,t_0\right)\right]$$

$$\mathrm{Re}\left[\mathcal{F}_{2,3}\left(t,t_0\right)\right] = 0$$

$$\mathrm{Im}\left[\mathcal{F}_{2,3}\left(t,t_0\right)\right] = \frac{4\hbar^2}{V_{\mathrm{SD}}^2\left(t-t_0\right)}\sin\left(\frac{V_{\mathrm{SD}}}{2}\left(t-t_0\right)\right) - \frac{2\hbar}{V_{\mathrm{SD}}} \tag{5.16}$$

and therefore

$$\hat{\mathcal{H}}_2 = \mathrm{Re}\left[\mathcal{F}_{2,1}\left(t,t_0\right)\right]\left[\hat{h}_0 + \hat{h}_0^\dagger,\,\hat{h}_1 + \hat{h}_1^\dagger\right]_-$$
$$+\,i\mathrm{Im}\left[\mathcal{F}_{2,1}\left(t,t_0\right)\right]\left[\hat{h}_0 + \hat{h}_0^\dagger,\,\hat{h}_1 - \hat{h}_1^\dagger\right]_-$$
$$+\,i\mathrm{Im}\left[\mathcal{F}_{2,3}\left(t,t_0\right)\right]\left[\hat{h}_1^\dagger,\hat{h}_1\right]_-. \tag{5.17}$$

As a next step commutators of the kind $[\hat{h}_0 + \hat{h}_0^\dagger,\,\hat{h}_1 + \hat{h}_1^\dagger]_-$ have to be calculated. Inserting Eq. (2.13), Eq. (5.7) and Eq. (5.8) results in

$$\left[\hat{h}_0 + \hat{h}_0^\dagger,\,\hat{h}_1 + \hat{h}_1^\dagger\right]_- = JJ_c\left(\hat{c}_2^\dagger\hat{c}_0 - \hat{c}_0^\dagger\hat{c}_{-2}\right) - \mathrm{h.c.}$$
$$\left[\hat{h}_0 + \hat{h}_0^\dagger,\,\hat{h}_1 - \hat{h}_1^\dagger\right]_- = JJ_c\left(\hat{c}_2^\dagger\hat{c}_0 - \hat{c}_0^\dagger\hat{c}_{-2}\right) + \mathrm{h.c.}$$
$$\left[\hat{h}_1^\dagger,\hat{h}_1\right]_- = J_c^2\left(\hat{c}_{-1}^\dagger\hat{c}_{-1} - \hat{c}_1^\dagger\hat{c}_1\right). \tag{5.18}$$

When calculating currents using this model, one should take into account that the Heisenberg equation leading to the current operator between sites $x = -1$ and $x = 0$, which was defined in Sec. 2.3.1, now involves the modified term

$$i\left[f\left(t\right)\hat{h}_1 + f^*\left(t\right)\hat{h}_1^\dagger,\hat{c}_0^\dagger\hat{c}_0\right]_- = 2J_c\sin\left(\frac{V_{\mathrm{SD}}}{2}t\right)\mathrm{Re}\left[\left(\hat{c}_1^\dagger\hat{c}_0 - \hat{c}_0^\dagger\hat{c}_{-1}\right)\right]$$
$$+\,2J_c\cos\left(\frac{V_{\mathrm{SD}}}{2}t\right)\mathrm{Im}\left[\left(\hat{c}_1^\dagger\hat{c}_0 - \hat{c}_0^\dagger\hat{c}_{-1}\right)\right]. \tag{5.19}$$

The current operator therefore now reads

$$\hat{I} = \frac{2ie}{\hbar}J_c\left(\cos\left(\frac{V_{\mathrm{SD}}}{2}t\right)\mathrm{Im}\left\{\hat{c}_1^\dagger\hat{c}_0\right\} + \sin\left(\frac{V_{\mathrm{SD}}}{2}t\right)\mathrm{Re}\left\{\hat{c}_1^\dagger\hat{c}_0\right\}\right). \tag{5.20}$$

5.4 Quality of the approximation

In Sec. 2.3.5 it was shown for the RLM that a time-dependent phase in the hopping between leads and probe leads to exactly the same current through

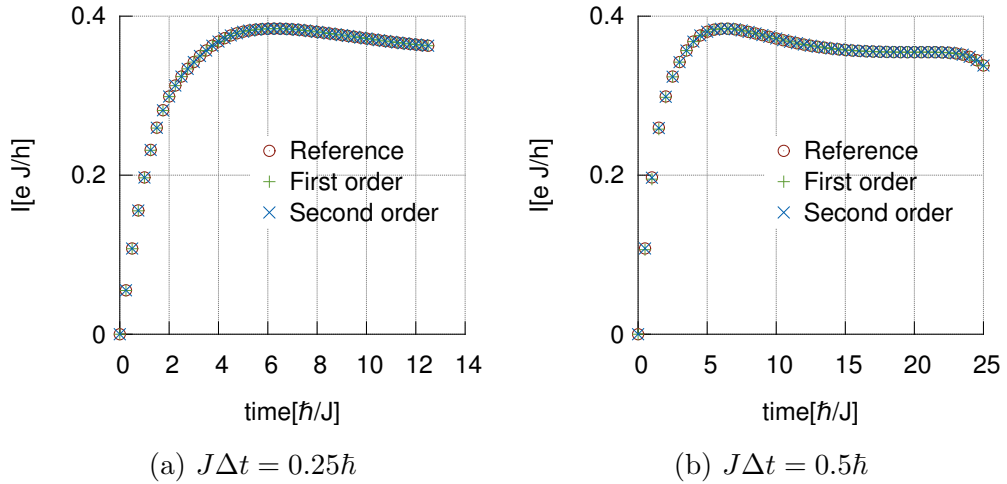(a) $J\Delta t = 0.25\hbar$ (b) $J\Delta t = 0.5\hbar$

Figure 5.1: Comparison of resulting currents, averaged over two neighboring sites, for calculations of the RLM using a time-dependent phase as described in Sec. 2.3.5 and the reference calculation using a RLM including a quench as described in 2.3.2. In all cases, exact diagonalization was used for a system of system size of $M = 50$ sites, voltage $V_{\mathrm{SD}} = 0.5J$, coupling $J_c = 0.3J$ between probe and leads and timesteps Δt. The RLM with time-dependent phase was implemented via the Magnus expansion.

the probe as a voltage quench induces. This allows for a comparison between a fully time-dependent current calculation for the RLM including a time-dependent phase and a standard current calculation using voltage quenches. In both cases exact diagonalization has been used. The results are shown in Figs. 5.1 and 5.2. The approximations work especially well in regions where the current takes a constant value. This is very fortunate, since the main results of this work's simulations are the plateau values of currents. Also, the first order approximation is already a very good guess towards the current for the timesteps usually used in the simulations.

In regions where $f(t)$ is analytic, i.e. not at the borders of the theta functions, the $\hat{\Omega}_k$ are odd functions in Δt when written in a Taylor series around

$$t_{\mathrm{mean}} = t_0 + \frac{\Delta t}{2}. \tag{5.21}$$

As a consequence, since the lowest contribution to $\hat{\Omega}_k$ is of order $\mathcal{O}((\Delta t)^{k+1})$, the lowest contribution to $\hat{\Omega}_{2k+1}$ is of order $\mathcal{O}((\Delta t)^{2k+3})$. The terms $\hat{\Omega}_k$ in the approximation are chosen such that $\sum_{l=1}^{k} \hat{\Omega}_l - \hat{\Omega} = \mathcal{O}((\Delta t)^{k+1})$, e.g. the terms of first order are chosen such that deviations of the full series are at least of the second order in Δt. The two points combined ensure that the

(a) $J\Delta t = 0.25\hbar$ (b) $J\Delta t = 0.5\hbar$
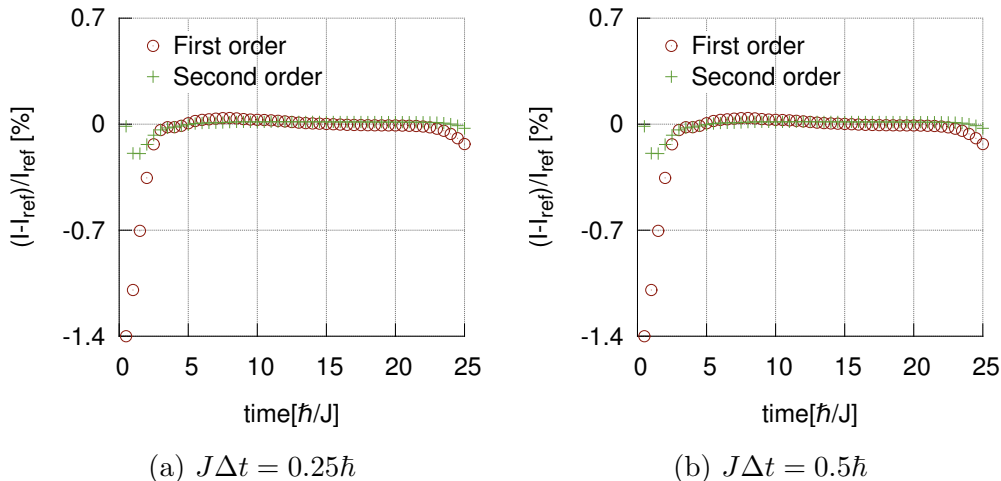
Figure 5.2: Relative differences of currents obtained via the Magnus expansion up to different orders in $\mathcal{O}(\exp J_c \Delta t)$ compared to currents obtained from time-independent current calculations in the RLM. Parameters used are given in the caption of Fig. 5.1.

expansion up to order $\hat{\Omega}_{2k}$ already has to determine the full series up to $(\Delta t)^{2k+3}$ and therefore the $\sum_{l=1}^{2k} \hat{\Omega}_l - \hat{\Omega} = \mathcal{O}((\Delta t)^{2k+3})$. This was found in Ref. [91, 92]. Therefore an inclusion of the next order in the series will not improve the margin of error by an order in Δt and the result is basically a third order result.

5.5 Adiabatic voltage switching

A sudden quench in the voltage leads to a current peak and ringing (oscillations) of the current in the transient regime. From Ref. [13] it is known that the transient effects remain prominent in the thermodynamic limit $M \to \infty$. An increase in the system size therefore cannot suppress them. Implementation of the Magnus expansion allows the simulation of other protocols that generate currents, and that diminish the current peak. In this section different ways to apply a bias to the system during time evolution are investigated and their effects on the current are compared. The goal is a reduction of transient regime effects in order to improve the good quality of the approximation that will be discussed in chapter 6, which will yield quasi-steady states.

The terms contributing to the time evolution Hamiltonian are in all cases discussed in this section the RLM Hamiltonian $\hat{\mathcal{H}}$ defined in Eq. (2.7) and

the voltage term $\hat{\mathcal{H}}_V$ defined in Eq. (2.15). The time evolution Hamiltonian then reads

$$\hat{\mathcal{H}}_t = \hat{\mathcal{H}} + f(t)\,\hat{\mathcal{H}}_V, \tag{5.22}$$

and the operator $\hat{A}(t)$ from Eq. (5.1) is given by

$$\hat{A}(t) = -\frac{i}{\hbar}\left(\hat{\mathcal{H}} + f(t)\,\hat{\mathcal{H}}_V\right). \tag{5.23}$$

First, a linear increase over a timespan τ is studied,

$$f(t) = \frac{t}{\tau}\Theta(\tau - t)\,\Theta(t) + \Theta(t - \tau). \tag{5.24}$$

The problem is solved via Eqs. (5.2), (5.3) and (5.4). The first order expansion in the exponential of the time evolution from $t = t_0$ to $t = t_0 + \Delta t$ then reads

$$
\begin{aligned}
\hat{\Omega}_1\left(t_0 + \Delta t, t_0\right) &= \int_{t_0}^{t_0+\Delta t} \mathrm{d}t'\,\hat{A}(t') \\
&= -\frac{i}{\hbar}\int_{t_0}^{t_0+\Delta t} \mathrm{d}t'\left(\hat{\mathcal{H}} + f(t')\,\hat{\mathcal{H}}_V\right) \\
&= -\frac{i}{\hbar}\left(\hat{\mathcal{H}}\Delta t + \hat{\mathcal{H}}_V\int_{t_0}^{t_0+\Delta t} \mathrm{d}t'f(t')\right) \\
&= -\frac{i}{\hbar}\Delta t\left(\hat{\mathcal{H}} + \hat{\mathcal{H}}_V\left(\Theta(\tau - t_0 - \epsilon)\,\Theta(t_0 + \epsilon)\frac{1}{2\tau}(2t_0 + \Delta t)\right.\right. \\
&\qquad\left.\left.+\Theta(t_0 + \epsilon - \tau)\right)\right) \\
&= -\frac{i}{\hbar}\Delta t\left(\hat{\mathcal{H}} + \hat{\mathcal{H}}_V\left(\Theta(\tau - t_{\mathrm{mean}})\,\Theta(t_{\mathrm{mean}})\frac{t_{\mathrm{mean}}}{\tau}\right.\right. \\
&\qquad\left.\left.+\Theta(t_{\mathrm{mean}} - \tau)\right)\right), \tag{5.25} \\
t_{\mathrm{mean}} &= t_0 + \frac{\Delta t}{2}, \tag{5.26}
\end{aligned}
$$

where ϵ is a small positive number. In this expression the fact that time is dicretized in the numerical evaluation and therefore τ is either outside or at one of the borders of the integration was used,

$$\tau \in\,]-\infty, t_0] \cup [t_0 + \Delta t, \infty[. \tag{5.27}$$

The result in Eq. (5.25) is an example of the statement that only linear terms contribute to the Taylor expansion around t_{mean} in the analytic regions of

$f(t)$. The second order term reads

$$\hat{\Omega}_2\left(t_0 + \Delta t, t_0\right) = \int_{t_0}^{t_0+\Delta t} \mathrm{d}t' \int_{t_0}^{t'} \mathrm{d}t'' \left[\hat{A}\left(t''\right), \hat{A}\left(t'\right)\right]_-$$

$$= \left(-\frac{i}{\hbar}\right)^2 \left[\hat{\mathcal{H}}, \hat{\mathcal{H}}_\mathrm{V}\right]_- \int_{t_0}^{t_0+\Delta t} \mathrm{d}t' \int_{t_0}^{t'} \mathrm{d}t'' \left(f\left(t''\right) - f\left(t'\right)\right)$$

$$= -\left(-\frac{i}{\hbar}\right)^2 \left[\hat{\mathcal{H}}, \hat{\mathcal{H}}_\mathrm{V}\right]_- \frac{\Delta t^3}{6\tau} \times$$

$$\times \Theta\left(\tau - t_\mathrm{mean}\right)\Theta\left(t_\mathrm{mean}\right). \tag{5.28}$$

The commutator reduces to

$$\left[\hat{\mathcal{H}}, \hat{\mathcal{H}}_\mathrm{V}\right]_- = \frac{V_\mathrm{SD}}{2} J_c \left(\left[\hat{c}_{-1}^\dagger \hat{c}_0 + \mathrm{h.c.}, \hat{c}_{-1}^\dagger \hat{c}_{-1}\right]_-\right.$$

$$\left. - \left[\hat{c}_1^\dagger \hat{c}_0 + \mathrm{h.c.}, \hat{c}_1^\dagger \hat{c}_1\right]_-\right),$$

$$= 2i \frac{e V_\mathrm{SD}}{2} J_c \hat{C}, \tag{5.29}$$

where the last line defines the dimensionless and hermitian operator $\hat{C}$. Using the commutator relations of Eq. (2.13) leads to

$$\hat{C} = -\frac{i}{2}\left(\hat{c}_0^\dagger \hat{c}_{-1} - \hat{c}_{-1}^\dagger \hat{c}_0 - \hat{c}_0^\dagger \hat{c}_1 + \hat{c}_1^\dagger \hat{c}_0\right)$$

$$\left\langle \hat{C} \right\rangle = \mathrm{Im}\left\{\left\langle \hat{c}_0^\dagger \hat{c}_{-1} + \hat{c}_1^\dagger \hat{c}_0 \right\rangle\right\}, \tag{5.30}$$

$$\hat{\Omega}_2\left(t_0 + \Delta t, t_0\right) = -\frac{i}{\hbar}\Delta t \frac{e V_\mathrm{SD} J_c \Delta t^2}{6\tau\hbar} \Theta\left(\tau - t_\mathrm{mean}\right)\Theta\left(t_\mathrm{mean}\right)\hat{C}. \tag{5.31}$$

The resulting current at the different orders is compared in Fig. 5.3. As in Fig. 5.1, the error correction by $\hat{\Omega}_2$ is negligible. The maximum value of the dimensionless coefficient $a_2(t_0, t_0 + \Delta t)$ in

$$\hat{\Omega}_1\left(t_0 + \Delta t, t_0\right) = -\frac{i}{\hbar}\Delta t\left(\hat{\mathcal{H}} + a_1\left(t_0, t_0 + \Delta t\right)\hat{\mathcal{H}}_\mathrm{V}\right),$$

$$\hat{\Omega}_2\left(t_0 + \Delta t, t_0\right) = -\frac{i}{\hbar}\Delta t^2 \frac{eV}{\hbar} J_c a_2\left(t_0, t_0 + \Delta t\right)\hat{C} \tag{5.32}$$

for the chosen parameters is 2.8×10^{-3}, while $a_1(t_0, t_0 + \Delta t)$ tends towards one. Comparison of the behavior of the transient current in Fig. 5.4 illustrates that a slower increase in voltage reduces the size of the transient peak but does not influence the oscillations superposing the steady state.
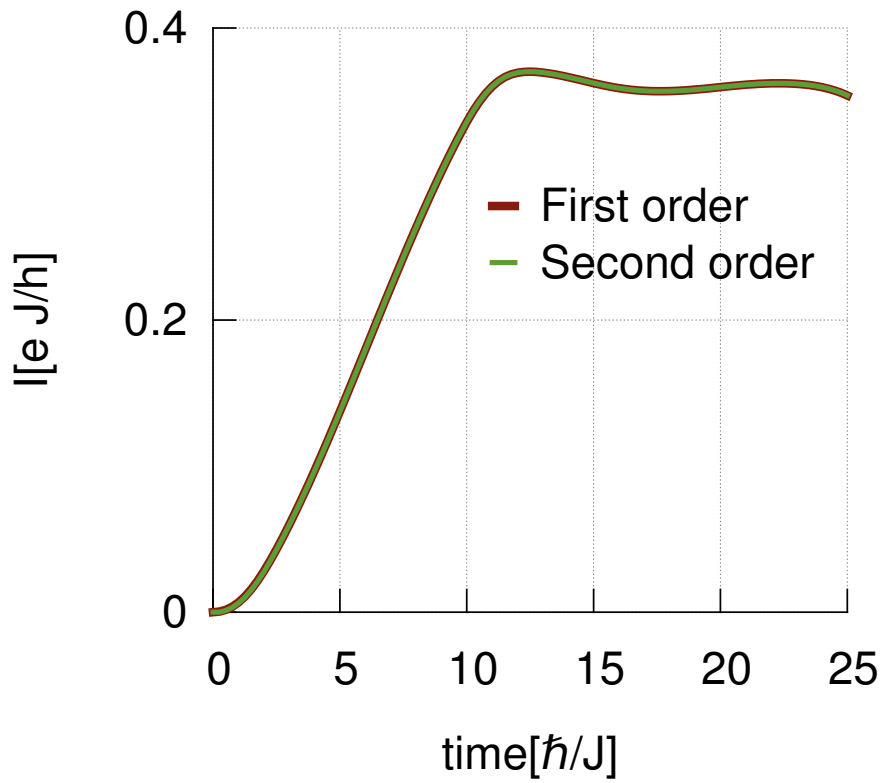
Figure 5.3: Comparison of first and second order current for a linear increase in voltage over a timespan of $\tau J = 10\hbar$. The system has a size of $M = 50$ sites, tunneling element $J_c = 0.3J$, maximal voltage $eV_{\text{SD}} = 0.5J$ and timestep size $J\Delta t = 0.25\hbar$.
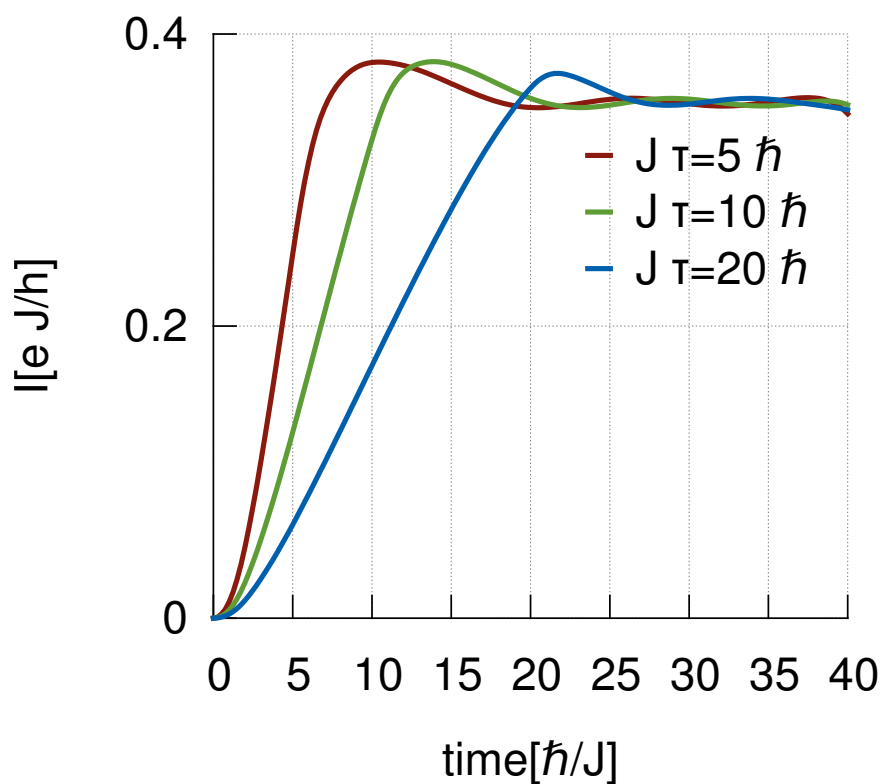
Figure 5.4: Comparison of first order currents for a linear increase in voltage over different timespans τ. The system has a size of $M = 80$ sites, tunneling element $J_c = 0.3J$, maximal voltage $eV_{\text{SD}} = 0.5J$ and timestep size $J\Delta t = 0.25\hbar$.

The function $f(t)$ that was used so far is not analytic and has kinks. In order to find out whether the choice of a smoother $f(t)$ can improve the passage to the steady state, an increase with

$$f(t) = \sin\left(\frac{\pi}{2}\frac{t}{\tau}\right)^2 \Theta(\tau - t)\Theta(t) + \Theta(t - \tau) \qquad (5.33)$$

is investigated. As a result the coefficients defined in equation (5.32) read

$$a_1\left(t_{\text{mean}} - \frac{\Delta t}{2}, t_{\text{mean}} + \frac{\Delta t}{2}\right) = \int_{t_{\text{mean}}-\frac{\Delta t}{2}}^{t_{\text{mean}}+\frac{\Delta t}{2}} \frac{\mathrm{d}t'}{\Delta t} f(t')$$

$$= \left(\frac{1}{2} - \frac{\tau}{\pi}\cos\left(\frac{\pi}{\tau}t_{\text{mean}}\right)\frac{\sin\left(\frac{\pi}{2\tau}\Delta t\right)}{\Delta t}\right) \times$$

$$\times \Theta(\tau - t_{\text{mean}})\Theta(t_{\text{mean}})$$

$$+ \Theta(t_{\text{mean}} - \tau), \qquad (5.34)$$

$$a_2\left(t_{\text{mean}} - \frac{\Delta t}{2}, t_{\text{mean}} + \frac{\Delta t}{2}\right) = \int_{t_{\text{mean}}-\frac{\Delta t}{2}}^{t_{\text{mean}}+\frac{\Delta t}{2}} \frac{\mathrm{d}t'}{\Delta t}\int_{t_{\text{mean}}-\frac{\Delta t}{2}}^{t'} \frac{\mathrm{d}t''}{\Delta t}\left(f(t'') - f(t')\right)$$

$$= \frac{\tau}{\pi^2 \Delta t}\sin\left(\frac{\pi}{\tau}t_{\text{mean}}\right) \times$$

$$\times \left\{\pi\cos\left(\frac{\pi}{\tau}\frac{\Delta t}{2}\right) - 2\frac{\tau}{\Delta t}\sin\left(\frac{\pi}{\tau}\frac{\Delta t}{2}\right)\right\}$$

$$\times \Theta(\tau - t_{\text{mean}})\Theta(t_{\text{mean}}). \qquad (5.35)$$

Again, the change in current due to the inclusion of $\hat{\Omega}_2$ is marginal, according to Fig. 5.5. The comparison of currents for the two different adiabatic increases of voltage done in Figs. 5.6, 5.7 and 5.8 results in the insight that the choice of a specific shape of voltage increase has only a minor influence on the height of the current peak in the transient regime. The best possibility of a reduction of this peak is an increase of τ.

5.6 Applications and outlook

The combination of td-DMRG and time-dependent exponential perturbation theory allows for a wealth of new systems to be studied. Alternating voltages can be simulated, allowing for an investigation of the interaction of systems with external photons. Other time-dependent manipulations of the systems can also be simulated. An example would be the simulation of qubit operations on quantum dot realizations of qubits in the case that a modeling of the surrounding bath is available or neglected.
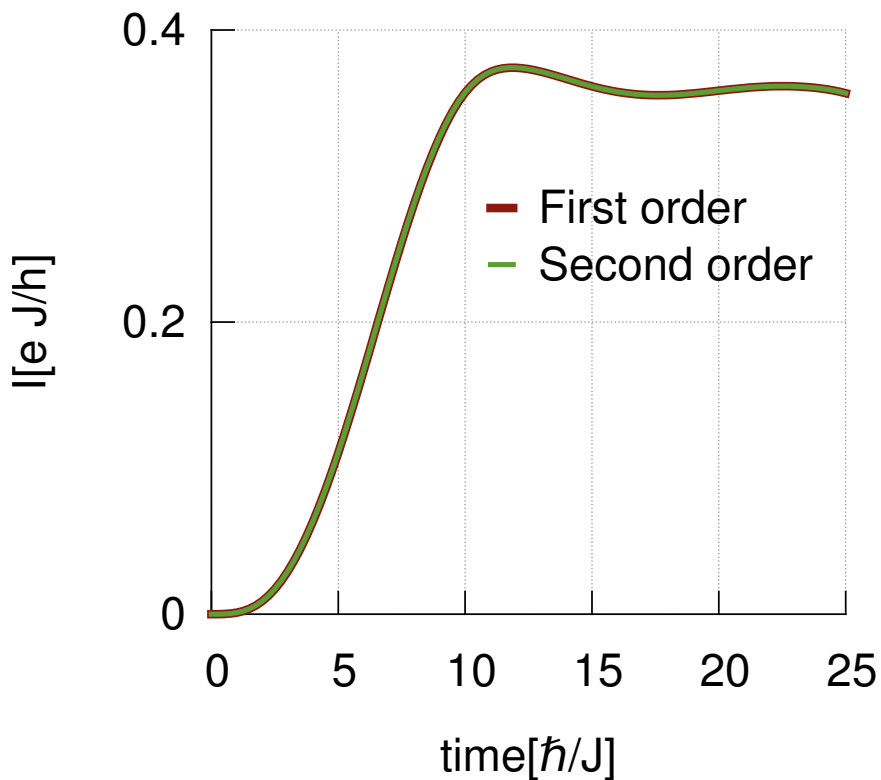
Figure 5.5: Comparison of first and second order current for a smoother increase in voltage over a timespan of $\tau J = 10\hbar$. The system has a size of $M = 50$ sites, tunneling element $J_c = 0.3J$, maximal voltage $eV_{\text{SD}} = 0.5J$ and timestep size $J\Delta t = 0.25\hbar$.

Figure 5.6: Comparison of currents for linear and smoother increase in voltage over a timespan of $\tau J = 5\hbar$. The system has a size of $M = 80$ sites, tunneling element $J_c = 0.3J$, maximal voltage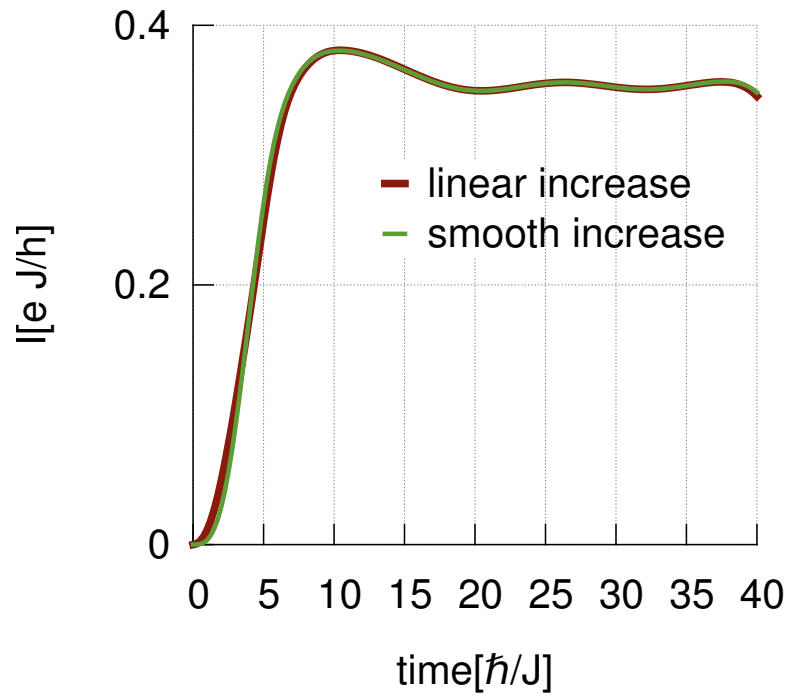 $eV_{SD} = 0.5J$ and timestep size $J\Delta t = 0.25\hbar$. Currents were simulated using the first order Magnus expansion.
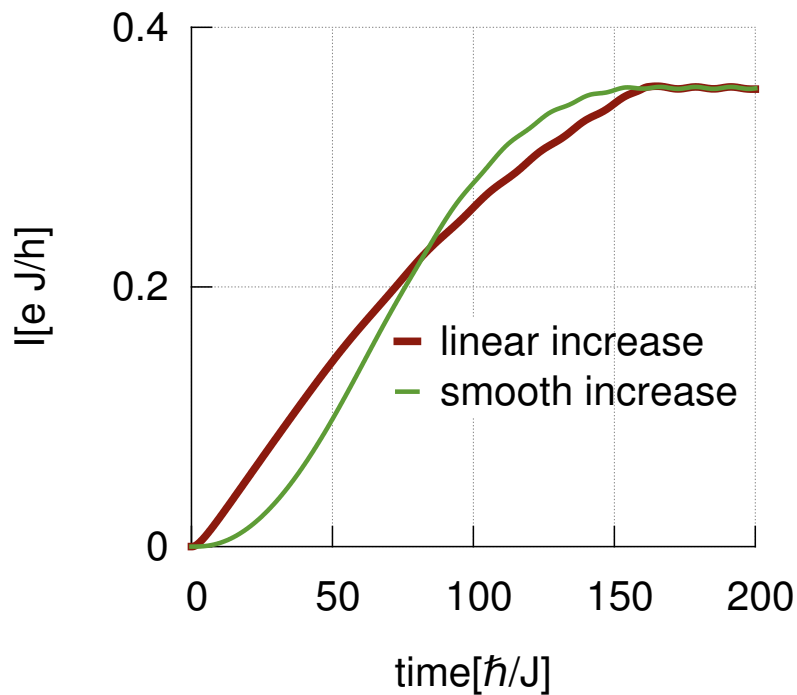
Figure 5.7: Comparison of currents for linear and smoother increase in voltage over a timespan of $\tau J = 160\hbar$. The system has a size of $M = 400$ sites, tunneling element $J_c = 0.3J$, maximal voltage $eV_{\mathrm{SD}} = 0.5J$ and timestep size $J\Delta t = 0.25\hbar$. Currents were simulated using the first order Magnus expansion.

M [1]	$\tau \left[\frac{\hbar}{J}\right]$	$I_{\text{smooth}} \left[\frac{eJ}{h}\right]$	$I_{\text{lin}} \left[\frac{eJ}{h}\right]$
80	5	0.381	0.381
80	10	0.381	0.381
80	20	0.377	0.373
200	30	0.360	0.359
200	50	0.357	0.358
200	70	0.356	0.358
400	100	–	0.355

Figure 5.8: Comparison of current peaks I_{lin} and I_{smooth} in the transient regime for linear and smoother increase in voltage over different timespans τ and in different system sizes M. The systems have tunneling element $J_c = 0.3J$, maximal voltage $eV_{\text{SD}} = 0.5J$ and timestep size $J\Delta t = 0.25\hbar$. Currents were simulated using the first order Magnus expansion. For $\tau J = 130\hbar$ and $\tau J = 160\hbar$ no peaks are observed in the transient regime, see Fig. 5.7. For $\tau J = 100\hbar$, only the setup with linear increase in voltage shows a peak in the transient regime. The steady state current resulting from analytic calculations for the chosen parameters is $Ih = 0.355eJ$.

The RLM containing a current source served here as a validation of the use of time-dependent exponential perturbation theory in the DMRG. but it was also investigated with another application in mind. The reflection of particles at the boundaries of the system connects the timespan available for current extraction to the system size. To decouple timespan from system size, absorbing boundary conditions could be introduced at the borders of the leads. However a lead which absorbs particles is a bad particle source, so in this case a current source in the center of the system would be prefered. So far no absorbing boundaries have been implemented successfully either due to reflections at the absorbing layer [93, 28, 94] or due to other unwanted effects [95]. In the scope of this work, no local absorption proved successful and a global energetic damping in the system leading to steady states will be presented in chapter 6. An introduction of current sources therefore is not needed in the end. Modification of the steady state to a closer resemblance of the thermodynamic steady state is one of the reasons to adiabatic voltage increases. It was shown in the previous section that the first order approximation of the Magnus row sufficiently reproduces the full time evolution. Work in that direction ultimately proved to be not successful.

Chapter 6

Towards steady state current simulations on finite systems

In the simulations performed in chapter 4, quasi steady state currents are only observed up to a finite time scale. This is a common problem for numerics which simulate finite systems out of equilibrium evolving in time. For a one-dimensional problem, interferences will occur in the center of the system after a return time τ_{r} given by $v_F \tau_{\mathrm{r}} = M$, where v_F is the Fermi velocity of the particles and M is the length of the system, as has been discussed in Sec. 2.3.3. The interferences carry information about the boundaries of the system, which distinguishes the simulated system from the larger systems realized in experiment and from systems in the thermodynamic limit assumed in analytic calculations. Simulated currents thus cease to mimic experimentally observed currents or analytically calculated currents once excitations return from the boundaries of the system. Thus the finite size of the system limits the measurement time during simulation and, as a result, adds finite time effects to the obtained current [96]. So far, efforts to overcome this limitation of the simulation methods have included smooth [93] and damped [28] boundary conditions, among other things. Also integrable impurities [94] and baths acting as source and drain attached in a one-directional way to the leads [95] have been tested. Some of these attempts delay the emergence of interferences, but none reduce them, see for example Ref. [57]. Within other areas of research, the problem is solved by using absorbing boundary conditions. Examples include photonic transport calculations in a single particle picture [97] or energy resolved Green's function approaches to the extraction of transport properties using density functiontal theory [98, 99]. This approach fails when applied to time resolved simulations of particle conserving

fermionic systems due to an unphysical long-range interaction generated by
the normalization of the wave functions [100]. An example of this failure
even for a noninteracting system when considering a single particle picture
as described in Sec. 3.1 is given in Sec. 6.4. In order to introduce damped
boundaries to many particle wave functions in a mathematically correct way
a DMRG method based on a density matrix description of the system is
needed. As a reminder the DMRG procedures explained in Sec. 3.2 are based
on many particle wavefunctions describing pure states. The density matrix
based DMRG method would need as its basis the space of all the possible
density matrices. This is a very resource demanding requirement [101] and
is therefore not suitable for the transport calculations targeted in this work.
The current chapter contains the study of a less rigorous and less resource
costly method to simulate steady states.

Section 6.1 again highlights the restriction on numerical transport sim-
ulations on finite systems. The main idea of the method, namely to use
the nonhermiticity of the hamiltonian to generate energetic damping, is pre-
sented in Sec. 6.2. The method then is tested on the RLM in Sec. 6.3. The
obtained steady state currents are compared to the known analytic steady
state currents of the RLM, and the outcome is discussed. Section 6.5 sum-
marizes the results of this chapter. Calculations in this chapter have been
performed using the DMRG algorithms discussed in chapter 3 unless stated
otherwise.

6.1 Restrictions on numerical current simulation in finite systems

In Sec. 2.3.2 two different prescriptions to quench the system have been dis-
cussed. Within this chapter the focus is on the quench to shifted energy bands
sketched in Fig. 2.6b. The quench is realized by the addition of the voltage
term given in Eq. (2.15) to the time evolution hamiltonian $\hat{\mathcal{H}}_t$. Fig. 6.1 shows
the resulting time evolution of the particle density per site in a simulation
for the RLM. The RLM is defined in Sec. 2.2, and its Hamiltonian is given in
Eq. (2.7) with $V_g = 0$. A density wave travels towards the boundaries, gets
reflected and returns to the center of the system, as discussed earlier. The
return time is given by

$$
\begin{aligned}
t_r &= \frac{M}{v_F} \\
&= \frac{M}{2} \frac{\hbar}{J},
\end{aligned} \tag{6.1}
$$

where M is the system size and the last equation holds true for filling up to crystal momentum $\pi/2$ with Fermi velocity $\hbar v_F = 2J$. In this simulation a transient current is observed, see Fig. 6.3, which decays exponentially with a decay time of

$$t_d = \frac{\hbar J}{2J_c^2} \tag{6.2}$$

in which the transient current reduces to a fraction of e^{-1} of its original value. After this time the steady state contribution to the current becomes dominant, but is still superposed by an oscillatory term with oscillation period of

$$T = \frac{2\pi\hbar}{eV_{\mathrm{SD}}}. \tag{6.3}$$

Fig. 6.2 visualizes the oscillation as well as the interference. The steady state current can be separated from the superposed oscillation if $T \lesssim t_r - t_d$. For small voltages V_{SD} or small couplings J_c between lead and structure the system size M needs to be large for this requirement to hold. In order to obtain low margins of error from the DMRG, the number of basis states kept after the DMRG reduction of the Hilbert space needs to be increased with increasing system size. Similar statements hold true for other numerical procedures. In general, a larger system size means higher cost of computational resources. This limits the parameter ranges of applicable voltages and system parameters for numerical investigations of systems. The method presented in the next section targets to overcome this limitation.

For an additional point of view on this motivation the correspondence between currents generated by a voltage source and currents generated by a current source is required. A derivation of the fact that both sources produce the same current in the RLM is given in Sec. 2.3.5. If the current is generated by a current source in the center of the system, the source and the drain in form of the leads are spacially separated. However in finite systems the leads do not act as drains in the sense that they remove incoming particles from the measurement. The functionality of a drain has to be added, e.g. by absorption in the leads. Simply adding absorbing reservoirs to the leads does not produce the desired results for the reasons discussed in Ref. [100] and, briefly, in the next section. In the next section an energetic damping is proposed that is active in the whole system and simulates an environment of the system. It is realized by the use of nonhermitian Hamiltonians, or put in an alternative picture, by the use of complex timesteps.
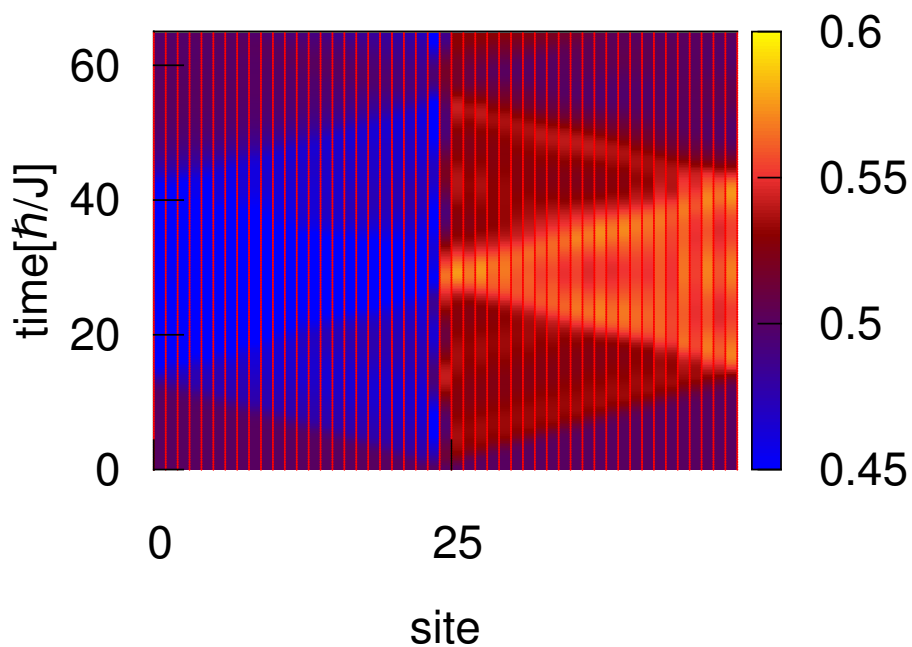
Figure 6.1: Color encoded density distribution over site and time in the RLM after quench as described in Sec. 6.1. Starting from uniform density at $t = 0$, particles initially move to the right. The first particles get reflected at $Jt = 12.5\hbar$ and return to the system again at $Jt = 25\hbar$. Parameters are $M = 50$, $eV_{\mathrm{SD}} = 0.5J$, $J\Delta t = 0.25\hbar$ and $J_c = 0.3J$.
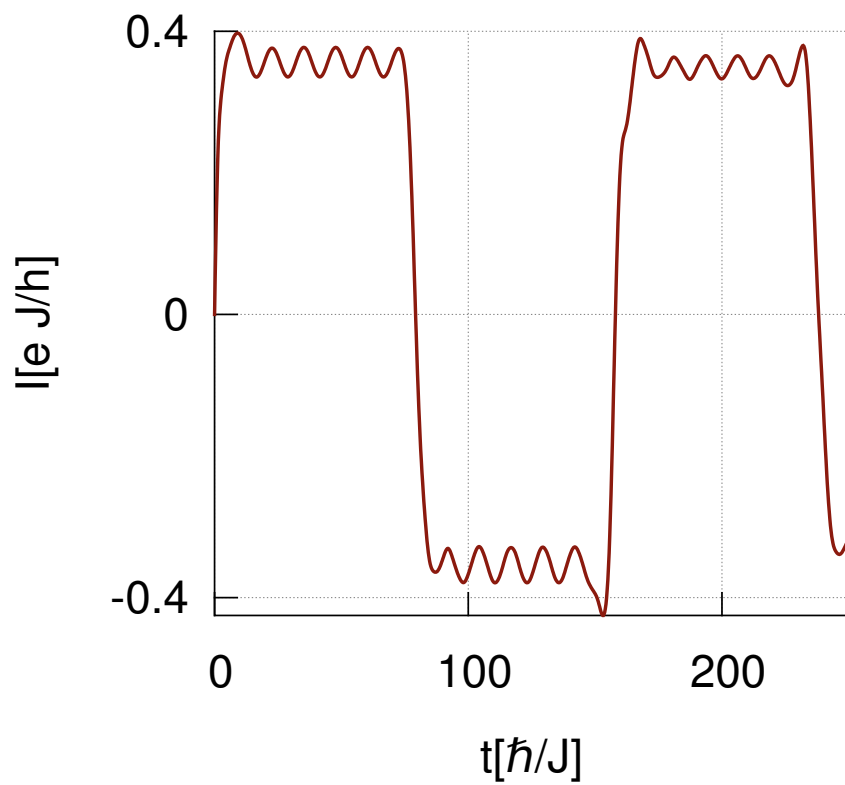
Figure 6.2: Current over time calculated numerically in the RLM via exact diagonalization. Parameters are $M = 150$, $eV_{SD} = 0.5J$, $J_c = 0.3J$ and timesteps $J\Delta t = 0.25\hbar$.
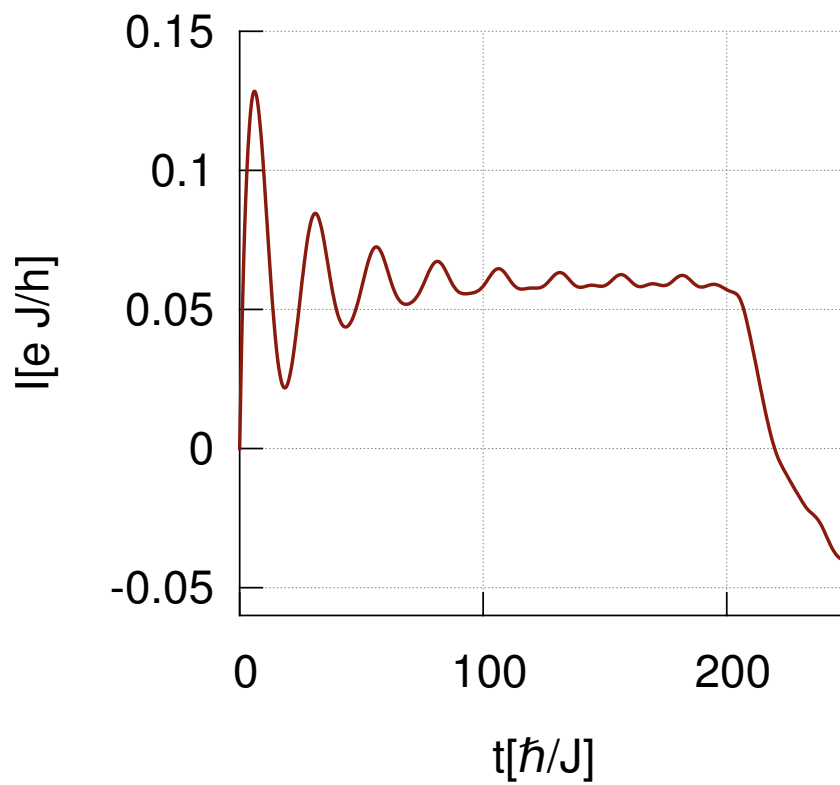
Figure 6.3: Current over time calculated numerically in the RLM via exact diagonalization. Parameters are $M = 400$, $eV_{\mathrm{SD}} = 0.5J$ and $J_c = 0.1J$ and timesteps $J\Delta t = 0.25\hbar$.

6.2 Method

In statistical physics, instead of an explicit inclusion of baths into the description of a system, their effect is occasionally regarded by addition of antihermitian terms to the self energy of the system in a Green's function formulation [60] of the problem [102, 99]. As a short reminder, the Green's function $G(x, x', E)$ of a one-dimensional system without interaction containing only one particle is defined as the solution of the equation [103]

$$(E - H_0(x)) G(x, x', E) = \delta(x - x').$$ (6.4)

The Dirac delta distribution is denoted by $\delta(x)$ and $H_0(x)$ describes the interactionless system. This equation is formally solved by the retarded Green's function

$$G^R(x, x', E) = \frac{1}{E - H_0(x) + i0^+}.$$ (6.5)

In momentum space, with E_p being the eigenfunctions of the Hamiltonian $\hat{\mathcal{H}}_0$ of the system, the solution reads [60]

$$G^R(p, E) = \frac{1}{E - E_p + i0^+}.$$ (6.6)

The concept of Green's functions also exists for interacting many particle systems with Hamiltonian $\hat{\mathcal{H}}_0 + \hat{\mathcal{H}}_I$ where the interactions are described by $\hat{\mathcal{H}}_I$. There, the formal solution reads

$$G^R(p, E) = \frac{1}{E - E_p + i0^+ - \Sigma(p, E)},$$ (6.7)

and the self energy $\Sigma(p, E)$ incorporates the effects of $\hat{\mathcal{H}}_I$. Interactions included in $\hat{\mathcal{H}}_I$ usually affect the real and imaginary part of $\Sigma(p, E)$. The addition of an antihermitian term to the Hamiltonian which does not explicitly include interactions is a simple way to mimic the ad-hoc addition of only an imaginary part to $\Sigma(p, E)$. This happens on the level of the definition of Hamiltonians and is thus independent of the language of Green's functions.

A noninteracting term in the Hamiltonian which varies in space, as would be the case for absorbing terms added to the ends of the leads, will lead to an additional source of wave reflection. This is due to the correspondence of a change in hopping elements to the physical phenomena investigated e.g. in the RLM. The reflected current is equal to $e^2 V_{SD}/h$ minus the transmitted current and is different from zero in the RLM case for $J_c \neq J$, as seen from

Eq. (2.29). In order to overcome the reflections, the proposal introduces a global antihermitian term which is constant in the leads to the Hamiltonian leading to a mixed real and imaginary time evolution. The antihermitian term is chosen to share the same eigenstates and the same hierarchy of eigenenergies with the initial Hamiltonian. This choice yields a projection to the initial state by the imaginary time evolution operator.

In the procedure picked in Sec. 6.1 for this chapter and described in Sec. 2.3.2 time evolution is governed by the Hamiltonian $\hat{\mathcal{H}}_{\mathrm{t}} = \hat{\mathcal{H}}_{\mathrm{s}} + \hat{\mathcal{H}}_{\mathrm{V}}$, with $\hat{\mathcal{H}}_{\mathrm{V}}$ given in Eq. (2.15). The proposal now replaces $\hat{\mathcal{H}}_{\mathrm{s}}$ by the nonhermitian Hamiltonian

$$
\begin{aligned}
\hat{\mathcal{H}}' &= \exp\left(-i\Phi\right)\hat{\mathcal{H}}_{\mathrm{s}} \\
&= \cos\left(\Phi\right)\hat{\mathcal{H}}_{\mathrm{s}} - i\sin\left(\Phi\right)\hat{\mathcal{H}}_{\mathrm{s}} \\
&= \cos\left(\Phi\right)\hat{\mathcal{H}}_{\mathrm{s}} + \sin\left(\Phi\right)\hat{\mathcal{A}},
\end{aligned} \tag{6.8}
$$

with $\hat{\mathcal{H}}_{\mathrm{s}}$ being hermitian, e.g. the Hamiltonian written down in Eq. (2.7), and $\hat{\mathcal{A}} = -i\hat{\mathcal{H}}_{\mathrm{s}}$. The phase $\Phi \in [0, \pi/2]$ is chosen as an arbitrary phase that dictates the strength of the energetic damping. Its influence on the result is discussed in Sec. 6.3. The operator $\hat{\mathcal{H}}'$ conserves the particle number if $\hat{\mathcal{H}}_{\mathrm{s}}$ does, as is the case in considerations within the scope of this thesis. $\hat{\mathcal{A}}$ has the same eigenfunctions as $\hat{\mathcal{H}}_{\mathrm{s}}$. The eigenenergies $E_n^{\hat{\mathcal{H}}_{\mathrm{s}}}$ of $\hat{\mathcal{H}}_{\mathrm{s}}$ are real since $\hat{\mathcal{H}}_{\mathrm{s}}$ is hermitian, so the eigenenergies $E_n^{\hat{\mathcal{A}}}$ of $\hat{\mathcal{A}}$ are imaginary, with

$$
E_n^{\hat{\mathcal{A}}} = -iE_n^{\hat{\mathcal{H}}_{\mathrm{s}}}. \tag{6.9}
$$

In td-DMRG the state of the system $|\Psi(t)\rangle$ is evolved in time with timesteps Δt as

$$
|\widetilde{\Psi}(t + \Delta t)\rangle = \exp(-i\hat{\mathcal{H}}'\Delta t)\,|\Psi(t)\rangle \tag{6.10}
$$

$$
|\Psi(t + \Delta t)\rangle = |\widetilde{\Psi}(t + \Delta t)\rangle / \sqrt{\langle\widetilde{\Psi}(t + \Delta t)\,|\,\widetilde{\Psi}(t + \Delta t)\rangle}. \tag{6.11}
$$

Expressing $|\Psi(t)\rangle$ in terms of eigenstates $|\Psi_n\rangle$ of $\hat{\mathcal{H}}_{\mathrm{s}}$ and assumption of small $J\Delta t \ll \hbar$ yields

$$
|\widetilde{\Psi}(t + \Delta t)\rangle = \sum_n c_n(t)\exp(-i\sin\left(\Phi\right)E_n^{\hat{\mathcal{H}}_{\mathrm{s}}}\Delta t)\,\exp(-\cos\left(\Phi\right)E_n^{\hat{\mathcal{H}}_{\mathrm{s}}}\Delta t)\,|\Psi_n\rangle. \tag{6.12}
$$

The coefficients $c_n(t)$ which give the weight of the eigenfunctions $|\Psi_n\rangle$ in the state of the system therefore aquire an exponential damping factor of $\exp(-\cos\left(\Phi\right)E_n^{\hat{\mathcal{H}}_{\mathrm{s}}}\Delta t)$, which depends on their corresponding eigenenergies.

By definition the initial state $|\Psi_0\rangle$ of the system has the lowest eigenenergy. The coefficients of other eigenstates are suppressed relative to $c_0(t)$ since they aquire stronger damping factors. In that sense $\hat{\mathcal{A}}$ enhances the contribution from the initial state during time evolution, or put differently, the resulting state is closer to the initial state due to $\hat{\mathcal{A}}$. On the other hand states containing excitations have higher energies than the ground state. $\hat{\mathcal{A}}$ reduces the relevance of contributions from these states during time evolution. Excitations correspond to moving particles, and since the excitations are created in the center of the system the particles initially move towards the boundaries. This means that states containing particles which move towards the boundaries of the system become less relevant over time. As a result the wavefronts moving towards the edges of the system shrink over time. Fig. 6.4 shows the effect of $\hat{\mathcal{A}}$ on the current at different positions in the system and the reduction in net particle flow towards the boundaries. The time averaging for this figure was performed over the time range in which the system is in a (quasi-)steady state, i.e. starting from the time when the transient current has decayed up to the time at which the simulation ends.

As stated before, particle conservation still holds in the presented prescription for the RLM. The shrinking wavefronts are part of a non-local change in density. This unphysical effect does not obey causality and is caused by the normalization of the wavefunction, see Eq. (6.11). It can actually increase the contribution of eigenstates and therefore the local density at some positions. A more detailed discussion of the effect is given in Ref. [100]. The time evolution contains a competition between $\hat{\mathcal{A}}$, which moves the system towards the initial state, and $\hat{\mathcal{H}}_{\mathrm{V}}$, which drives the system away from the initial state. Together the two terms force the system into a (quasi-)steady state. The error of this approximation with respect to the introduction of an unphysical effect is discussed in the next section.

An equivalent description of the method uses the hermitian Hamiltonian $\hat{\mathcal{H}}_{\mathrm{s}}$ and includes the phase in the definition of the parameter time. The new time t' is complex,

$$t' = \exp\left(-i\Phi\right)t. \tag{6.13}$$

This leads to the same mixed time evolution present in Eq. (6.12), which can be separated into real and imaginary time evolution. The imaginary time evolution acts approximately as projection of the state onto the initial state, yielding the energetic damping.

In a finite system, the steady state means that there is no net change of charge within the leads. According to the definition given in Sec. 2.3.1, the current therefore vanishes. Yet there is still a flow of particles through
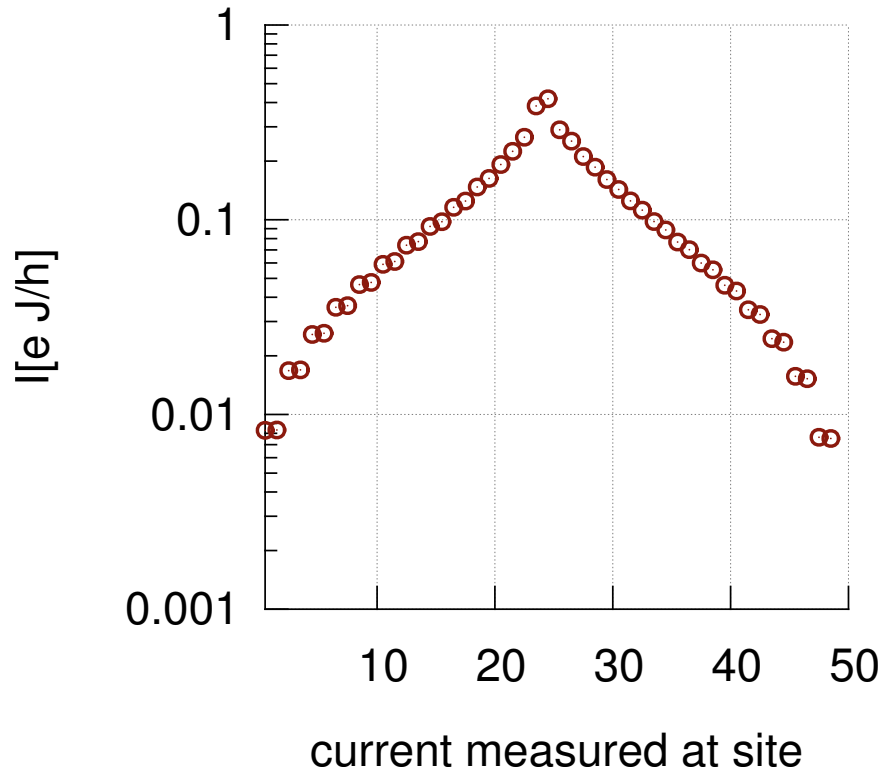
Figure 6.4: Time averaged current over site index for
$\hat{\mathcal{H}}' = \exp\left(-i0.494\pi\right)\hat{\mathcal{H}}_{\mathrm{RLM}}$, with RLM-Hamiltonian $\hat{\mathcal{H}}_{\mathrm{RLM}}$. Parameters are
$M = 50$, $eV_{\mathrm{SD}} = 0.5J$, and $J_c = 0.3J$, and time evolution is discretized with
timesteps $J\Delta t = 0.25\hbar$.

the structure. This flow is compensated by the change of charge due to the damping in the leads. The current for this method is defined as the flow of particles in the absence of damping. It is calculated as expectation value of the operator $-i/\hbar[\hat{\mathcal{H}}_s, \hat{Q}]_-$. This is the expression obtained from the Heisenberg equation of motion for $-\partial_t \hat{Q}$ in a system governed by the hermitian Hamiltonian $\hat{\mathcal{H}}_s$, with $\hat{Q}$ being the charge operator. For each point in time this corresponds to the fictitious situation that at this time of the measurement the damping is turned off, and the system is described again by $\hat{\mathcal{H}}_s + \hat{\mathcal{H}}_V$. To see this one needs to remember that the time evolution up to the current measurement for this meausrement point in time was governed by the system including damping. The current then is calculated from $-i/\hbar[\hat{\mathcal{H}}_s, \hat{Q}]_-$, which means that the system is described by $\hat{\mathcal{H}}_s$ in the near future of that point in time.

6.3   Results

In a first step big phases are considered. The result for one realization of a current measurement simulation in the RLM using nonhermitian time evolution Hamiltonians is shown in Figs. 6.5 and 6.6. The interference which manifests as sudden drop in current is no longer observable due to the strong energetic damping reducing the reflected wave to a neglectable amount. The current shows a transient regime, just as with the methods discussed in Sec. 2.3.2. However, the transient current does not show an exponential decay. The superposed oscillations show a changed behavior since the eigenenergies and therefore the energy gap which causes the oscillations now are complex quantities. The steady state current is extracted by averaging out the superposed oscillations. Simulations for different parameters in the RLM and for different voltages result in the I/V given in Fig. 6.7. As shown in Fig. 6.4 the value of the current changes depending on the position of the extraction in the system. In Fig. 6.7 was extracted at the connection between structure and lead. This means that at the point of measurement between the structure and the first site of the lead, a mean current of

$$\langle \overline{I} \rangle (t) = \int_0^1 dx\, f(x,t)\, \langle I \rangle (t) \tag{6.14}$$

was calculated. Here, the integration goes from the structure $(x = 0)$ to the first site of the lead $(x = 1)$. $f(x,t)$ is the function describing the decay of the current, and $\langle I \rangle (t)$ is the expected current on the structure. The current intended to calculate is obtained from $\langle \overline{I} \rangle (t)$ by inversion of the equation. If this effect is included in the extrapolation of the current flowing in through

the structure in the center of the system, the I/V changes to the curve plotted in Fig. 6.8 . The extrapolation used approximated the damping to be of exponential form, $f(x,t) = \exp\{-\Gamma_x x\}$.

The resulting currents over time show remnants of the interference, which reduce for values of Φ close to $\pi/2$, see Figs. 6.9, 6.10 and 6.11. The suppression of the remnants depends on Φ and J_c, and for small J_c they reduce faster with increasing Φ. A variation of the extracted currents with the phase Φ and the size M is observable. This variation is slow in the region of Φ that shows a strong suppression of the interferences. Fig. 6.12 shows the I/V for currents with strongly differing phases and sizes.

The I/V in Figs. 6.7 and 6.8 contain results obtained with the two different phases $\Phi = 0.494\pi$ and $\Phi = 0.49\pi$, which yield very similar results due to the small difference in phase and the slow variation in that region. The method gives good results even for very low decay rates of up to $\hbar J\Gamma = 2J_c^2 = 2*10^{-4}J^2$ in systems with $M = 50$ sites. This should be compared with the resulting current for $\Phi = 0$ for the same system size in Fig. 6.6. These systems should have an energy resolution of roughly $\Delta E = 4\pi J/M \approx 0.25J$. The mismatch between the shapes of the currents obtained for the two different methods can not be explained by finite size effects, as seen in Fig. 6.12. One possible explanation builds on the observation that the density at the structure oscillates in time, as seen in Fig. 6.13. This hints at an excitation on the resonant level which cannot decay due to the interplay of damping and voltage terms. In simulations not using the phase, the resonance builds up in the transient regime and then decays over time, which leads to the decay rate of the transient current being connected to the resonance width. As a consequence of this, the forced quasi steady state differs from the steady state obtained in the thermodynamic limit or in experiments. Fig. 6.14 shows the current resulting from an adiabatic voltage switch. Adiabatic voltage switches modify the transient behavior and partially prevent the resonant level from being excited, as can be seen by the reduced peak in Fig. 5.8. Since the measurement time is no longer restricted by the return time of a wavefront, the possibility of long switching times τ is given. For the simulation with a phase applied to the Hamiltonian, adiabatic switching does not improve the situation. Another source of error is the extrapolation formula which assumes exponential damping of the current towards the leads. A formula matching the actual damping in a better way might improve the resulting I/V. However, the damping within the leads seems to be rather independent from the coupling to the structure and only weakly dependent on the applied voltage. Assuming exponential damping, the current decay rate per site for $J_c = 0.3J$, $eV_{\mathrm{SD}} = 0.5J$ and $\Phi = 0.494\pi$ equals $\Gamma_x = 0.86/\mathrm{site}$. For $J_c = 0.01J$ and same parameters otherwise, it
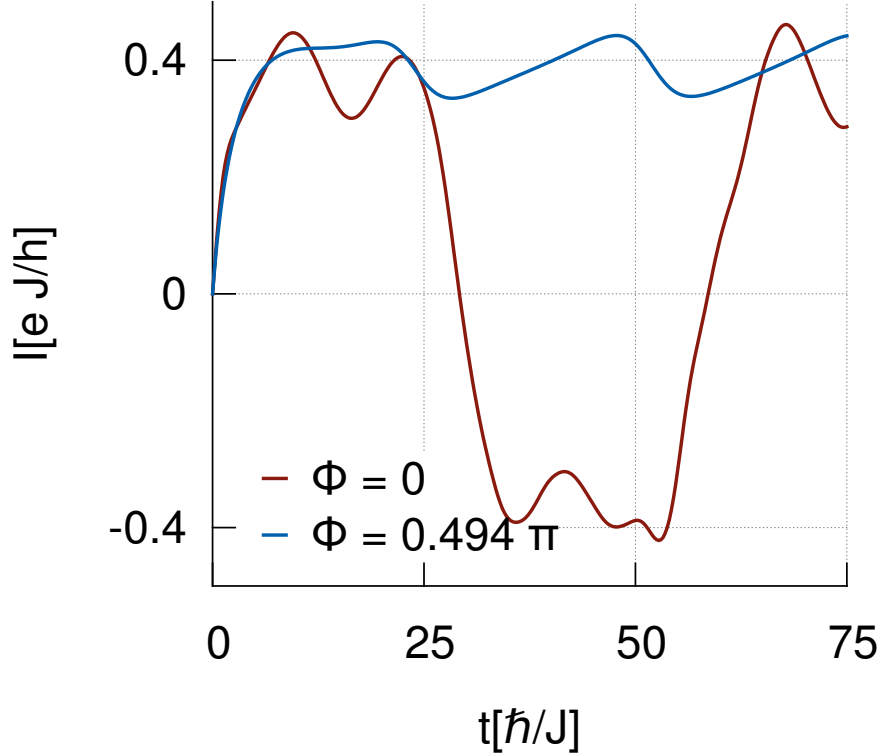
Figure 6.5: Current over time in the noninteracting resonant level model with $M = 50$, $J_c = 0.3J$ and $eV_{\text{SD}} = 0.5J$. The blue line gives the result for the method presented in this chapter. The red line gives the result using the usual method.

also equals $\Gamma_x = 0.86/$site. Most importantly, the damping will not lead to an increase in the current from the structure towards the lead. Errors made in the formula can not explain the overestimation of current for larger values of J_c.

Fig. 6.15 shows the I/V resulting from different values of ϕ and M. The data is chosen from the pool of performed simulations as the simulations using the smallest phases that generate currents without visible remnants of the interferences. This approach is supposed to give the optimal I/V possible since the error introduced by the large phase has not been removed by the proposed treatments. The method gives results which are in accordance with analytic solutions for the range of small J_c. This is the range of main interest in the scope of this work. However, due to the large phase needed in order to remove the interferences the results differ from analytic results for larger
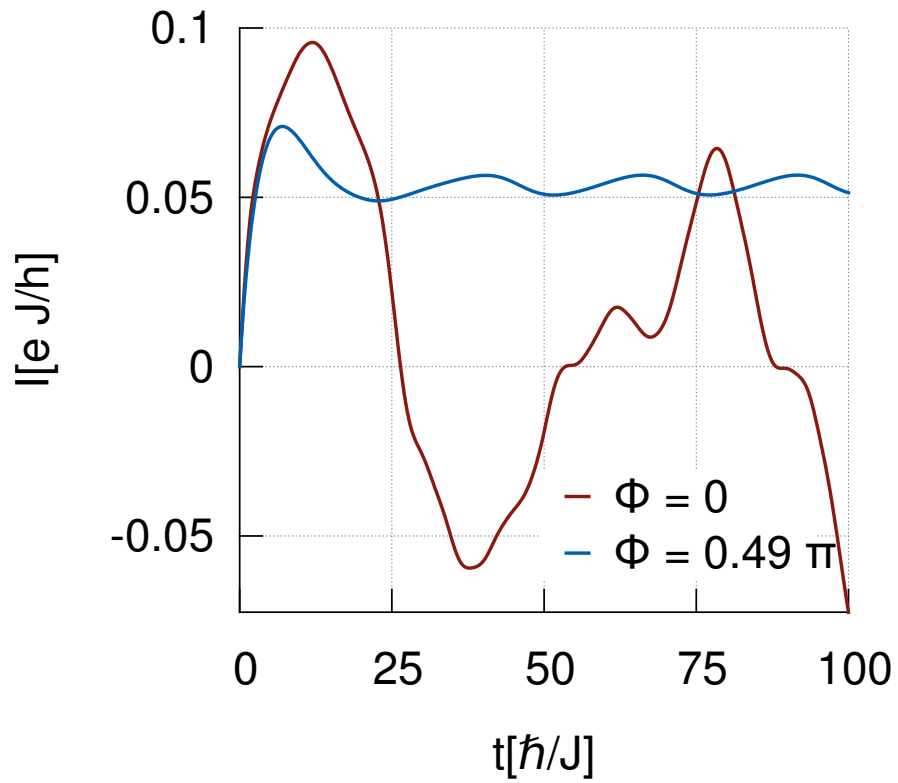
Figure 6.6: Current over time in the noninteracting resonant level model with $M = 50$, $J_c = 0.1J$ and $eV_{SD} = 0.5J$. The blue line gives the result for the method presented in this chapter. The red line gives the result using the usual method.
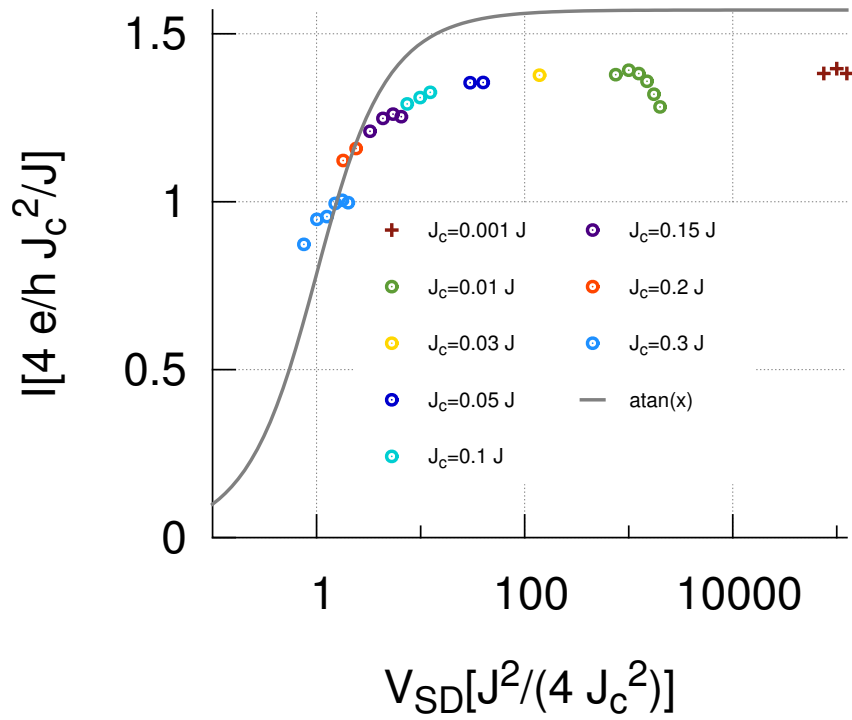
Figure 6.7: Extracted I/V for RLM hamiltonian with phases of $\Phi = 0.494\pi$ and $\Phi = 0.49\pi$ for multiple values of J_c. The straight line gives the approximated analytic scattering theory result. System size used is $M = 50$, timesteps are $J\Delta t = 0.25\hbar$ and $eV_{\mathrm{SD}} \in [0.3J, 0.8J]$.
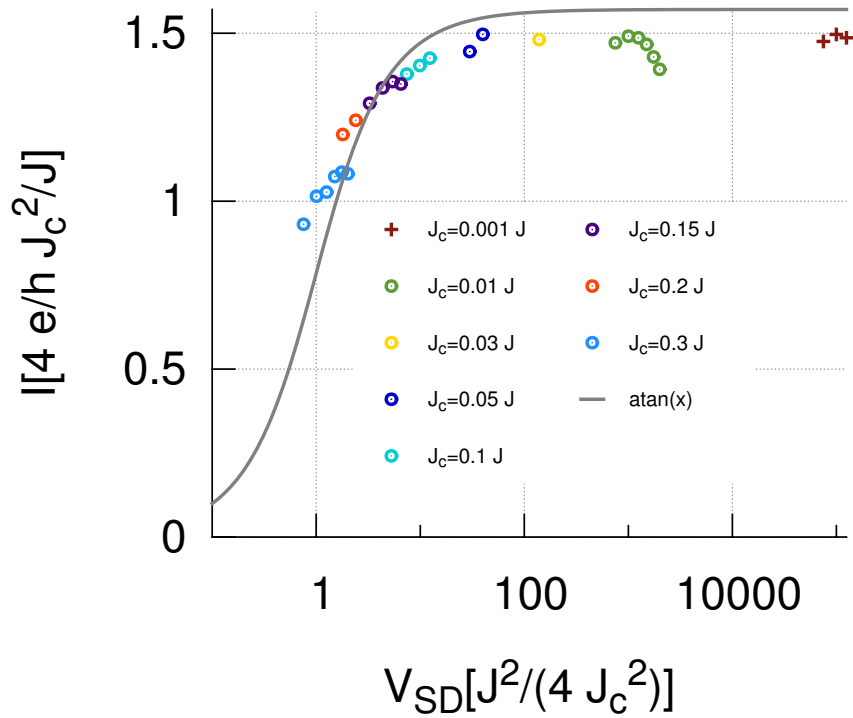
Figure 6.8: Extracted I/V for RLM hamiltonian with phases of $\Phi = 0.494\pi$ and $\Phi = 0.49\pi$ for multiple values of J_c. The straight line gives the approximated analytic scattering theory result. System size used is $M = 50$, timesteps are $J\Delta t = 0.25\hbar$ and $eV_{\text{SD}} \in [0.3J, 0.8J]$. In this plot, the damping towards the edges of the system is considered in the extrapolation of the current through the structure.
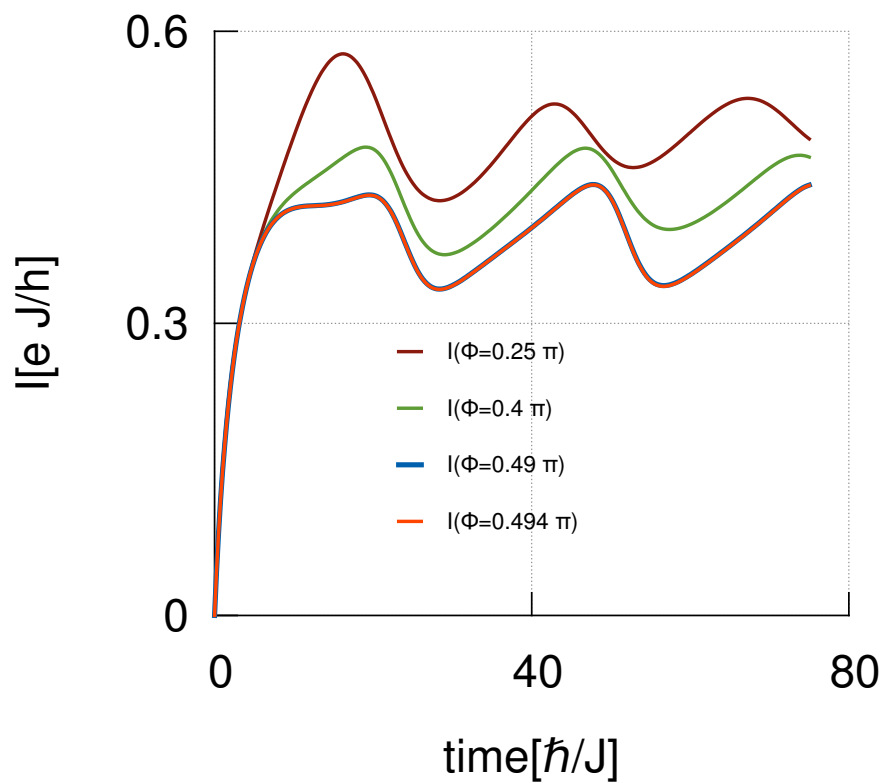
Figure 6.9: Resulting currents for RLM hamiltonian with various phases. System size used is $M = 50$, timesteps are $J\Delta t = 0.25\hbar$. The hopping amplitue is $J_c = 0.3J$, and the bias has the value $eV_{\mathrm{SD}} = 0.5J$.

Figure 6.10: Resulting currents for RLM hamiltonian with various phases. System size used is $M = 150$, timesteps are $J\Delta t = 0.25\hbar$. The hopping amplitue is $J_c = 0.3J$, and the bias has the value $eV_{\mathrm{SD}} = 0.4J$.
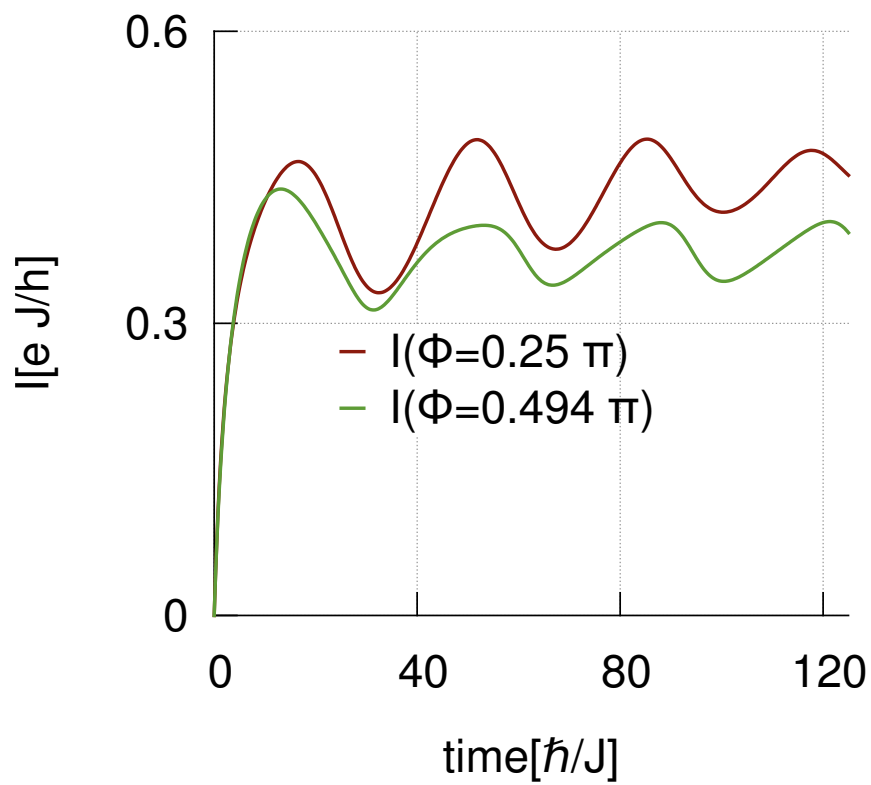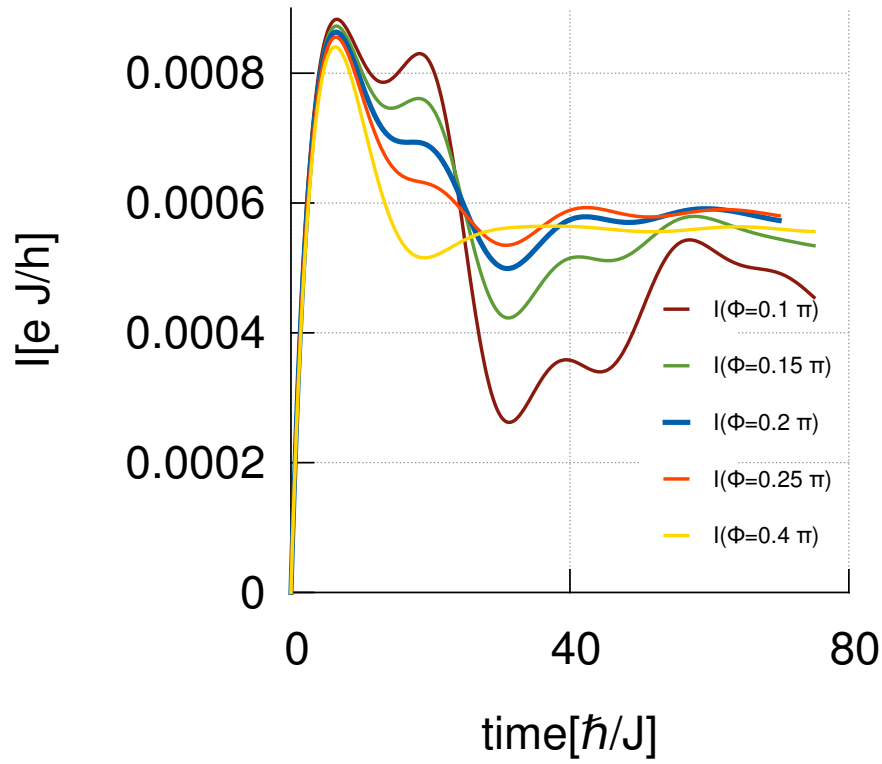
Figure 6.11: Resulting currents for RLM hamiltonian with various phases. System size used is $M = 50$, timesteps are $J\Delta t = 0.25\hbar$. The hopping amplitue is $J_c = 0.01J$, and the bias has the value $eV_{\mathrm{SD}} = 0.5J$.

Figure 6.12: Extracted I/V for RLM hamiltonian with different phases and system sizes for multiple values of J_c. The straight line gives the approximated analytic scattering theory result.
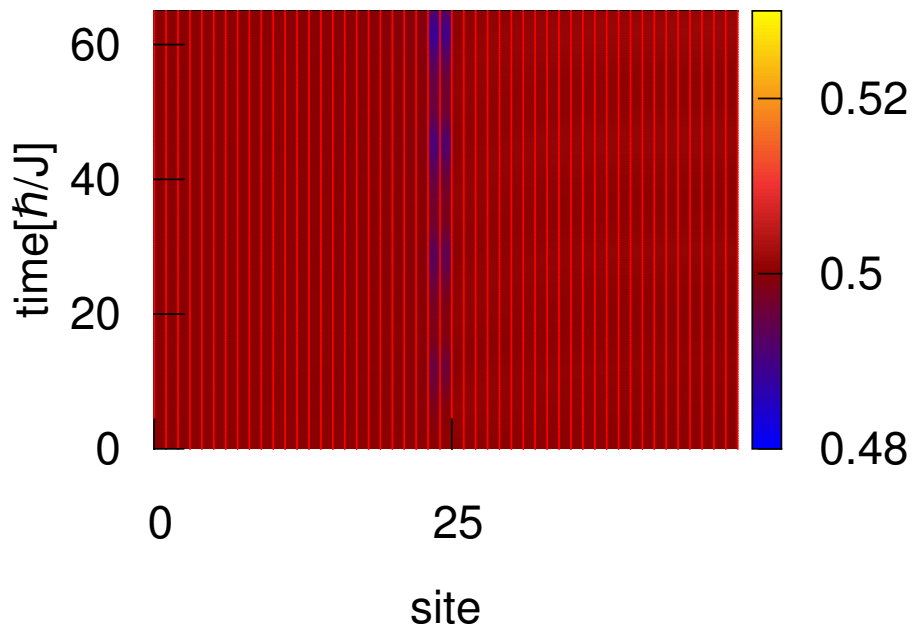
Figure 6.13: Color encoded density distribution over site and time in the RLM, with density oscillations at the structure and uniform density distribution otherwise. Parameters are $M = 50$, $eV_{\text{SD}} = 0.5J$, $J\Delta t = 0.25\hbar$, $J_c = 0.3J$ and $\Phi = 0.494\pi$.
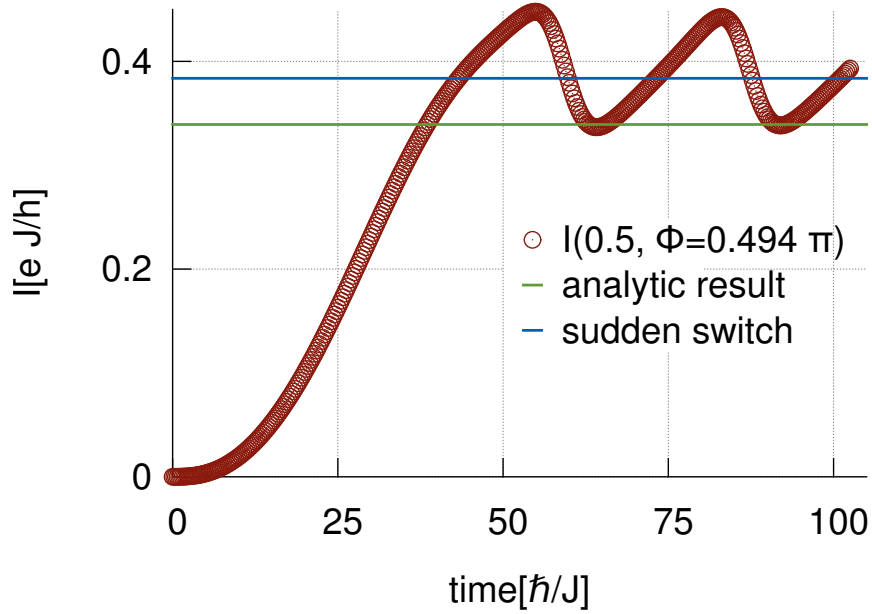
Figure 6.14: Current over time in the noninteracting resonant level model with $M = 50$, $J_c = 0.3J$, $eV_{\mathrm{SD}} = 0.5J$ and $\Phi = 0.494\pi$. The voltage is switched on adiabatically according to the prescription given in Sec. 5.5 and the function given in Eq. (5.33) over the time $J\tau = 60\hbar$. The blue line marks the extracted current value for the situation shown in Fig. 6.5, where the same system parameters and voltage value were used in a sudden voltage switch. The green line marks the analytic result obtained from Eq. (2.29).
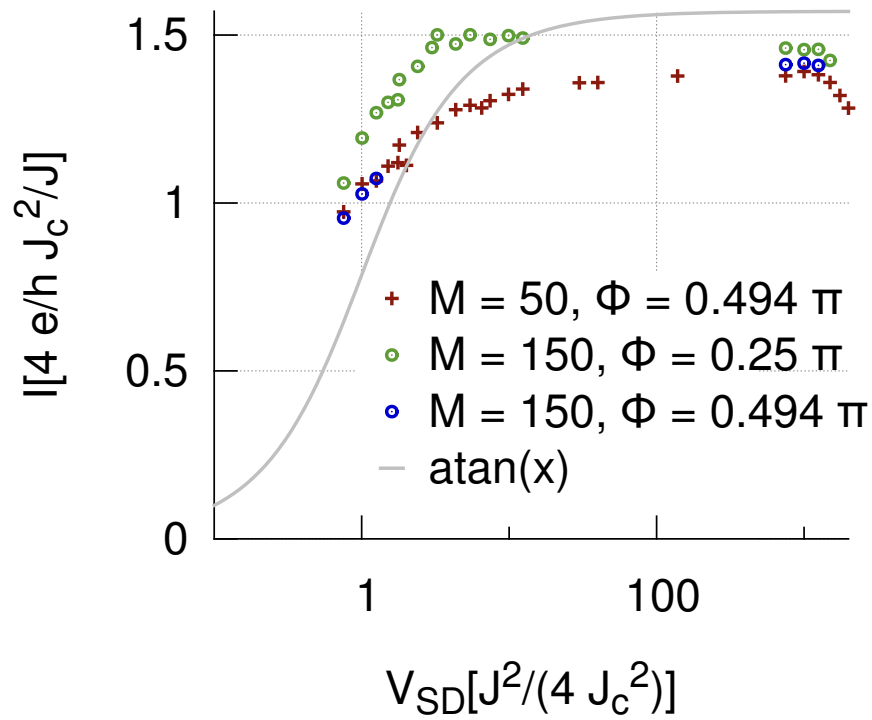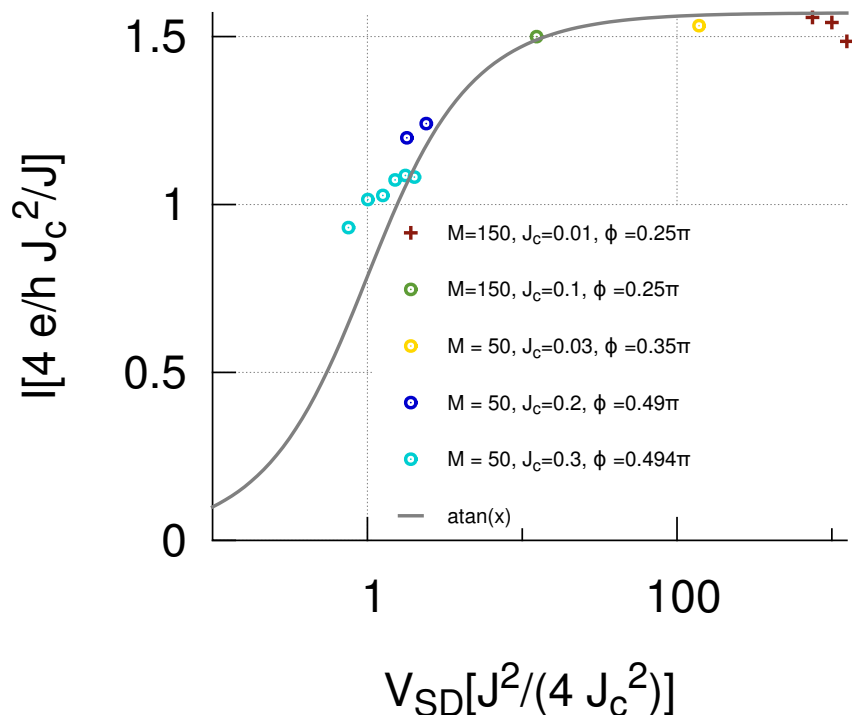
Figure 6.15: Extracted I/V for RLM hamiltonian with different phases and for multiple values of J_c and M. The straight line gives the approximated analytic scattering theory result. The timesteps used in the DMRG time evolution are $J\Delta t = 0.25\hbar$, and $eV_{SD} \in [0.3J, 0.8J]$. In this plot, the damping towards the edges of the system is considered in the extrapolation of the current through the structure.

J_c.

6.4 Steady states and the single particle picture

For noninteracting fermions one usually can apply a single particle picture for the simulation of currents, see Sec. 3.1. Since this chapter has treated the noninteracting RLM as toy model it is enticing to use the single particle picture for the description of transport in the presence of nonhermitian terms in the Hamiltonian. On a closer look it turns out that this does not work.

In the derivation of the end result of Sec. 3.1 the expression $f(\{\hat{n}^t\})$ given in Eq. (3.9) reduces to unity due to the hermiticity of the Hamiltonian. For nonhermitian Hamiltonians $f(\{\hat{n}^t\})$ does not reduce due to the complex eigenvalues of the Hamiltonian and the method breaks down. In a naive application of the single particle picture prescription for current simulation given in Eq. (3.11) the breakdown manifests as infringement of the Pauli principle, see Fig. 6.16. The result of the single particle picture is equivalent to a description of the transport using single particle states in an energy basis. These states do not contain a mechanism to enforce the Pauli principle, i.e. to limit the number of fermions per state to a maximum of one. In noninteracting systems, there is no interplay between the energy levels and the Pauli principle can be regarded via the initial state configuration. The normalization of the wavefunction for nonhermitian time evolution leads to a mix between the single particle energy levels, which will in general lead to a higher occupation of low energy levels.

6.5 Conclusion

In this chapter a simulation prescription which generates steady states during time evolution in finite, one-dimensional systems is presented. The method is based on nonhermitian Hamiltonians, and it is the first method known to the author which generates steady states under the given conditions. Generated currents in general differ from the analytic results for the RLM. A strong agreement of the results is reached for the targeted parameter regime however. The method provides the foundation for the development of refined methods to obtain steady states in many particle wave funtion approaches to the simulation of finite systems.
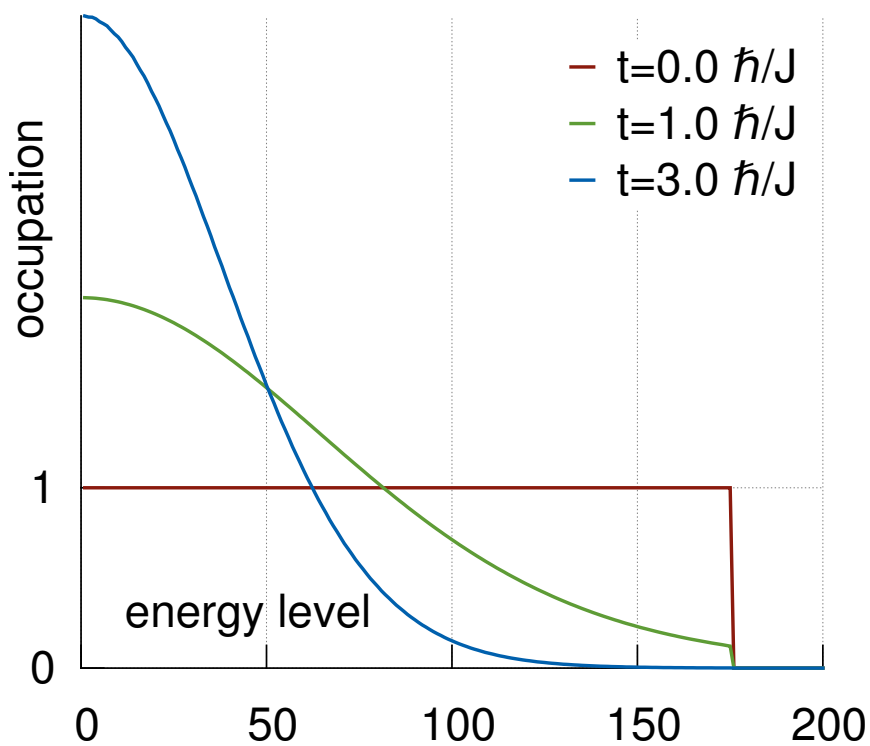
Figure 6.16: Occupation of the two hundred lowest single particle eigenenergy levels of $\hat{\mathcal{H}}_s$ in complex time evolution at different times within a naive single particle picture calculation in the spinless fermion RLM at half filling. Parameters are $M = 350$, $eV_{SD} = 0.5J$, $J_c = 0.3J$ and $J\Delta t = 0.25\hbar$.

Chapter 7

Summary and conclusions

The aim of this thesis is to improve the understanding of nanodevices. This is achieved both by the investigation of mechanisms that could explain experimentally observed properties, and by the provision of new means to study the behavior of such components.

The part of this work on a molecular diode falls into the former category. In a first step a standard is defined which states that molecular rectification effects need to be independent of any external factors. This is required in order to obtain universally applicable molecular diodes, that function in various environments. Known and popular mechanisms that are traditionally used to explain molecular rectification are reviewed, analyzed and investigated. The first investigated and dissected mechanism is the proposal made by Aviram and Ratner that consists of a donor-bridge-acceptor setup. The second one is a static polarization of the molecule. It manifests as both 'asymmetric charging', i.e. an asymmetric transition probability to the two connected leads, and 'asymmetric field', i.e. an adjustment of the energy levels of the molecule depending on the applied voltage. It is also checked whether these single effects meet the standard for rectification defined by the author, yielding a negative result. A new model is therefore proposed representing a dynamical polarizability of the molecule. This mechanism fulfills the posed requirements on molecular rectification and is subsequently used in the simulation of a bridge rectifier. The simulation confirms the usability of the proposed polarizability in electronic devices.

The author's work on molecular rectification provides clarification on the much debated topic of mechanisms that cause molecules to rectify. It provides such a mechanism whose experimental realizations should reliably show asymmetric I/V curves. This is an improvement to e.g. the Aviram Ratner proposal whose early realizations sometimes did not show this feature.

Another part of this work is the project on time evolution in numerical

simulations of systems that vary in time or are exposed to time-dependent influences. In this project the known time-dependent exponential perturbation theory based on the also known Magnus series is embedded in a traditional simulation method. The implementation is based upon an already existing version of DMRG. The good quality of the approximation is tested on a toy model. This results in the finding that very good approximations of the current can be obtained already from the first order of the series. Then the effects of an adiabatic increase of the voltage on the current are investigated, where form and length of the increase are varied. The aim of the investigation is to find a way to reduce the effects of the transient regime and especially the current peak. The result is that the exact form of the increase is of only minor importance. The dependence of the size of the current peak on the duration of the increase is obtained. This knowledge is used in later calculations in order to find an optimum between reduction of the peak and simulation time.

This implementation allows its user to investigate time-dependent systems and time-dependent driving such as the problem of a structure coupled to an alternating voltage.

The third project discussed in this work concentrates on a possibility to obtain steady states in time-resolved simulation on finite one-dimensional fermionic systems. An energetic damping is proposed for this purpose. The good quality of the approximation is tested on the noninteracting resonant level model, and different approaches are tried in order to increase the agreement with analytical results. One of these approaches is an adiabatic voltage increase, which constitutes the motivation for the author's previous investigation of this topic. In the end, very good results are obtained for narrow resonances.

This is the first proposal known to the author that manages to generate steady states for the stated kind of simulations. The steady states are required for current simulations in parameter ranges of interacting systems which contain narrow resonances. In these situations very long simulation times are needed in traditional simulations, which require large system sizes and a huge amount of computational resources. The proposal is a first step towards simulations on these systems.

Four key new results are distilled from this thesis:

- The dissection and analysis of known mechanisms that try to explain molecular rectification into single effects, in combination with

- the investigation of a model of dynamically polarizable molecules which leads to rectification effects independent of external factors.

128

- The implementation of a Krylov space technique to perform time evolution with time-dependent Hamiltonians, tests on the good quality of the approximation and its application to systems under an adiabatic voltage increase.

- The proposal and investigation of energetic damping as a means to obtain steady states in the time-resolved simulation of fermions on finite systems.

The impact and implications of these results can be summarized as:

- A better understanding of the underlying mechanisms of molecular rectification.

- The ability to simulate systems with alternating voltages, interactions of the system with classical electromagnetic fields and other time-dependent systems.

- The advance in the effort to simulate steady state currents in small systems over long times.

- Access to parameter regimes which are not accessible in the time-resolved simulation of electrical currents using traditional methods.

Beyond the presented results some open questions remain. The proposed mechanism of a rectifying molecule needs to be implemented in extended models of real molecules in order to predict or explain rectification. Also the simulation of the bridge rectifier should be completed in order to prove that the rectification effect persists when included in larger devices. The method incorporating the truncated Magnus series is yet to be used in the investigation of a model. Also an improvement of the energetic damping yielding better agreement with analytic results in the regime of large current flow, or a better understanding of the causes for the reduction in agreement in such a regime, would be of advantage. And finally, the proposed energetic damping needs to be tested on known interacting models in a next step. These open questions ensure that the topics encountered in this work will remain interesting for further investigation.

Overall this thesis contributes to the understanding of molecular diodes. It provides a method to treat time-dependent problems and makes the first step towards a steady state simulation on finite systems.

Appendix A

Algorithms used in DMRG procedures

In chapter 3 the DMRG methods are explained. In the explanation algorithms used to obtain eigenvalues of matrices or, closely connected to that, exponentiate matrices in the vicinity of fixed points in time, are mentioned. The appendix introduces these algorithms.

Since some of the algorithms presented here are connected to the Krylov space the main ideas behind Krylov space methods will be given in Sec. A.1. In Sec. A.2 the Jacobi-Davidson algorithm [104], an algorithm for iteratively diagonalizing sparse matrices, is reviewed. In the work presented in this thesis the Jacobi-Davidson algorithm is used for this task over other popular algorithms such as the Lanczos algorithm [105], the Arnoldi algorithm [106, 107] and the Davidson algorithm [108]. This choice is made due to the faster convergence of Jacobi-Davidson and due to the higher stability of the algorithm [65].The difference between Jacobi-Davidson and Davidson algorithm [108] is pointed out in the discussion of the former one in Sec. A.2. The Lanczos algorithm is mentioned in Sec. A.3.3 in which it is compared to the Arnoldi algorithm. Section A.3 thematizes the different approximations made evaluating the time evolution operator in the different time evolution schemes discussed in Sec. 3.2.2. This includes Suzuki-Trotter [71, 72, 73], Runge-Kutta [74, 75, 76] and Arnoldi algorithm. Further information on approximations and algorithms discussed in this appendix is available in Refs. [65, 53, 109, 110, 111].

A.1 The Krylov space

This section contains two viewpoints which motivate the usage of Krylov spaces for the representation of large matrices in algorithms such as the

Lanczos and Arnoldi algorithms.

The first point gives an argument for the usage of Krylov spaces in the extraction of eigenvalues of matrices. After applying $\hat{H}$ a high number of times D to a random vector and renormalizing the resulting vector afterwards, the resulting states read

$$
\begin{aligned}
\frac{1}{N}\hat{H}^D\left|\nu\right\rangle &= \frac{1}{N}\hat{H}^D\sum_i a_i\left|x_i\right\rangle \\
&= \frac{1}{N}\sum_i a_i E_i^D\left|x_i\right\rangle \\
&\approx \sum_i a_i\left(\frac{E_i}{E_{\max}}\right)^D\left|x_i\right\rangle.
\end{aligned}
\tag{A.1}
$$

The normalization of the vectors is named N and for large D, i.e. $a_{\max}^2|E_{\max}^{2D}| \ll |sum_{i\neq\max}a_i^2 E_i^{2D}|$, is approximately given by

$$
\begin{aligned}
N &= \sqrt{a_1^2 E_1^{2D} + \cdots + a_{\max}^2 E_{\max}^{2D} + \cdots} \\
&\approx a_{\max}E_{\max}^D.
\end{aligned}
\tag{A.2}
$$

Only eigenvectors $\left|x_i\right\rangle$ with the absolute values of their eigenvalues E_i close to the absolute value of the maximum eigenvalue $E_{\max}$ contribute significantly. Therefore the elements of Krylov space with $\hat{H}$ applied repeatedly point strongly towards the eigenstates with high absolute eigenvalues. Searching for the extremal eigenvectors by iteratively applying the matrix is called power method. Krylov space methods search in the space spanned by the vectors resulting from the power method for the best approximation to the eigenvector. This yields a convergence which is greatly improved in comparison to the power method.

Since the initial vector is randomly chosen, it can be far – in the sense of the two-norm of the difference between the two vectors being large – to an extremal eigenvector $|x_{\max}\rangle$. In that case the limitations of the naive picture given are shown and a large Krylov basis is needed in order to obtain a good approximation of the extremal eigenvector. Orthonormalization of added basis states with respect to all other basis states is an easy way to account for this and to improve the convergence of Krylov space methods.

The second viewpoint is about the approximation of functions of matrices $\hat{H}$, which act on a given state, using Krylov spaces. It notes that, neglecting symmetries for the moment, the full Hilbert space of dimension d of a problem can be spanned by the states

$$
\left|\nu\right\rangle, \hat{H}\left|\nu\right\rangle, \hat{H}^2\left|\nu\right\rangle, ..., \hat{H}^d\left|\nu\right\rangle,
\tag{A.3}
$$

where $|\nu\rangle$ is a random state or a guessed state with nonvanishing contributions a_i of all eigenstates $|x_i\rangle$ of H. A nonrandom state, or with a very small chance a random state, can have vanishing a_i. If so, only a subspace is spanned, the initial assumption fails and the procedure may break down. In that case, a different choice of starting vector is needed. The argument infers from Eq. (A.3) that the Krylov space is given by states which result from application of polynomials of a matrix to the initial state. Now a function of this matrix acts on a given state which is used as initial state for the construction of a Krylov space. An approximation of the resulting state within the Krylov space then corresponds to an approximation of the matrix function by polynomials, which is a very common approximation, see e.g. the Taylor expansion.

To conclude this section note that the gain of the Krylov space usage is rooted in the fact that application of large matrices to states is much faster than the diagonalization of the matrices. The diagonalization would be needed to execute the operations which are approximated by the Krylov space techniques exactly.

A.2   The Davidson and Jacobi-Davidson methods

The Davidson and Jacobi-Davidson algorithms are recursive diagonalization algorithms used to obtain good approximations for the m lowest eigenvalues up to E_m and eigenvectors up to $|x_m\rangle$ of the diagonalized matrix form of an operator $\hat{H}$ for large Hilbert spaces. In a first step they need a number of $l \geq m$ initial states in vector form $|\nu_i\rangle$ which give the initial basis. These vectors can be orthonormalized random vectors. Starting from these vectors the basis is expanded step by step, and then it is used to represent $\hat{H}$. In later steps of the DMRG procedure the wavefunction prediction is used instead of random vectors to obtain the starting vectors, see the discussion in Sec. B.2 or Ref. [112].

The Jacobi-Davidson algorithm tries to approximate the m lowest eigenvalues of a matrix $\hat{H}$. For that purpose the basis is expanded by correction vectors $|z\rangle$, one for each eigenvector to approximate. The choice of $|z\rangle$ separates the Davidson algorithm from the Jacobi-Davidson algorithm. For pedagogic reasons this section first discusses its calculation in a generalized modification of the Davidson algorithm which is described in Ref. [65]. Then the differences between this version and the traditional Jacobi-Davidson algorithm as well as the used modified versions of the Davidson and Jacobi-

Davidson algorithms is highlighted. The latter is implemented in the DMRG procedure used in the scope of this thesis.

A.2.1 The fundamental concept of the Davidson method

In the Davidson method the correction vectors are approximately given as the difference of the unknown eigenstates of $\hat{H}$ and the corresponding eigenstates of the reduced representation of $\hat{H}$ in the given basis. This way the Basis space is expanded towards the m lowest eigenstates . This is continued until the approximation error given by the two-norm of $|z\rangle$ is below the desired threshold. A requirement to have a m-th lowest eigenvector at each step is that the algorithm starts with at least m orthonormalized initial vectors spanning an initial basis. In order to calculate one of the correction vectors $|z\rangle$ for a given basis spanned by the basis vectors $|\nu_i\rangle$ and for the approximation of the k-th lowest eigenvector $|x_k\rangle$ at an intermediate step, the vectors $|\nu_i\rangle$ are written as columns into the matrix $\hat{V}_l$. The product of $\hat{V}_l$ with its transposed matrix, $\hat{V}_l^T$ is the projection onto the l-dimensional basis spanned by the $|\nu_i\rangle$:

$$\hat{P}_l = \hat{V}_l \hat{V}_l^T. \tag{A.4}$$

$\hat{H}$ is applied to $\hat{V}_l$ to obtain the matrix $\tilde{A}$:

$$\tilde{A} = \hat{H}\hat{V}_l. \tag{A.5}$$

In practice, $\hat{H}$ is only applied to the newest addition to the basis, $|\nu_l\rangle$, since the other results have already been obtained in previous steps. The resulting vector is used as additional column of $\tilde{A}$. $\tilde{A}$ is then multiplied to the transposed matrix $\hat{V}_l^T$, yielding the matrix elements $\hat{h}_{i,j} = \langle\nu_j|\hat{H}|\nu_i\rangle$ of the inclomplete representation $\hat{h}$ of $\hat{H}$:

$$\hat{h} = \hat{V}_l^T \tilde{A} = \hat{V}_l^T \hat{H}\hat{V}_l. \tag{A.6}$$

In an actual algorithm the amount of calculations is again reduced since most of the matrix elements are already known. $\langle\nu_j|\hat{H}|\nu_i\rangle$ is only calculated for fixed $j = l$, and the hermiticity of $\hat{h}$ is used to obtain $\langle\nu_i|\hat{H}|\nu_l\rangle$. The matrix $\hat{h}$ is diagonalized exactly in order to obtain its k-th lowest eigenvector $|\alpha_k\rangle_{\nu_j}$ expressed by the basis states $|\nu_i\rangle$. The corresponding eigenvalue of $\hat{h}$ is λ_k, and its eigenvector represented in the full basis is

$$|\alpha_k\rangle = \hat{V}_l |\alpha_k\rangle_{\nu_j}. \tag{A.7}$$

With this, the correction $|z\rangle$ to $|\alpha_k\rangle$ in order to obtain $|x_k\rangle$ is approximated by

$$|z\rangle := (|x_k\rangle - |\alpha_k\rangle)\,, \tag{A.8}$$

$$\begin{aligned}
\left(\hat{H} - E_k\right)|z\rangle &= -\left(\hat{H} - E_k\right)|\alpha_k\rangle \\
&\approx -\sum_j \left(\hat{H} - E_k\right)|\nu_j\rangle\,\langle\nu_j|\alpha_k\rangle \\
&\approx -\left(\tilde{A} - \lambda_k\right)\sum_j |\nu_j\rangle\,\langle\nu_j|\alpha_k\rangle \\
&= -\left(\tilde{A} - \lambda_k\right)|\alpha_k\rangle_{\nu_j} \\
&=: -|q\rangle
\end{aligned}$$

$$|z\rangle \approx -\left(\tilde{H} - \lambda_k\right)^{-1}|q\rangle\,. \tag{A.9}$$

The preconditioner $\tilde{H}$ is chosen as an easily invertible approximation to $\hat{H}$. The original Davidson algorithm uses a diagonal matrix as preconditioner containing the diagonal elements of $\hat{H}$. Other choices of $\tilde{H}$ are possible, yielding generalized Davidson algorithms, which are more general and more flexible than the original Davidson algorithm [65]. In the scope of this thesis $\tilde{H}$ is a Hamiltonian consisting of the diagonalizable Hamiltonians of smaller blocks of the system without interconnections between them. The different terms in the Hamiltonian are diagonalized simultaneously, so that the full Hamiltonian is diagonalized. To be more specific, the system is divided into blocks A' and B' in Sec. 3.2.1 which are given by the expansion of the blocks A and B by one additional site each. The matrix $\hat{H}$ is the full Hamiltonian of the system:

$$\hat{H} = \hat{\mathcal{H}}_{\mathrm{A}} \otimes 1_2 \otimes 1_{\mathrm{B}} + 1_{\mathrm{A}} \otimes 1_2 \otimes \hat{\mathcal{H}}_{\mathrm{B}} + 1_{\mathrm{A}} \otimes \hat{\mathcal{H}}_2 \otimes 1_{\mathrm{B}} + \hat{\mathcal{H}}_{\mathrm{A'B'}}. \tag{A.10}$$

In this notation $\hat{\mathcal{H}}_{\mathrm{A/B/2}}$ is the Hamiltonian of block A/B represented in the basis of this block or the hamiltonian describing the two additional sites in their basis. The matrices $1_{\mathrm{A/B/2}}$ are unity matrices represented in block A or B or on the two additional sites, and $\hat{\mathcal{H}}_{\mathrm{A'B'}}$ are terms connecting block A' and B', which are represented in the basis of the combined blocks. The used preconditioner $\tilde{H}$ then reads

$$\begin{aligned}
\tilde{H} &= \hat{\mathcal{H}}_{\mathrm{A}} \otimes 1_2 \otimes 1_{\mathrm{B}} + 1_{\mathrm{A}} \otimes 1_2 \otimes \hat{\mathcal{H}}_{\mathrm{B}} + 1_{\mathrm{A}} \otimes \hat{\mathcal{H}}_2 \otimes 1_{\mathrm{B}} \\
&= \hat{H} - \hat{\mathcal{H}}_{\mathrm{A'B'}}.
\end{aligned} \tag{A.11}$$

The vector $|q\rangle$ is calculated in an intermediate step. If its norm is smaller than a chosen error treshold, then $|\alpha_k\rangle$ and λ_k are the desired results of the algorithm. Else $|z\rangle$ is orthonormalized with respect to the remaining basis states via Gram-Schmidt, yielding a new basis state $|\nu_{l+1}\rangle$, and the procedure is repeated.

A.2.2 Adressing the issue of slow convergence in the modified Davidson algorithm

The method described above may experience a slow convergence in case $\tilde{H}$ is close to $\tilde{A}$. This is connected to the vector $|q\rangle$ that was implicitly defined in Eq. (A.9) being close to an eigenvector of $(\tilde{H} - \lambda_k)^{-1}$. If $\tilde{H} = \tilde{A}$ the procedure even breaks down since Eq. (A.9) then would yield

$$
\begin{aligned}
|z\rangle &= -\left(\tilde{A} - \lambda_k\right)^{-1} |q\rangle \\
&= |\alpha_k\rangle_{\nu_j},
\end{aligned}
\tag{A.12}
$$

and $|z\rangle$ would not expand the basis any more. A possible solution to this problem is to modify the vector $|q\rangle$. The traditional Jacobi-Davidson algorithm modifies $|q\rangle$ such that the new search direction $|z\rangle$ is orthogonal to the previous basis vectors $|\nu_j\rangle$, i.e. $\langle z|\nu_i\rangle = 0$:

$$
\begin{aligned}
|q'\rangle &= \left(|q\rangle + \sum_i \epsilon_i |\nu_i\rangle\right), \\
|z\rangle &\approx -\left(\tilde{H} - \lambda_k\right)^{-1} \left(|q\rangle + \sum_i \epsilon_i |\nu_i\rangle\right),
\end{aligned}
\tag{A.13}
$$

where the ϵ_i are chosen such that $|z\rangle$ is orthogonalized against the $|\nu_j\rangle$ as discussed, compare with Eq. (A.14). For the purposes of this work the requirements in computational resources of the traditional Jacobi-Davidson algorithm are too high. In a modified version of the generalized Davidson algorithm [113], which is discussed in Ref. [65], $|q\rangle$ is modified only in the direction of the newest addition to the basis, $|\nu_l\rangle$. This is used only to orthogonalize $|z\rangle$ against $|\nu_l\rangle$ instead of all the basis vectors:

$$
\begin{aligned}
|z\rangle &\approx -\left(\tilde{H} - \lambda_k\right)^{-1} (|q\rangle + \epsilon |\nu_l\rangle), \\
\epsilon &= \langle \nu_l| \left(\tilde{H} - \lambda_k\right)^{-1} |q\rangle.
\end{aligned}
\tag{A.14}
$$

Within this thesis, a modified version of the Jacobi-Davidson method is applied instead. This version splits objects defined in the original Hilbert space into their projection on the reduced space and their projection orthogonal to the reduced space, e.g.

$$
\begin{aligned}
|z\rangle &= \hat{V}_l \hat{V}_l^T |z\rangle + \left(1 - \hat{V}_l \hat{V}_l^T\right) |z\rangle \\
&= \hat{P}_l |z\rangle + |z\rangle^{\perp} .
\end{aligned} \tag{A.15}
$$

It searches for the orthogonal part $|z\rangle^{\perp}$ instead of first calculating $|z\rangle$ and then orthogonalizing. This leads to an equation similar to Eq. (A.9), where the projection $\hat{P}_l^{\perp} = (1 - \hat{V}_l \hat{V}_l^T)$ is used:

$$
\begin{aligned}
|z\rangle^{\perp} &= - \left(\hat{P}_l^{\perp} \tilde{H} \hat{P}_l^{\perp} - \lambda_k\right)^{-1} \hat{P}_l^{\perp} |q\rangle , \\
|q\rangle &= - \left(\tilde{A} - \lambda_k\right) |\alpha_k\rangle_{\nu_j} .
\end{aligned} \tag{A.16}
$$

The objects $|q\rangle$, $\tilde{A}$, λ_k and $\tilde{H}$ are still given by their previous definitions.

A.3   Approximations of the time evolution exponential function

A.3.1   The Suzuki-Trotter approximation

States $|\Psi(t)\rangle$ of the system are evolved in time by application of an exponential function with an antihermitian operator $\hat{A}$ as its argument [89]. E.g. for constant Hamiltonians $\hat{H}$, $\hat{A}$ is given by

$$
\hat{A} = -\frac{\mathrm{i}}{\hbar} \hat{H} \left(t - t_0\right) , \tag{A.17}
$$

with the initial time t_0 and the final time t up to which the state evolves. Therefore a matrix representation of

$$
\hat{U} = \exp\{\hat{A}\} \tag{A.18}
$$

is needed for a given matrix representation of $\hat{A}$. If $\hat{A}$ is of sufficently small dimension to be exactly diagonalizable, $\hat{U}$ is calculated easily in the eigenbasis of $\hat{A}$ as shown e.g. in Sec. 3.1. Unfortunately there is no general precondition method, i.e. a method using preconditioners similar to the Jacobi-Davidson method, available to compute matrix exponentials [114] for larger dimensions

of $\hat{A}$. Three feasible schemes for the approximation of $\hat{U}$ are presented in Sec. A.3.

The first scheme is the Suzuki-Trotter approximation [71, 72, 73]. It is used in Sec. 3.3.1 as a means to separate the exponential function $\hat{U}$ acting on all sites simultaneously into exponentials which act locally on the bond of only two sites. They are expressed in a reduced Hilbert space and computed exactly. The algorithm is based on the observation that for arbitrary operators $\hat{A}_1...\hat{A}_m$ the series

$$\hat{U}_n = \left[\exp\left\{ \frac{1}{n}\hat{A}_1 \right\} \exp\left\{ \frac{1}{n}\hat{A}_2 \right\} \cdots \exp\left\{ \frac{1}{n}\hat{A}_m \right\} \right]^n \tag{A.19}$$

converges for large n towards the exponential

$$\hat{U}' = \exp\left\{ \sum_{j=1}^{m} \hat{A}_j \right\}. \tag{A.20}$$

The observation is known as generalized Trotter formula [72]. In the context of Sec. 3.3.1 the operators $\hat{A}_j$ correspond to non-commuting parts of $\hat{A}$, are expressed through time independent hamiltonians $\hat{H}_j$ via

$$\hat{A}_j = -\frac{i}{\hbar}\hat{H}_j \left(t - t_0 \right), \tag{A.21}$$

and $\hat{U}' = \hat{U}$. Also the systems considered with Suzuki-Trotter contain nearest neighbour interactions only. One possible method [66] uses the splitting

$$\hat{A} = \hat{A}_1 + \hat{A}_2, \tag{A.22}$$

where $\hat{A}_1$ contains interactions of even bonds, i.e. between sites zero and one, zwo and three and so on. $\hat{A}_2$ contains interactions of odd bonds, i.e. between sites one and two, three and four etc. This way every term in $\hat{A}_1$ commutes with each other, and the same goes for $\hat{A}_2$, but $\hat{A}_1$ and $\hat{A}_2$ do not commute. As an example, for an infinite chain with constant hopping,

$$i\hbar\hat{A} = -J \sum_{x=-\infty}^{\infty} c_x^\dagger c_{x+1}^\dagger + \text{h.c.},$$

$$i\hbar\hat{A}_1 = -J \sum_{x=-\infty}^{\infty} c_{2x}^\dagger c_{2x+1}^\dagger + \text{h.c.},$$

$$i\hbar\hat{A}_2 = -J \sum_{x=-\infty}^{\infty} c_{2x+1}^\dagger c_{2x+2}^\dagger + \text{h.c.}. \tag{A.23}$$

$\hat{U}$ is approximated by the $n = 2$ term of the series [66]

$$\hat{U}_2 = \exp\left\{\frac{1}{2}\hat{A}_1\right\} \exp\left\{\hat{A}_2\right\} \exp\left\{\frac{1}{2}\hat{A}_1\right\}. \tag{A.24}$$

This term is a second order approximation of $\hat{U}$ in $(t - t_0)$ [66], and a generalization to higher orders is straightforward. Since the local Hamiltonians of all even bonds commute with each other, their time evolution exponentials separate exactly,

$$\exp\left\{\hat{A}_1\right\} = \prod_{x=-\infty}^{\infty} \exp\left\{-\frac{i}{\hbar}\left(c_{2x}^\dagger c_{2x+1}^\dagger + \text{h.c.}\right)(t - t_0)\right\}. \tag{A.25}$$

After an analogous treatment of the odd bonds, the whole time evolution is carried out by an application of the single local operators to even bonds first in any order, then to odd bonds, then to the even bonds again.

The method discussed in Sec. 3.3.1 for a system with M sites separates $\hat{A}$ into $M - 1$ operators $\hat{A}_j$ with

$$\hat{A}_j \propto c_{j-1}^\dagger c_j^\dagger + \text{h.c.} \tag{A.26}$$

and approximates the exponential at the same order of Trotter error by

$$\hat{U}_2 = \exp\left\{\frac{1}{2}\hat{A}_1\right\} \exp\left\{\frac{1}{2}\hat{A}_2\right\} \cdots \ldots \exp\left\{\frac{1}{2}\hat{A}_2\right\} \exp\left\{\frac{1}{2}\hat{A}_1\right\}. \tag{A.27}$$

This allows to apply the local time evolution operators ordered in the same way as the recursion procedure of the improvement of the basis in DMRG, see Sec. 3.2.2 and Sec. 3.3.1 for details. The method is widely used if only nearest neighbour hopping problems are considered, but is not applicable for more general problems.

A.3.2 The Runge-Kutta method

For general $\hat{A}$ another approach has to be used. In the approach discussed in this section, instead of the exponential function governing the time evolution, the Schrödinger equation

$$\frac{d}{dt}|\Psi(t)\rangle = -\frac{i}{\hbar}\hat{H}(t)|\Psi(t)\rangle \tag{A.28}$$

for the state $|\Psi(t)\rangle$ of the system is considered. An approximated solution to this equation is given by the Runge-Kutta prescription [74, 75, 76]. A

thorough discussion of this approximation is given e.g. in Ref. [115]. There exist many Runge-Kutta prescriptions. They have in common that solutions at later timesteps $|\Psi(t + \Delta t)\rangle$ are constructed by addition of interpolated solutions $k_i = |\Psi(t + x)\rangle$, $x_i < \Delta t$, at intermediate timesteps with a weight b_i. The exact interpolation formulas and weights distinguish the different realizations as well as the order of the approximation. Unfortunately the various Runge-Kutta methods share the lack of unitarity. A common example for a Runge-Kutta method is the standard fourth-order Runge-Kutta algorithm [67]

$$|\Psi(t + \Delta t)\rangle = |\Psi(t)\rangle + \sum_{i=1}^{4} b_i k_i, \tag{A.29}$$

$$b_i = \frac{1}{6}\left(1 + \delta_{i,2} + \delta_{i,3}\right),$$

$$k_1 = -\frac{i}{\hbar}\Delta t \hat{H}(t) |\Psi(t)\rangle,$$

$$k_2 = -\frac{i}{\hbar}\Delta t \hat{H}\left(t + \frac{\Delta t}{2}\right)\left(|\Psi(t)\rangle + k_1\right),$$

$$k_3 = -\frac{i}{\hbar}\Delta t \hat{H}\left(t + \frac{\Delta t}{2}\right)\left(|\Psi(t)\rangle + k_2\right),$$

$$k_4 = -\frac{i}{\hbar}\Delta t \hat{H}(t + \Delta t)\left(|\Psi(t)\rangle + k_3\right). \tag{A.30}$$

A.3.3 The Arnoldi algorithm

Another approach to the problem of exponentiating large matrices is to approximate the matrix in a small subspace, which then allows for an exact diagonalization. Since the exponential can be written in form of a Taylor series, i.e. a series of polynomials of the matrix, the Krylov spaces which are constructed of such polynomials and which are introduced in Sec. A.2 are a common choice for the subspace. The Krylov space method of choice within the scope of this work is based on the Arnoldi algorithm [106, 107]. This method is presented in Ref. [116]. As starting vector for the construction of the Krylov space the vector

$$|v_1\rangle = \frac{1}{\sqrt{N}}|\Psi(t)\rangle \tag{A.31}$$

which is to be evolved in time as in Eq. (A.28) by application of the time evolution $\hat{U}$ given in Eq. (A.18) is used. $|v_1\rangle$ is normalized by division through

the norm $\sqrt{N}$ of $|\Psi(t)\rangle$. Now the standard Krylov space construction with modified Gram-Schmidt orthonormalization is applied to obtain the additional Krylov space basis vectors $|v_2\rangle \cdots |v_m\rangle$ for an m-dimensional subspace of the d-dimensional representation of $|\Psi(t)\rangle$. In step j this means that first the not yet orthonormalized vector

$$|v_{j+1}\rangle = \hat{A}|v_j\rangle \tag{A.32}$$

is calculated in the d-dimensional space. The modified Gram-Schmidt orthogonalization is then carried out with respect to one basis vector at a time, meaning that

$$\left|v'_{j+1}\right\rangle = |v_{j+1}\rangle - \langle v_i|v_{j+1}\rangle |v_i\rangle,$$
$$|v_{j+1}\rangle := \left|v'_{j+1}\right\rangle / \left\langle v'_{j+1}|v'_{j+1}\right\rangle \tag{A.33}$$

for the indices $i = 1 \cdots j$ in ascending order. The vector $|v_{j+1}\rangle$ is normalized after the orthogonalization. If the normalization constant is smaller than a chosen lower bound or if the chosen dimension of the subspace is reached, the construction of the Krylov subspace is stopped. The overlaps

$$a_{i,j} = \langle v_i|v_{j+1}\rangle$$
$$= \langle v_i|\hat{A}|v_j\rangle,$$
$$a_{j+1,j} = \langle v_{j+1}|v_{j+1}\rangle$$
$$= \langle v_{j+1}|\hat{A}|v_j\rangle \tag{A.34}$$

form the matrix elements of the projection $\hat{A}_m$ of $\hat{A}$ onto the Krylov subspace with dimension m. The vectors $|v_j\rangle$ correspond to the columns of a projection operator $\hat{V}_m$ with $\hat{A}\hat{V}_m = \hat{V}_m\hat{A}_m$. In the d-dimensional space this operator reads $\hat{V}_m\hat{V}_m^\dagger$. The time evolution can now be approximated by a projection onto the constructed Krylov space:

$$|\Psi(t + \Delta t)\rangle = \hat{U}|\Psi(t)\rangle$$
$$\approx \hat{U}\hat{V}_m\hat{V}_m^\dagger|\Psi(t)\rangle$$
$$= \frac{1}{\sqrt{N}}\hat{V}_m \exp\left\{\hat{A}_m\right\}\hat{V}_m^\dagger|v_1\rangle$$
$$= \frac{1}{\sqrt{N}}\hat{V}_m \exp\left\{\hat{A}_m\right\}|e_1\rangle. \tag{A.35}$$

Here, $|e_1\rangle$ denotes the unit vector in the direction of the first basis vector in the m-dimensional Krylov space, and the exponential of $\hat{A}_m$ can be calculated exactly using exact diagonalization.

The Arnoldi algorithm gives very good approximations already for small Krylov spaces [77]. For hermitian matrices and in exact numerics it is formally equivalent to the Lanczos Algorithm, which typically needs less than one hundred iterations for high accuracy approximations [65]. The difference between the two algorithms is that Lanczos requires only up to three vectors to be stored at any step. On the downside of this, orthogonality is often lost after some iterations and the algorithm is less stable than Arnoldi. Also the Lanczos method by construction only applies to hermitian matrices while Arnoldi generalizes Lanczos to non-hermitian matrices [65].

The advantage of Krylov subspace methods leading to their application over e.g. Runge-Kutta in the context of this work is the preservation of unitarity during time evolution, which is not guaranteed for arbitrary order Runge-Kutta approximations.

Appendix B

Improvements on the performance of DMRG procedures

This chapter provides some information on the ideas behind two modifications of the DMRG procedures discussed in chapter 3. The modifications are not necessary for the DMRG in order to perform their task but they improve the performance.

B.1 Conserved generalized charges in DMRG procedures

In Sec. 3.2.1 a basic form of the iDMRG algorithm is presented which dissects the basis space Ω_S into a tensor product of subspaces ω_x at positions x. there, the dissection takes the form of Eq. (3.22),

$$\Omega_S = \omega_1 \otimes \omega_2 \otimes \cdots \otimes \omega_M. \tag{B.1}$$

Computations using the DMRG algorithms are performed much faster if the algorithms make use of the quantum numbers of the system. The states are sorted according to their quantum numbers labeling conserved generalized charges due to symmetries. This leads to some bookkeeping but speeds up matrix multiplications applied e.g. during the Jacobi-Davidson diagonalization algorithm [108, 104]. E.g. for conserved particle number N Ω_S is written as direct sum of subspaces $\omega_S(n)$ with particle number n. The $\omega_S(n)$ then are decomposed as a tensor product of the subspaces $\omega_B(n)$ of two blocks A

and B by

$$\Omega_S = \omega_S \left(n = 0 \right) \oplus \omega_S \left(n = 1 \right) \oplus \cdots \oplus \omega_S \left(n = N + 1 \right)$$
$$\omega_S \left(n = 2 \right) = \omega_A \left(n = 2 \right) \otimes \omega_B \left(n = 0 \right)$$
$$\oplus \omega_A \left(n = 1 \right) \otimes \omega_B \left(n = 1 \right)$$
$$\oplus \omega_A \left(n = 0 \right) \otimes \omega_B \left(n = 2 \right). \tag{B.2}$$

The decomposition continues up to systems consisting of just one site. Subspaces containing too many particles are omitted. Subspaces containing one more particle than the desired number of particles have to be kept in order to represent creation operators.

In the example given in Sec. 3.2.1 the creation operator acting on site 1 described in a two-site block read

$$\hat{c}_1^\dagger \left(2 \right) = \begin{pmatrix} 0 & 1 \\ 0 & 0 \end{pmatrix}_1 \otimes \begin{pmatrix} 1 & 0 \\ 0 & 1 \end{pmatrix}_2, \tag{B.3}$$

see Eq. (3.24). Written in terms of subspaces, the projection of the operator $\hat{c}_x^\dagger \left(y, n, m \right)$ acting on site $x = 1$ represented in a $y = 2$-site basis connecting the subspace with $m = 0$ particles to the one with $n = 1$ particles reads

$$\hat{c}_1^\dagger \left(2, 1, 0 \right) = \begin{pmatrix} 0 & 1 \\ 0 & 0 \end{pmatrix}_1 \otimes (1)_2^0, \tag{B.4}$$

where $(1)_2^0$ is the unit matrix in the one dimensional subspace of site two with zero particles. E.g. an expansion of $(1)_2^0$ to the full Hilbert space at site two gives

$$(1)_2^0 \to \begin{pmatrix} 0 & 0 \\ 0 & 1 \end{pmatrix}_2. \tag{B.5}$$

The annihilation operator acting on site $x = 2$ gets projected to

$$\hat{c}_2 \left(2, 0, 1 \right) = (1)_1^0 \otimes \begin{pmatrix} 0 & 0 \\ 1 & 0 \end{pmatrix}_2. \tag{B.6}$$

Analogously, the connection between the one and two particle subspaces and the operator on the full subspace expressed through these operators read

$$\hat{c}_1^\dagger \left(2, 2, 1 \right) = \begin{pmatrix} 0 & 1 \\ 0 & 0 \end{pmatrix}_1 \otimes (1)_2^1, \tag{B.7}$$

$$\hat{c}_1^\dagger \left(2 \right) = \hat{c}_1^\dagger \left(2, 1, 0 \right) \oplus \hat{c}_1^\dagger \left(2, 2, 1 \right). \tag{B.8}$$

In the notation using direct sums of subspaces the Hamiltonian $\hat{\mathcal{H}}(x)$ of the $x = 2$-site block within the leads now becomes

$$
\begin{aligned}
\hat{\mathcal{H}}(2) &= -J\left(\hat{c}_1^\dagger(2)\,\hat{c}_2(2) + \hat{c}_2^\dagger(2)\,\hat{c}_1\right), \\
&= \hat{\mathcal{H}}(2,0) \oplus \hat{\mathcal{H}}(2,1) \oplus \hat{\mathcal{H}}(2,2) \qquad\qquad\qquad\text{(B.9)}
\end{aligned}
$$

$$\hat{\mathcal{H}}(2,0) = 0,$$

$$
\begin{aligned}
\hat{\mathcal{H}}(2,1) &= -J\left(\hat{c}_1^\dagger(2,1,0)\,\hat{c}_2(2,0,1) + \hat{c}_2^\dagger(2,1,0)\,\hat{c}_1(2,0,1)\right), \\
&= -J\left(\begin{pmatrix} 0 & 1 \\ 0 & 0 \end{pmatrix}_1 \otimes \begin{pmatrix} 0 & 0 \\ 1 & 0 \end{pmatrix}_2 + \begin{pmatrix} 0 & 0 \\ 1 & 0 \end{pmatrix}_1 \otimes \begin{pmatrix} 0 & 1 \\ 0 & 0 \end{pmatrix}_2\right),
\end{aligned}
$$

$$\hat{\mathcal{H}}(2,2) = 0. \qquad\qquad\qquad\qquad\qquad\qquad\qquad\qquad\text{(B.10)}$$

Here, $\hat{\mathcal{H}}(x,n)$ denotes the hamiltonian of a subsystem with x sites and n particles. The example given here is about the construction of an exact basis in the initial step. However the categorization by quantum numbers is also applied in the other steps, e.g. during the expansion of the system.

B.2   The wavefunction prediction

The amount of iterations needed for the Jacobi-Davidson method described in Sec. A.2 is reduced by the usage of the wavefunction prediction proposed in [112]. In the finite lattice DMRG discussed in Sec. 3.2.2 the wavefunction prediction replaces the initial random vectors by the resulting low energy wavefunctions of the previous DMRG iteration step, which are represented in the transformed basis. In order to give an explicit transformation for the wavefunctions, one step of the process of updating the basis needs to be revisited.

Let us assume that the Jacobi-Davidson of the previous step results in the low energy wavefunctions $|\Psi_n\rangle$ given by

$$|\Psi_n\rangle \to \sum_{i,j,k,l} \Psi_{i,j,k,l}^n |i\rangle_\text{A} |j\rangle_1 |k\rangle_2 |l\rangle_\text{B}. \qquad\qquad\text{(B.11)}$$

Here, $|i\rangle_\text{A/B}$ are the basis vectors of blocks A and B, and $|i\rangle_{1/2}$ denote the basis vectors of the two added sites, indexed as site one and two. The $|\Psi_n\rangle$ are used to obtain the reduced density matrix $\hat{\rho}_{\text{A}'}$ of block A' which is composed of block A and additional site one via Eq. (3.31). $\hat{\rho}_{\text{A}'}$ is diagonalized

via the transformation matrix $\hat{U}^{A'}$ to the new basis $|m\rangle_{A'}^{\text{full}}$:

$$|m\rangle_{A'}^{\text{full}} = \sum_{i,j} \left[\hat{U}_{A'}\right]_{ijm} |i\rangle_A |j\rangle_1 ,$$

$$|i\rangle_A |j\rangle_1 = \sum_m \left[\hat{U}_{A'}^{\dagger}\right]_{mij} |m\rangle_{A'}^{\text{full}} . \tag{B.12}$$

Here, $[\hat{O}]_{ij}$ denotes element ij of the matrix $\hat{O}$. The basis is projected to the N_{cut} highest weights of $\hat{\rho}_{A'}$ via $\hat{P}_{A'} = \hat{V}_{A'}\hat{V}_{A'}^T$, resulting in the basis given by $|m\rangle_{A'}$:

$$|m\rangle_{A'}^{\text{full}} \rightarrow \left[\hat{V}_{A'}\right]_{m,o} |o\rangle_{A'} . \tag{B.13}$$

The matrix $\hat{V}_{A'}$ has dimensions $d \times N_{\text{cut}}$ and entries $\hat{V}_{A',\text{ij}} = \delta_{i,j}$. In other words it contains the N_{cut} kept eigenvectors of $\hat{\rho}_{A'}$ represented in the eigenbasis of $\hat{\rho}_{A'}$ as columns. Its transposed matrix is given by $\hat{V}_{A'}^T$. The arrow $\rightarrow$ indicates that information is irreversibly lost going in its direction due to the projection. The representation of $|\Psi_n\rangle$ in the reduced basis of block A', and the bases of block B and site two, thus reads

$$|\Psi_n\rangle = \sum_{k,l,o} \Phi_{k,l,o}^n |o\rangle_{A'} |k\rangle_2 |l\rangle_B ,$$

$$\Phi_{k,l,o}^n \equiv \sum_{i,j,m} \Psi_{i,j,k,l}^n \left[\hat{U}_{A'}^{\dagger}\right]_{ijm} \left[\hat{V}_{A'}\right]_{m,o} . \tag{B.14}$$

In a previous step, either in DMRG or iDMRG, the basis $|i\rangle_B$ of block B with x sites was obtained from the basis $|i\rangle_{B_{\text{prev}}}$ of block B_{prev} with $x - 1$ sites and an additional site three by

$$|l\rangle_B \leftarrow \sum_q \left[\hat{V}_B^T\right]_{lq} \left[\hat{U}_B\right]_{qrs} |r\rangle_3 |s\rangle_{B''} . \tag{B.15}$$

Inserting Eq. (B.15) into Eq. (B.14) yields the transformation to the basis which is present in the Jacobi-Davidson of this step:

$$|\Psi_n\rangle \rightarrow \sum_{o,k,r,s} \phi_{o,k,r,s}^n |o\rangle_{A'} |k\rangle_2 |r\rangle_3 |s\rangle_{B''} ,$$

$$\phi_{o,k,r,s}^n \equiv \sum_{i,j,m,q} \Psi_{i,j,k,l}^n \left[\hat{U}_{A'}^{\dagger}\right]_{ijm} \left[\hat{V}_{A'}\right]_{m,o} \left[\hat{V}_B^T\right]_{lq} \left[\hat{U}_B\right]_{qrs} . \tag{B.16}$$

These wavefunctions replacing $|\Psi_n\rangle$ are used as initial guesses for the Jacobi-Davidson algorithm. In the first DMRG step, transformations and wavefunctions obtained from iDMRG are used.

XVI

The difference in the Hamiltonians used in the Jacobi-Davidson run and in the previous run is due to the different spaces spanned by the bases and is small. Since the wavefunctions were solutions of the previous run and therefore of a nearly identical problem, they are supposed to be good initial guesses to the solution of the current run.

In adaptive DMRG the time evolving wavefunction is present in all steps during the iterations. The required basis transformations of the wavefunction are performed in analogy to Eq. (B.16).

Bibliography

[1] T. HAGER, *Force of Nature: The Life of Linus Pauling*, 1995.

[2] T. COLLET and P. SCHMITTECKERT, *EPL* **107**, 48005 (2014).

[3] T. COLLET and P. SCHMITTECKERT, *submitted to Annalen der Physik* .

[4] F. BRAUN, *Annalen der Physik und Chemie* **153**, 556 (1874).

[5] A. R. BURKS and A. W. BURKS, *The first electronic computer: the Atanasoff story*, University of Michigan Press, 1989.

[6] A. AVIRAM and M. A. RATNER, *Chem. Phys. Lett.* **29** (1974).

[7] V. BALZANI, A. CREDI, and M. VENTURI, *ChemPhysChem* **4**, 49 (2003).

[8] R. LANDAUER, *Journal of Mathematical Physics* **37**, 5259–5268 (1996).

[9] R. LANDAUER, *Philosophical Magazine* **21**, 863 (1970).

[10] M. BÜTTIKER, *Phys. Rev. Lett.* **57**, 1761 (1986).

[11] S. MAO, T. SHANG, B. PARK, D. D. ANDERSON, and S. J. DILLON, *Applied Physics Letters* **104**, (2014).

[12] B. A. LIPPMANN and J. SCHWINGER, *Phys. Rev.* **79**, 469 (1950).

[13] N. S. WINGREEN, A.-P. JAUHO, and Y. MEIR, *Phys. Rev. B* **48**, 8487 (1993).

[14] W. KOHN and L. J. SHAM, *Phys. Rev.* **140**, A1133 (1965).

[15] M. SCHLÜTER and S. LU JEU, *Physics Today* **35**, 36 (1982).

[16] J. E. HIRSCH and R. M. FYE, *Phys. Rev. Lett.* **56**, 2521 (1986).

[17] A. N. RUBTSOV, V. V. SAVKIN, and A. I. LICHTENSTEIN, *Phys. Rev. B* **72**, 035122 (2005).

[18] P. WERNER, A. COMANAC, L. DE' MEDICI, M. TROYER, and A. J. MILLIS, *Phys. Rev. Lett.* **97**, 076405 (2006).

[19] E. GULL, A. J. MILLIS, A. I. LICHTENSTEIN, A. N. RUBTSOV, M. TROYER, and P. WERNER, *Rev. Mod. Phys.* **83**, 349 (2011).

[20] G. COHEN, D. R. REICHMAN, A. J. MILLIS, and E. GULL, *Phys. Rev. B* **89**, 115139 (2014).

[21] L. MÜHLBACHER and E. RABANI, *Phys. Rev. Lett.* **100**, 176403 (2008).

[22] P. WERNER, T. OKA, and A. J. MILLIS, *Phys. Rev. B* **79**, 035320 (2009).

[23] K. G. WILSON, *Rev. Mod. Phys.* **47**, 773 (1975).

[24] S. R. WHITE, *Phys. Rev. Lett.* **69**, 2863 (1992).

[25] M. A. CAZALILLA and J. B. MARSTON, *Phys. Rev. Lett.* **88**, 256403 (2002).

[26] P. SCHMITTECKERT, *Phys. Rev. B* **70**, 121302 (2004).

[27] K. A. AL-HASSANIEH, A. E. FEIGUIN, J. A. RIERA, C. A. BÜSSER, and E. DAGOTTO, *Phys. Rev. B* **73**, 195304 (2006).

[28] D. BOHR, P. SCHMITTECKERT, and P. WÖLFLE, *EPL* **73**, 246 (2006).

[29] T. GIAMARCHI, *Quantum Physics in One Dimension*, Oxford University Press.

[30] L. LANDAU, *JETP* **3**, 920 (1956).

[31] L. LANDAU, *JETP* **5**, 101 (1957).

[32] L. LANDAU, *JETP* **8**, 70 (1959).

[33] L. LANDAU and E. LIFSCHITZ., *Lehrbuch der theoretischen Physik Band IX: Statistische Physik, Teil 2.*, Akademie-Verlag-Berlin, 1984.

[34] R. H. Baughman, A. A. Zakhidov, and W. A. d. Heer, *Science* **297**, pp. 787 (2002).

[35] Goldhaber-Gordon D., Shtrikman Hadas, Mahalu D., Abusch-Magder David, Meirav U., and Kastner M. A., *Nature* **391**, 156 (1998), 10.1038/34373.

[36] J. Zhao, C. Zeng, X. Cheng, K. Wang, G. Wang, J. Yang, J. Hou, and Q. Zhu, *Phys. Rev. Lett.* **95** (2005).

[37] A. Chatterjee and B. Deopura, *Fibers and Polymers* **3**, 134 (2002).

[38] V. V. Mitin, V. Kochelap, and M. A. Stroscio, *Quantum heterostructures: microelectronics and optoelectronics*, Cambridge University Press, 1999.

[39] H. Kalt, *Optical properties of III-V semiconductors*, Springer, 1996.

[40] C. Weisbuch and B. Vinter, *Quantum semiconductor structures: Fundamentals and applications*, Elsevier, 1991.

[41] R. Dingle, W. Wiegmann, and C. H. Henry, *Phys. Rev. Lett.* **33**, 827 (1974).

[42] M. Elbing, R. Ochs, M. Koentopp, M. Fischer, C. von Hänisch, F. Weigend, F. Evers, H. B. Weber, and M. Mayor, *Proceedings of the National Academy of Sciences of the United States of America* **102**, 8815 (2005).

[43] P. F. Barbara, T. J. Meyer, and M. A. Ratner, *The Journal of Physical Chemistry* **100**, 13148 (1996).

[44] V. Balzani, *Electron Transfer in Chemistry*, WILEY-VCH Verlag, 2001.

[45] A. M. Kuznetsov and J. Ulstrup, *Electron Transfer in Chemistry and Biology*, WILEY-VCH Verlag, 1998.

[46] H. Kuhn and D. Möbius, *Angewandte Chemie International Edition in English* **10**, 620–637 (1971).

[47] Davis William B., Svec Walter A., Ratner Mark A., and Wasielewski Michael R., *Nature* **396**, 60 (1998), 10.1038/23912.

[48] N. J. Geddes, D. J. Sandman, J. R. Sambles, D. J. Jarvis, and W. G. Parker, *Appl. Phys. Lett.* **56** (1990).

[49] M. A. Reed, C. Zhou, C. J. Muller, T. P. Burgin, and J. M. Tour, *Science* **278**, 252 (1997).

[50] C. Kergueris, J.-P. Bourgoin, S. Palacin, D. Esteve, C. Urbina, M. Magoga, and C. Joachim, *Phys. Rev. B* **59**, 12505 (1999).

[51] S. Datta, *Nanotechnology* **15**, S433 (2004).

[52] C. Cohen-Tannoudji, B. Diu, and F. Laloe, *Quantum mechanics, Volume 1*, Wiley, 1977.

[53] G. H. Golub and C. F. Van Loan, *Matrix Computations.*

[54] E. Boulat, H. Saleur, and P. Schmitteckert, *Phys. Rev. Lett.* **101**, 140601 (2008).

[55] A. Branschädel, G. Schneider, and P. Schmitteckert, *ArXiv e-prints* (2010).

[56] N. W. Ashcroft and D. N. Mermin, *Festkörperphysik*, Oldenbourg Verlag, 2012.

[57] A. Branschädel, G. Schneider, and P. Schmitteckert, *Annalen der Physik* **522**, 657 (2010).

[58] A. Branschädel, E. Boulat, H. Saleur, and P. Schmitteckert, *Phys. Rev. B* **82**, 205414 (2010).

[59] I. Bâldea and H. Köppel, *Phys. Rev. B* **81**, 193401 (2010).

[60] G. D. Mahan, *Many-Particle Physics.*

[61] A. M. Läuchli, J. Sudan, and E. S. Sørensen, *Phys. Rev. B* **83**, 212401 (2011).

[62] E. Anderson, Z. Bai, C. Bischof, S. Blackford, J. Demmel, J. Dongarra, J. Du Croz, A. Greenbaum, S. Hammerling, A. McKenney, et al., *LAPACK Users' guide*, volume 9, Siam, 1999.

[63] U. Schollwöck, *Rev. Mod. Phys.* **77**, 259 (2005).

[64] K. A. Hallberg, *Advances in Physics* **55**, 477 (2006).

[65] R. M. NOACK and S. R. MANMANA, Diagonalization- and Numerical Renormalization-Group-Based Methods for Interacting Quantum Systems, in *Lectures on the Physics of Highly Correlated Electron Systems IX*, edited by A. AVELLA and F. MANCINI, volume 789 of *American Institute of Physics Conference Series*, pp. 93–163, 2005.

[66] A. J. DALEY, C. KOLLATH, U. SCHOLLWÖCK, and G. VIDAL, *Journal of Statistical Mechanics: Theory and Experiment* **2004**, P04005 (2004).

[67] S. R. WHITE and A. E. FEIGUIN, *Phys. Rev. Lett.* **93**, 076401 (2004).

[68] A. E. FEIGUIN and S. R. WHITE, *Phys. Rev. B* **72**, 020404 (2005).

[69] H. G. LUO, T. XIANG, and X. Q. WANG, *Phys. Rev. Lett.* **91**, 049701 (2003).

[70] J. J. SAKURAI and S. F. TUAN, *Modern quantum mechanics*, volume 1, Addison-Wesley Reading, Massachusetts, 1985.

[71] M. SUZUKI, *Progress of Theoretical Physics* **56**, 1454 (1976).

[72] M. SUZUKI, *Communications in Mathematical Physics* **51**, 183 (1976).

[73] H. F. TROTTER, *Proc. Amer. Math. Soc.* **10**, 545 (1959).

[74] C. RUNGE, *Math. Ann.* .

[75] W. KUTTA, *Z. Math. Phys.* **46**, 435 (1901).

[76] K. HEUN, *Z. Math. Phys.* **45**, 23 (1900).

[77] Y. SAAD, *SIAM Journal on Numerical Analysis* **29**, pp. 209 (1992).

[78] O. LEGEZA, J. RÖDER, and B. A. HESS, *Phys. Rev. B* **67**, 125114 (2003).

[79] D. ROY, *Phys. Rev. B* **81**, 085330 (2010).

[80] V. MUJICA, M. A. RATNER, and A. NITZAN, *Chem. Phys.* **281** (2002).

[81] P. E. KORNILOVITCH, A. M. BRATKOVSKY, and R. STANLEY WILLIAMS, *Phys. Rev. B* **66**, 165436 (2002).

[82] K. STOKBRO, J. TAYLOR, and M. BRANDBYGE, *Journal of the American Chemical Society* **125**, 3674 (2003), PMID: 12656578.

[83] S. DATTA, W. TIAN, S. HONG, R. REIFENBERGER, J. I. HENDERSON, and C. P. KUBIAK, *Phys. Rev. Lett.* **79**, 2530 (1997).

[84] I. I. OLEYNIK, M. A. KOZHUSHNER, V. S. POSVYANSKII, and L. YU, *Phys. Rev. Lett.* **96**, 096803 (2006).

[85] R. METZGER, B. CHEN, U. HOEPFNER, M. LAKSHMIKANTHAM, D. VUILLAUME, T. KAWAI, X. WU, H. TACHIBANA, T. HUGHES, H. SAKURAI, J. BALDWIN, C. HOSCH, M. CAVA, L. BREHMER, and G. ASHWELL, *J. Am. Chem. Soc.* **119**.

[86] E. LÖRTSCHER, B. GOTSMANN, Y. LEE, L. YU, C. RETTNER, and H. RIEL, *ACS Nano* **6**, 4931 (2012).

[87] P. HOROWITZ, W. HILL, and T. C. HAYES, *The art of electronics*, volume 2, Cambridge university press Cambridge, 1989.

[88] W. MAGNUS, *Communications on Pure and Applied Mathematics* **7**, 649–673 (1954).

[89] S. BLANES, F. CASAS, J. OTEO, and J. ROS, *Physics Reports* **470**, 151 (2009).

[90] A. ALVERMANN and H. FEHSKE, *Journal of Computational Physics* **230**, 5930 (2011).

[91] A. ISERLES, S. NØRSETT, and A. RASMUSSEN, *Applied Numerical Mathematics* **39**, 379 (2001), Themes in Geometric Integration.

[92] H. MUNTHE-KAAS and B. OWREN, *Philosophical Transactions: Mathematical, Physical and Engineering Sciences* **357**, pp. 957 (1999).

[93] M. VEKIĆ and S. R. WHITE, *Phys. Rev. Lett.* **71**, 4283 (1993).

[94] M. MOLINER and P. SCHMITTECKERT, *EPL* **96**, 10010 (2011).

[95] F. GEBHARD, K. ZU MÜNSTER, J. REN, N. SEDLMAYR, J. SIRKER, and B. ZIEBARTH, *Annalen der Physik* **524**, 286 (2012).

[96] P. SCHMITTECKERT, S. T. CARR, and H. SALEUR, *Phys. Rev. B* **89**, 081401 (2014).

[97] B. ENGQUIST and A. MAJDA, *Math. Comp.* **31**, 629 (1977).

[98] F. ARNOLD, F. WEIGEND, and F. EVERS, *J. Chem. Phys.* **126**, 174101 (2007).

[99] A. ARNOLD and F. EVERS, "Molecular conductance from ab-initio calculations: self-energies and absorbing boundary conditions", in *CFN Lectures on Functional Nanostructures - Volume 2: Nanoelectronics*, Springer Verlag Berlin Heidelberg, 2011, 2011.

[100] P. SCHMITTECKERT, *Annalen der Physik* **524**, 89 (2012).

[101] M. ZWOLAK and G. VIDAL, *Phys. Rev. Lett.* **93**, 207205 (2004).

[102] W. BRENIG, *Nonequilibrium PhenomenonSpringer, Berlin* (1989).

[103] H. BRUUS and K. FLENSBURG, *Many-body quantum theory in condensed matter physics*, volume 198566336, Oxford University Press Oxford, 2004.

[104] G. G. SLEIJPEN and H. VAN DER VORST, *SIAM Journal on Matrix Analysis and Applications* **17**, 401 (1996).

[105] C. LANCZOS, *Journal of Research of the National Bureau of Standards* **45** (1950).

[106] W. E. ARNOLDI, *Quarterly of Applied Mathematics* **9**, 17 (1951).

[107] Y. SAAD, *Linear Algebra and its Applications* **34**, 269 (1980).

[108] E. R. DAVIDSON, *Journal of Computational Physics* **17**, 87 (1975).

[109] B. N. PARLETT, *The Symmetric Eigenvalue Problem*, Prentice-Hall, 1980.

[110] D. S. WATKINS, *Fundamentals of Matrix Computations*, Wiley-interscience, 2 edition, 2002.

[111] Z. BAI, J. DEMMEL, J. DONGARRA, A. RUHE, and H. VAN DER VORST, *Templates for the solution of Algebraic Eigenvalue Problems: A Practical Guide*, SIAM, 2000.

[112] S. R. WHITE, *Phys. Rev. Lett.* **77**, 3633 (1996).

[113] J. OLSEN, P. JØRGENSEN, and J. SIMONS, *Chemical Physics Letters* **169**, 463 (1990).

[114] C. MOLER and C. V. LOAN, *SIAM Review* **45**, pp. 3 (2003).

[115] P. ALBRECHT, *SIAM Journal on Numerical Analysis* **33**, pp. 1712 (1996).

[116] E. GALLOPOULOS and Y. SAAD, *SIAM Journal on Scientific and Statistical Computing* **13**, 1236 (1992).

Acknowledgements

In this chapter i want to thank all the people who helped me during the course of my time at the institute.

I am really grateful to Peter Schmitteckert that he supervised me and and advised me on the topics of my PhD thesis. I also want to thank Maik Höschele, Nikolaos Kainaris, Pablo Schad, Christian Seiler, Nicolas Voigt, Philip Wollfarth and Max Zoller for proof reading parts of my thesis. Jörg Schmalian and Ferdinand Evers have accepted the referee jobs for my thesis and have gone to the time and effort of reading and rating the thesis, which i am very thankful for. I appreciate the great job the TKM and TFP admins Andreas Poenecke and Christian Seiler did at keeping the computers running and giving advice on related matters, as well as the lots of help i received from Rose and Fabienne Flatter on administrative matters. The continuous support of my family and of Anne Schödl helped me during difficult times, and i cannot express my gratitude towards them in words.